IN SITU TEM STUDY ON THE NANOMECHANICAL BEHAVIORS OF METALLIC NANOWIRES

by

Jiangwei Wang

B.S., Xi'an University of Technology, 2006

M.S., Institute of Metal Research, Chinese Academy of Sciences, 2009

Submitted to the Graduate Faculty of

Swanson School of Engineering in partial fulfillment

of the requirements for the degree of

Doctor of Philosophy

University of Pittsburgh

2014

UNIVERSITY OF PITTSBURGH

SWANSON SCHOOL OF ENGINEERING

This dissertation was presented

by

Jiangwei Wang

It was defended on

September 23, 2014

and approved by

Brian Gleeson, PhD, Professor, Department of Mechanical Engineering and Materials Science

Jörg M.K. Wiezorek, PhD, Professor, Department of Mechanical Engineering and Materials Science

William S. Slaughter, PhD, Associate Professor, Department of Mechanical Engineering and Materials Science

Guofeng Wang, PhD, Assistant Professor, Department of Mechanical Engineering and Materials Science

Guangyong Li, PhD, Associate Professor, Department of Electrical and Computer Engineering

Dissertation Director: Scott X. Mao, PhD, Professor, Department of Mechanical Engineering and Materials Science

IN SITU TEM STUDY ON THE NANOMECHANICAL BEHAVIORS OF METALLIC NANOWIRES

Jiangwei Wang, PhD

University of Pittsburgh, 2014

In this dissertation, the relationships between structure-mechanical properties-deformation mechanisms in face-centered cubic (FCC) and body-centered cubic (BCC) metallic nanowires have been studied using in situ TEM nanomechanical testing.

It is well known that smaller is stronger and the widely-observed size effect is believed to arise from dislocation interactions inside nanocrystals. However, the interaction mechanisms in small-volume nanocrystals remain unexplored. Here, it was found that surface-nucleated dislocations can strongly interact inside the confined volume of Au nanowires, which led to a new type of dislocation-originated stacking fault tetrahedra (SFT), at variance to the widely-believed vacancy-originated SFT. The atomic-scale processes of nucleation, migration and annihilation of dislocation-originated SFT were revealed, shedding new light onto the strain hardening and size effect in small-volume materials.

Although nanoscale twinning is an effective mean to enhance the strength of metals, twin-size effect on the deformation and failure of nanotwinned metals remains largely unexplored, especially at the minimum twin size. Here, a new type of size effect in nanotwinned Au nanowires is presented. As twin size reaches the angstrom-scale, Au nanowires exhibit a remarkable ductile-to-brittle transition that is governed by the heterogeneous-to-homogeneous dislocation nucleation transition. Quantitative measurements show that approaching such a

nanotwin size limit gives rise to the ultra-high strength in Au nanowires, close to the ideal strength limit of perfect Au.

Twinning is a fundamental deformation mode that competes against dislocation slip in crystals. At the nanoscale, higher stresses are required for plastic deformation than that in bulk, which favors twinning over dislocation slip. Indeed, deformation twinning has been well-documented in FCC nanocrystals. However, it remains unexplored in BCC nanostructures. Here, it shows that twinning is the dominant deformation mode in BCC-tungsten nanocrystals. A competition between twinning and dislocation slip occurs when changing the loading orientations, attributed to the defect growth controlled plasticity in BCC nanocrystals. Several important commonalities and differences in FCC and BCC nanocrystals deforming at nanoscale are further proposed.

The results from this dissertation advance fundamental understanding of plastic deformation in a broad class of metals and alloys, and are of technological importance for degradation control and future design of ultra-strength nanomaterials.

TABLE OF CONTENTS

LIST OF TABLES

LIST OF FIGURES

PREFACE

This is a good opportunity to express my acknowledgement to all of those who have helped, supported and accompanied me during my PhD study. First and foremost, I would like to thank my advisor, Dr. Scott X. Mao, from the depths of my heart, for his support, encouragement, discussion and inspiration. His professional knowledge and support lead me into the exciting research filed of nanomechanics.

My special thanks and appreciates go to my collaborators. Thank Dr. Ting Zhu in Georgia Institute of Technology, for his great efforts in atomic-scale simulations, helpful discussion and inspiration; Dr. Frederic Sansoz in The University of Vermont, for his excellent work in simulating the nanotwinned metals; Dr. Wei Cai in Stanford University and Dr. Christopher R. Weinberger, who is now an associate professor in Drexel university, for their work and helpful discussion on the dislocation nucleation in BCC metals; Dr. Jianyu Huang for his helpful discussion, support and inspiration; Dr. Shouheng Sun in Brown university for providing the great samples. I also want to express my sincere appreciation and gratitude to my committee members, Dr. Brian Gleeson, Dr. William S. Slaughter, Dr. Jörg M.K. Wiezorek, Dr. Guofeng Wang and Dr Guangyong Li for their precious time and always been there for me.

My next acknowledgement goes to Dr. John Sullivan, Dr. Yang Liu (Now in North Carolina State University), Dr. Xiaohua Liu (Now in Enevate Corporation), Dr. Katherine L. Jungjohann, Mr. Anthony J. Coley in Sandia National Laboratory and Dr. Chongmin Wang in

Pacific Northwest National Laboratory, for their generous help and technical assistance during my researches.

I am also grateful to my group members, He Zheng, Li Zhong, Liqiang Zhang and Yang He for their friendship and support in research. Thanks are also due to my friends in U.S. and China, especially Yu Gong, Yinkai Lei, Bing Ma, Pu Zhang and Qingcheng Yang at PITT, Feifei Fan and Zhi Zeng in Georgia Institute of Technology, Wentao Liang in Pennsylvania State University, Yujie Zhu in University of Maryland, for their generous help in both my life and research.

Finally, the most heartfelt and sincere acknowledgement must be expressed to my family, especially my dear wife. Their unconditional love, patience, understanding and support make my life more meaningful and my study a pleasant journey. This thesis is dedicated to all of them.

1.0 INTRODUCTION

Nanosized materials hold great promising in the application of memristor, sensor, detector, electronics, batteries and micron/nano electro-mechanical systems (MEMS/NEMS)[1-7], due to their excellent phys-chemical properties, such as electrical[4,8,9], mechanical[10-12], optical[13,14], chemical[15] and electrochemical[16-18] properties. Those superior properties originate from their high surface-to-volume ratio and large surface energy compared to their bulk counterparts[19-21]. During past 20 years, numerous efforts have been made on the synthesis, characterization and application of nanosized materials. The materials include metals[9,22], semiconductors[23,24], alloys[25,26], ceramics[27,28] and nanocomposites[29-32], in the forms of nanoparticles, nanowires, nanorods and quantum dots. The broad applications of those nanostructures have also been theoretically explored in various research fields. However, in real applications, the mechanical, electrical, thermal, chemical or electrochemical induced degradations can lead to the loss of their stability and functional properties, as well as the serving life[31,33-36], which hinder their wide applications. As the materials' size scales down, such degradations might be further promoted due to high atoms diffusivity induced by the large surface energy. Therefore, the fundamental understanding on the dynamic processes of degradations are crucial important for future design and development of nanosized materials with high reliability. However, those degradations are largely unexplored at present due to the technological difficulties in handling individual nanosized specimen, especially at the atomic-scale.

On the other hand, it is well-known that the phys-chemical properties of materials can be well controlled by the elastic strain field applied on the materials, especially at nanoscale[19]. Revealing the relationships between microstructure, mechanical properties and deformation mechanisms in nanosized materials are thus central important for the "elastic strain engineering"[19]. Thanks to the development of nano-fabrication/nano-manipulation technologies[12,37,38] and large-scale molecular dynamics (MD) simulations[39-41], significant processes have been made in understanding the structure-mechanical properties-deformation mechanisms relationships at small length scale by both experimental and theoretical studies[12,37-41]. At the micron and sub-micron scales, materials show ultrahigh strength, near-ideal elastic strain limit and improved young's modulus[19,37,42], while their deformation mechanisms are quite distinct from their bulk counterparts, in both defect nucleation and propagation[20,40,42-45]. As the material size further scales down to nano or atomic scale, the free surface plays significant role in controlling the yielding, plastic deformation and failure of materials[20,21,43,46,47], as revealed by the large-scale MD simulations. Several different kinds of deformation modes have been observed in nanosized materials under MD simulation[20,21], such as dislocation nucleation[43,48], deformation twinning[49,50], phase transformation[46], shape memory effect[51,52] and atomic-scale chain[47]. However, due to its inherent ultrahigh strain rate, truncated atomic potential and idealized crystal geometry used in MD simulations, those results should be only considered as inspirations of our understanding which need to be further validated or disproved by the experimental evidences. However, due to the technical difficulties in handling, loading and measuring at nanoscale, it has been a long-standing challenge to reveal those deformation processes, especially at the atomic-scale.

Recently, a novel transmission electron microscope (TEM) specimen holder coupled with a scanning tunnel microscope (STM) probe has been successfully developed, which allows the atomic-scale observation on the structure evolution of nanosized materials[17,30,53-55]. Individual specimen with different geometries can be easily picked up, manipulated and loaded by the ultrathin STM probe, while the atomic-scale resolution is kept. More importantly, an atomic force microscope (AFM) or nanoindentation chip can be applied in an alternated experimental setup allowing the stress-strain measurement during mechanical loading[56,57]; as a result, the microstructure, mechanical properties and deformation mechanisms of nanosized materials can be studied systematically and correlated together. However, very few studies have been conducted toward revealing those fundamental questions at present. In this research, we will use the unprecedented in-situ atomistically-resolved approach for discovering the previously unknown deformation mechanisms in metallic nanostructures and exploring their structure-mechanical properties-deformation mechanisms relationship to shed some light for the materials design and mechanical degradation controlling at atomic-scale.

The thesis is organized as follows. In Chapter 2, the deformation mechanisms at different length scale will be reviewed. Based on the research background, the objectives of the present study will be proposed.

In Chapter 3, the experimental methods, including materials preparation, experimental setup and nanomechanical testing, will be discussed in detail. A novel method to fabricate nanowires from bulk materials inside the TEM will be presented in this chapter.

In Chapter 4, atomic-scale dynamic observations will be used to reveal the dislocation interactions inside the small volume of nanocrystals with twin-free or low density twins. Dislocation-originated stacking fault tetrahedral (SFT) were observed to form following an

intersection and cross-slip process, which is applicable to a broad class of FCC metals and alloys. It is discovered that the deformation-induced SFT is an important deformation mode in controlling the plasticity and strain hardening at nanoscale. Those deformation-induced SFT can migrate and annihilate under mechanical loading in the manner that is not expected in bulk samples.

In Chapter 5, the effects of microstructure on the structure-properties relationship in FCC metals will be studied and discussed. By using in situ nanomechanical testing combined with atomic-scale observations, it is found that Au nanowires exhibit a remarkable ductile-to-brittle transition that is governed by the heterogeneous-to-homogeneous dislocation nucleation transition when the twin thickness is reduced to the smallest possible size of angstrom-scale (0.7 nm), profoundly contrasting with the deformation behavior of metallic nanowires with twin-free or low density twins. Quantitative measurements show that approaching such nanotwin size limit gives rise to an ultra-high tensile strength (up to 3.12 GPa) in Au nanowires. Such twin-size dependent dislocation nucleation and deformation represents a new type of size effect distinct from the sample size effect described previously.

In Chapter 6, the effects of crystal structure on the deformation mechanisms will be studied and discussed by using FCC-Au and BCC-W as examples. It discovers that W nanocrystals exhibit surprising reversible plastic deformation via twinning or irreversible plastic deformation via dislocation nucleation at room temperature and low strain rates, depending on the load orientation. Those nanosized FCC and BCC metals exhibit different behaviors in both deformation twinning and dislocation nucleation. The fundamental mechanisms will be revealed in this chapter.

In Chapter 7, the crystal structure effects on deformation at nanoscale are further explored based on the results presented in this dissertation.

Finally, the dissertation is concluded in Chapter 8 and future research directions are discussed in Chapter 9.

2.0 BACKGROUND

In this chapter, the deformation mechanisms of materials deformed at different length scales will be briefly summarized and reviewed. Main attentions will be paid onto the current understanding of deformation mechanisms of nanosized materials and their impact factors. Based on the background review, the objectives of present research will be proposed.

2.1 DISLOCATION DYNAMICS IN METALS AT DIFFERNET LENGTH SCALES

2.1.1 Deformation of bulk materials

"Crystals are like people: it is the defects in them that make them interesting", as said by Charles Frank (a famous physicist in the field of material sciences)[58]. Indeed, the theories on plastic deformation and mechanical properties of materials are all about how the defects generate, propagate and annihilate. Among those defects, dislocation (a type of line defect) are the most important one in controlling the yielding, deforming and failure of crystalline materials[59,60]. How the dislocations are generated and how they propagate and interact have been studied for more than half of century[59]. Now, it is generally believed that the frank-read source and double-cross-slip source serve as the main dislocation multiplication sources in controlling the plastic deformation in single crystals[59]. While in polycrystalline materials, the preexisting imperfections,

such as boundaries, interfaces and participates, contribute to most of the dislocations nucleation sites and sink points[59-61]. Although bulk metals can be strengthened through different mechanisms, such as work hardening, solid solution strengthening, precipitation strengthening, dispersion strengthening, the heterogeneous nucleation of dislocation from Frank-Read sources or pre-existing imperfections leads to the earlier yielding of materials and thus much lower strength compared to the perfect crystal[10,60]. Therefore, attaining theoretical strengths in metals and alloys remains an outstanding challenge.

In the 1980s, people discovered that nanocrystalline materials exhibit improved strength/hardness and better toughness, enhanced diffusivity, but lower ductility in comparison with the conventional polycrystalline materials [62,63]. Over the past couple of decades, widespread researches have been conducted to reveal the structure-mechanical properties relationship in nanocrystalline materials. It is now known that the tranditional dislocation sources do not exist in the individual grains of nanocrystalline materials owing to their limited grain size, as well as dislocation pile-ups[63,64]. Below a critical grain size, the plasticity of materials are dominated by the grain boundary (GB) processes due to the ultrahigh atom fraction at GB, such as GB rotation/sliding and/or grain growth, as confirmed by both MD simulations and experimental studies[61,63-67]. However, the GB-mediated processes bring the orientation of neighboring grains closer together and lead to the increase in grain size (Figure 2.1a), which provides a path for further deformation via shear localization or dislocation motion (Figure 2.1c)[63,64]. Consequently, softening and shear instability will occur in nanocrystalline materials, characterized by the low ductility of nanocrystalline materials[63]. Thus, the questions naturally arisen are: How the nanosized single crystal without GB deforms? What about their mechanical properties? This will be discussed in **2.1.2**.

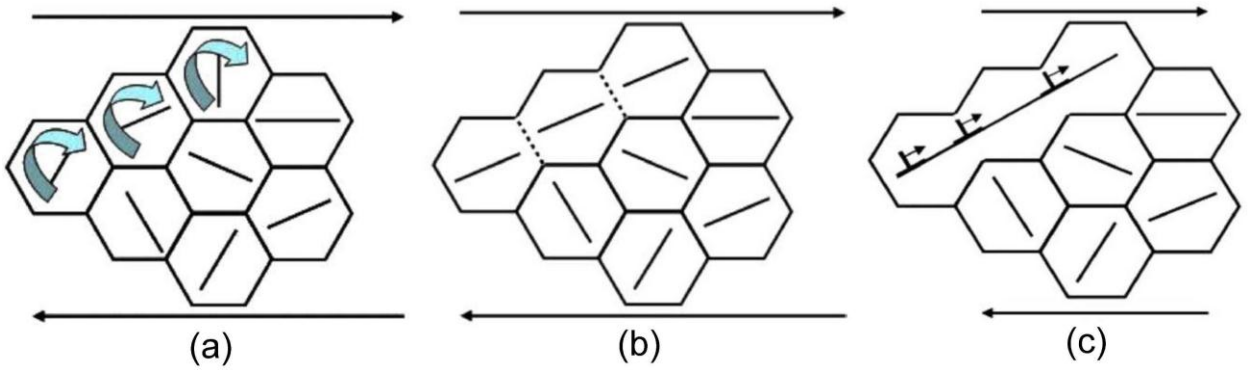

Figure 2.1 GB rotation induced grain coalescence during plastic deformation[63].

2.1.2 Deformation of single crystals at micrometer or sub-micrometer scale

Both the experimental studies and MD simulations show that "smaller is stronger" holds true in either nanocrystalline materials or single crystals[19,37,42], i.e. higher stresses are needed to yield and deform the crystals with smaller feature sizes (Figure 2.2). Nix and co-workers first revealed that the size-dependent strength is induced by the constraints of crystal geometry on the nucleation and propagation of dislocations[37,42,68]. Unlike their bulk counterparts, the mobile dislocations in sub-micrometer crystals can only propagate limited distances before annihilating at the free surface or interacting with other dislocations, leading to the dislocation starvation in the small crystals[42,68]. As a result, the overall dislocation density is reduced rapidly and ultrahigh stresses are required to the nucleation and propagation of new dislocations for accommodating the further deformation[42,68]. The dislocation starvation was confirmed by a recently study conducted by Shan et al.[44] By using in situ nanocompression conducted under TEM, they discovered that sub-micrometer nickel crystal with high density preexisting defects are mechanically annealed into a dislocation-free state (Figure 2.3), i.e. dislocation starvation, and

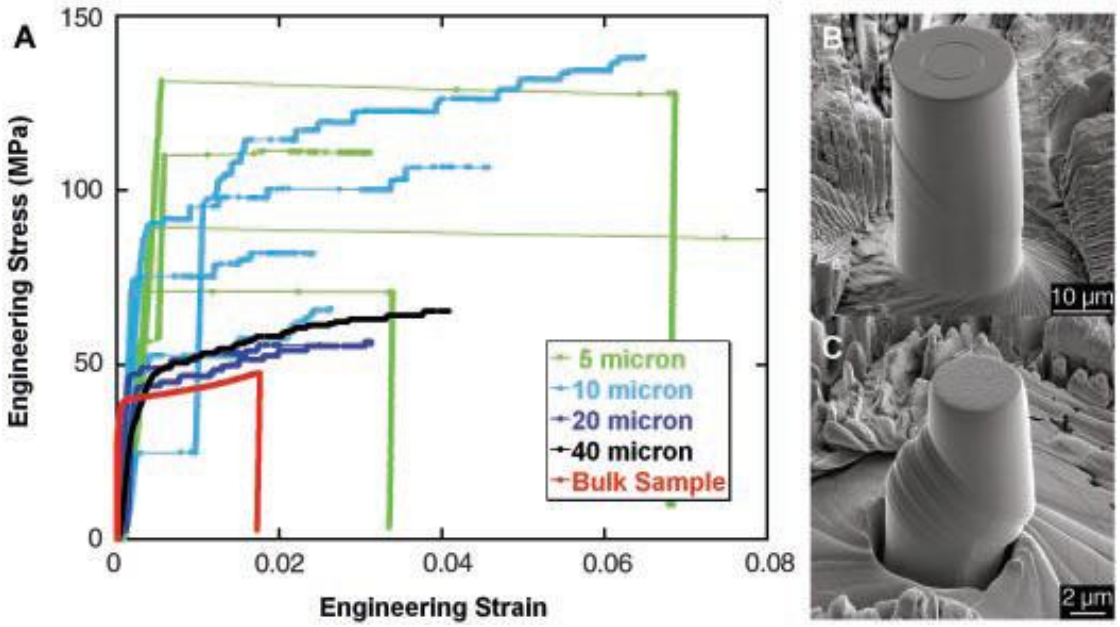

Figure 2.2 Crystal dimensions dependent mechanical properties in pure nickel samples with micron-size[37]. (a) As the sample size decreasing, the compressive strength of micron-sized nickel pillars increase significantly. (B-C) Deformation morphologies of different nickel pillars under compression.

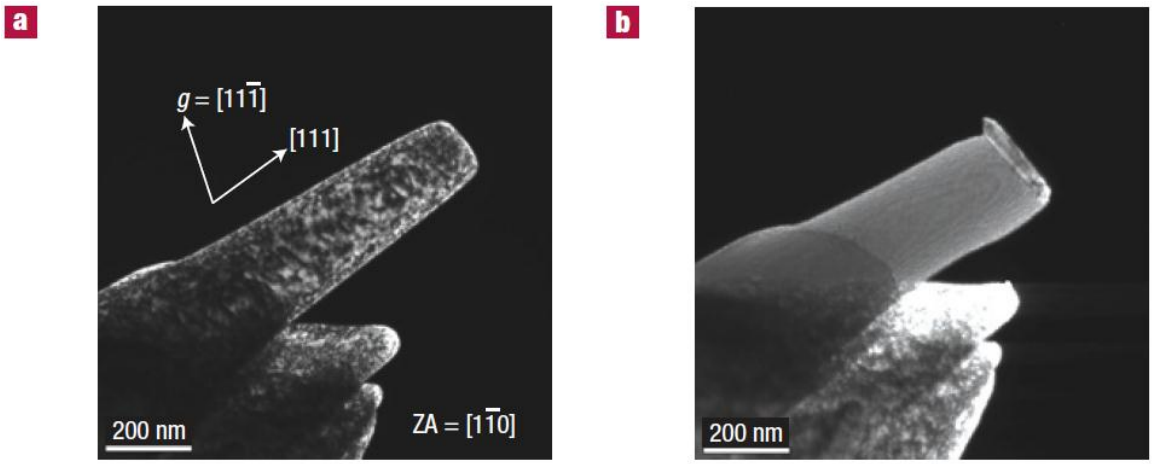

Figure 2.3 Mechanical annealing in nickel nanopillar with the diameter of 160 nm under nanocompression[44]. (a) High density defects exist in the pristine nickel nanopillar. (b) Under compression loading, the defects escape and annihilate at the free surface, leading to the mechanical annealing.

further plastic deformation are limited by the dislocation nucleation sources[44]. In the following, the dislocation sources at small length scale will be reviewed.

At micrometer or sub-micrometer scale, the plastic deformation of single crystals is controlled by the dislocation sources[42,44,45]. However, the traditional dislocation sources do not exist owing to the limited crystal size and single-crystal nature. Thus, new dislocation sources need to be triggered to mediate the plastic deformation. Recently, in situ TEM studies show that single-ended dislocation sources can operate in sub-micrometer face-centered cubic (FCC) and body-centered cubic (BCC) single crystals[45,69,70]. The dislocations are emitted from such single-armed dislocation sources and then propagate through the rest perfect crystal, which finally escape the crystal before they can multiply or interact with others (Figure 2.4)[45]. Consequently, the mobile dislocations are exhausted rapidly and further deformations are controlled by the dislocation sources[45,69]. It should be noted that the dislocation dynamics in sub-micrometer BCC crystals are different from FCC ones due to their distinct dislocation structure. Although single-ended dislocation sources operate the deformation of BCC at sub-micron scale[70], the dislocation propagates in a manner of self-multiplication before moving out the crystal under the combined effects of surface image force and its non-planar core structure (Figure 2.5)[40]. Such kind of distinct dislocation behavior leads to a less size dependence of strength in BCC nanopillars[71-73]. Moreover, the free surfaces can serve as another major dislocation sources and sink points at smaller length scale, which significantly affect the dislocation dynamics and plastic deformation of small-volume crystals, especially at nanoscale.

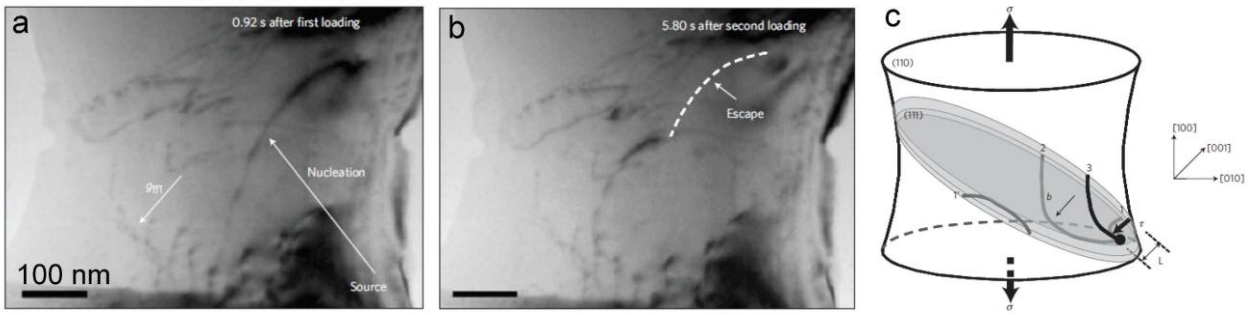

Figure 2.4 Single-ended dislocation source in sub-micrometer Al single crystals under mechanical loading[45]. (a) Dislocation nucleation. (b) Dislocation annihilation

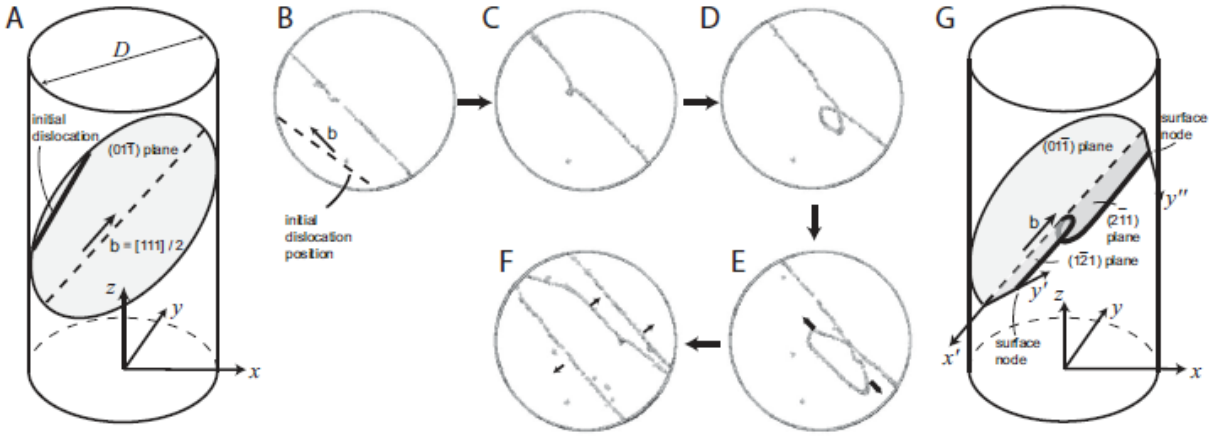

Figure 2.5 Self-multiplication during the propagation of dislocation in BCC Mo pillar[40].

2.1.3 Surface controlled deformation at nanoscale

The properties of nanomaterials are usually determined by their surface structure. When the crystal size is scaled down to tens of nanometer, significantly miscoordinated atoms locate on the surface, in contrast to their bulk counterparts[43,74]. As a result, large surface energy and surface stress are generated due to those dangling atoms and broken atomic symmetry at the free surface[20,21]. The originate of surface stress has been well reviewed in Ref.20-21[20,21] and will not be further discussed here. On the other hand, the surface atoms in nanosized materials tend to arrange along the most close-packed atomic planes to low their surface energy, and thus the surface energy are typically anisotropic, leading to the surface facets[20]. Those surface properties of nanomaterials are the physical origin of their unique properties[20,21,75-77], such as structural stability, mechanical properties and thermal conductivity.

For the mechanical properties, both MD simulation[20,43,78] and experimental study[53] have showed that the free surface plays important role in controlling the defect nucleation, propagation and annihilation. Zheng *at al.* revealed that the surface steps serve as the effective dislocation sources to accommodate the plastic deformation at nanoscale (Figure 2.6)[53]. Under mechanical loading, elastic strain gradually accumulates at the surface steps, leading to the local stress concentration. After the partial dislocation nucleates from the surface steps, the elastic strain is released[53]. However, the dislocation quickly escapes and annihilates on the opposite surface due to the small volume of nanocrystal (Figure 2.6a-c). As a result, the plastic deformation is controlled by the discrete nucleation of partial dislocation from surface steps[53]. Here, it needs to point out that the free surface also can serves as the dislocation sources in the bulk and micron-sized material, however, it is the dominated dislocation sources at nanoscale in controlling the plasticity. To reveal to what degree the surface nucleation controls the size-

dependent strength of small-volume material, Zhu *et al*. developed a atomistic model and discovered that the activation volume of surface nucleation of dislocation is relatively small (about 1-10b^3, where b represents the Burgers vector)[43]. Such small activation volume of surface nucleation induces a strong temperature and strain rate dependence of nucleation stress, which can be expressed as:

$$\sigma = \frac{Q^*}{\hat{\Omega}} - \frac{k_B T}{\hat{\Omega}} \ln \frac{k_B T N v_0}{E \dot{\varepsilon} \hat{\Omega}} \tag{2.1}$$

Where Q^* is the nucleation barrier under applied stress, $\hat{\Omega}$ represents the activation volume under applied stress, T is the temperature, k_BT corresponds to the thermal energy, E is the Young's modulus of material, $\dot{\varepsilon}$ is the deformation strain rate, N corresponds to the number of surface nucleation sites, v_0 represents the attempt frequency[43]. Above equation suggests that an upper bound exists for the nucleation stress in controlling the size dependent strength in nanopillar (Figure 2.7)[43]. More specifically, the surface nucleation only leads to a weak size effect on the strength of nanocrystals. Hence, the widely-observed size effect should arise from dislocation interactions inside nanocrystals. However, the dislocation interaction mechanism insider the small volume of nanocrytsal remains unclear at present.

On the other hand, surface facets are frequently observed on the sidewalls of metallic and semiconductor nanowires during crystal growth or mechanical deformation[10,12,53,75,79]. It has been revealed that the acoustic phonon spectra of metallic and semiconductor nanowires are strongly affected by their surface facets[10,75]. The instabilities of phonon spectrum further dictate the ideal strength, defect nucleation and thermal conductivity of materials[10,75,80]. By using MD simulations, Sansoz[75,76] has successfully predicted the effects of surface facets on the thermal conductivity and mechanical properties of Au and Si nanowires (Figure 2.8). The periodic {111} surface facets

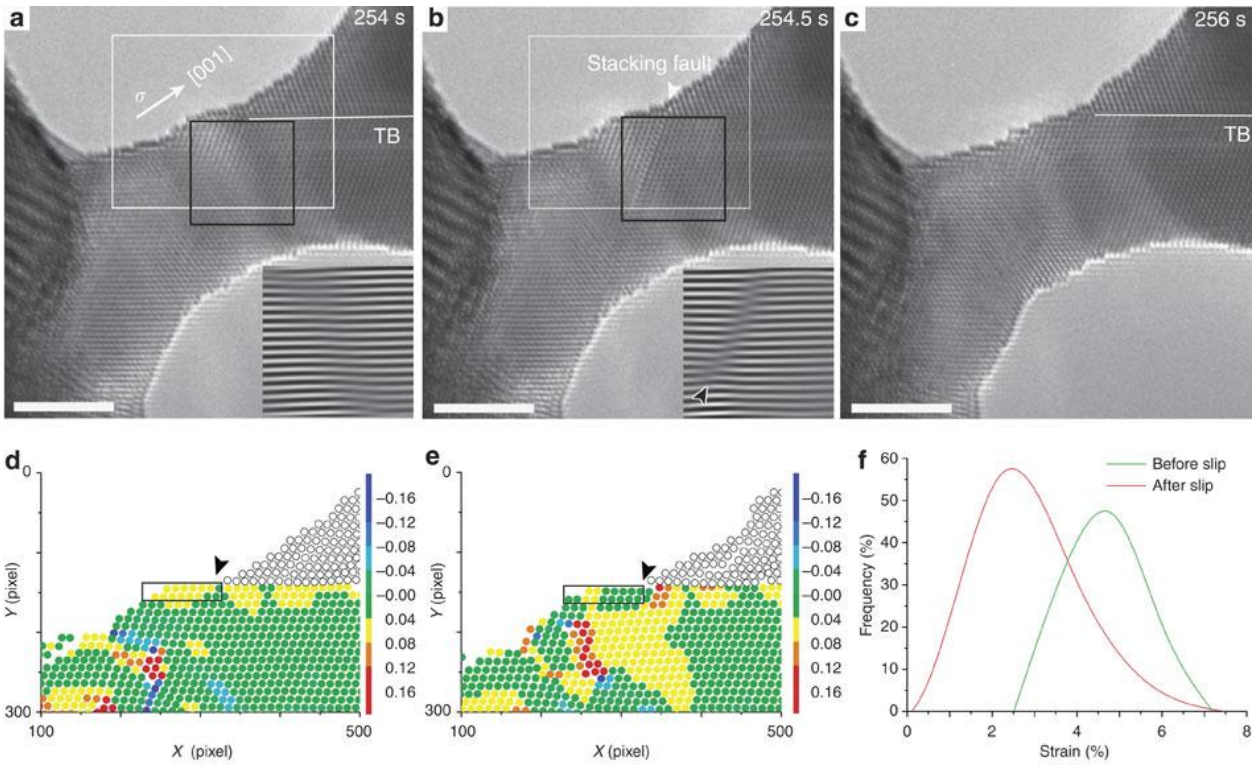

Figure 2.6 Surface controlled dislocation nucleation in sub-10 nm Au nanocrystal. (a-c) Dislocation nucleates from surface steps and annihilates at the opposite surface. (d-e) Strain field in the white-box region of Au nanocrystal before (d) and after (e) the dislocation nucleation. (f) A quantitative strain analysis in (d-e).[53]

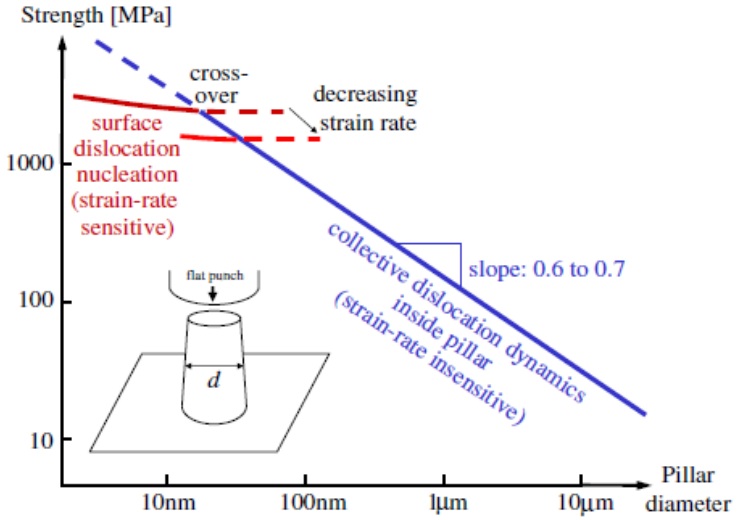

Figure 2.7 Surface effect on the rate-controlled deformation processes: size dependent strength in single-crystal nanowires or nanopillars[43].

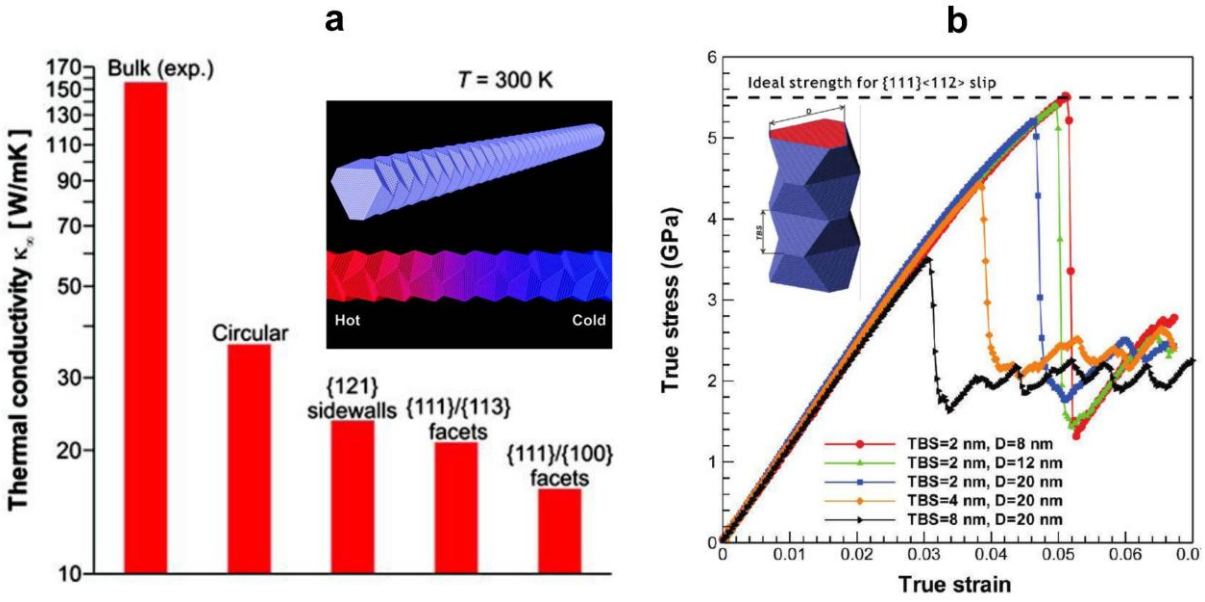

Figure 2.8 Effects of surface facets on (a) the thermal conductivity of Si nanowire[75] and (b) the mechanical properties of nanotwinned Au nanowire with surface facets[76].

significantly reduce the thermal conductivity of Si nanowires due to the phonon instabilities induced by the {111} surface facets[75]. The phonon instabilities further affects the ideal strength of materials[80]. Deng *et al.*[76]. demonstrated that the maximum strengths of polycrystalline and nanotwinned Au nanowire with smooth surface are much lower than the ideal limit of Au, however, ideal strength limit can be achieved in the zigzag Au nanowires with specific arrangement of {111} surface facets. The improved mechanical properties are attributed to the suppression effect of surface facets on the nucleation of dislocation from surface. In reality, growth twinning with surface facets are frequently observed in metallic nanowires[79,81-84]. However, the effects of surface facets on the defects nucleation and deformation dynamics remains unexplored due to the challenges in characterizing and observing the dynamic deformation process. In addition, some novel phenomenon that are unexpected in the bulk

materials may arise at nanoscale, such as superplasticity, phase transformation, shape memory and pseudoelasticity, which are induced or mediated the free surface.

In summary, considerable efforts have been devoted to study the size dependent strength and the dislocation sources at different length scale. For FCC metals, the source controlled plasticity has been well understood at different length scale. However, the physical origin of size-dependent strength is still under debate. On one hand, small volume crystal exhibits a deformation state of dislocation starvation due to the high dislocation loss rate; on the other hand, surface sources are abundant at nanoscale, which may facilitate the dislocation interaction in nanomaterials. However, it remains unclear whether stable dislocation structure or high order defects can be generated via the dislocation interactions inside the small volume of nanocrystals, which may contribute to the strain-hardening and size-dependent strength. Moreover, although some theoretical studies have been conducted to explore the dislocation dynamics in BCC metals, it remains unclear how the defects nucleate, propagate and annihilate in nanosized BCC metals. Considering the significant differences in the deformation of bulk FCC and BCC metals[20,85], the dislocation and twinning dynamics in nanosized BCC metals may exhibit a different manner.

2.2 MECHANICAL PROPERTIES AND DEFORMATION MECHANISMS OF NANOTWINNED METALS

Crystal twins can be classified into three types: growth twin (introduced during materials synthesis), deformation twins (generated by plastic deformation) and annealing twins (introduced

by the recrystallization of deformed materials during the annealing)[86]. Due to their coherent structure and high thermal and mechanical stability, crystal twins have important impacts on the material strengths, plasticity and electronic properties. However, the strengthening effect of twin boundaries is relatively low when the twin size is at micrometer scale[86]. Recently, high density twins are successfully synthesized in nanosized metals and semiconductors[84,87], providing the chance to study their effects on the material's properties. Here, main focus will be paid on to the mechanical properties and plastic deformation of nanotwinned materials.

2.2.1 Nanotwinned nanocrystalline materials

The mechanical properties, plastic deformation and fracture of ultrafine-grained metals with nanoscale growth twins have attracted extensive studies since their first discovery in 2004[87]. It is now well-known that nanotwinned nanocrystalline FCC metals have excellent ultimate strength, good ductility, high conductivity and improved fatigue tolerance as twin thickness (λ) decreases[41,88-93]. In the pioneering work, Lu *et al.* successfully synthesized ultrafine-grained copper (Cu) with nanoscale growth twins and studied its mechanical and electric properties (Figure 2.9)[87]. They discovered that the ultrafine-grained Cu with nanoscale growth twins exhibit a tensile strength up to 1 GPa (Figure 2.9b), about 10 times higher than that of bulk Cu, while retaining a high conductivity[87]. The ultrahigh strengths are attributed to the coherent twin boundaries which serve as the barriers of dislocation motion[86-88,93,94]. However, the tensile strength reaches a maximum value at the critical twin thickness of 15 nanometers, followed by a softening as the twin thickness further decreases[88]. Such kind of transition was attributed to the activity of preexisting dislocation sources at twin boundaries, such as preexisting partial dislocations and kink-like steps[41,88,92]. Recently, Li *et al.* studied the deformation of nanotwinned

nanocrystalline Cu with perfect coherent twin boundaries using MD simulation[41]. They discovered that the softening observed in nanotwinned Cu when the twin spacing is below a specific limit are induced by the nucleation and propagation of twin partials emitted from the intersection of twin boundaries with grain boundaries (Figure 2.10)[41]. Beyond the aforementioned studies, the nanoscale coherent growth twins have also been other nanograined metals, such as Ag[91], copper alloys[86] and austenite stainless steel[95], and their effects on plasticity have been widely studied by both experiments and simulations.

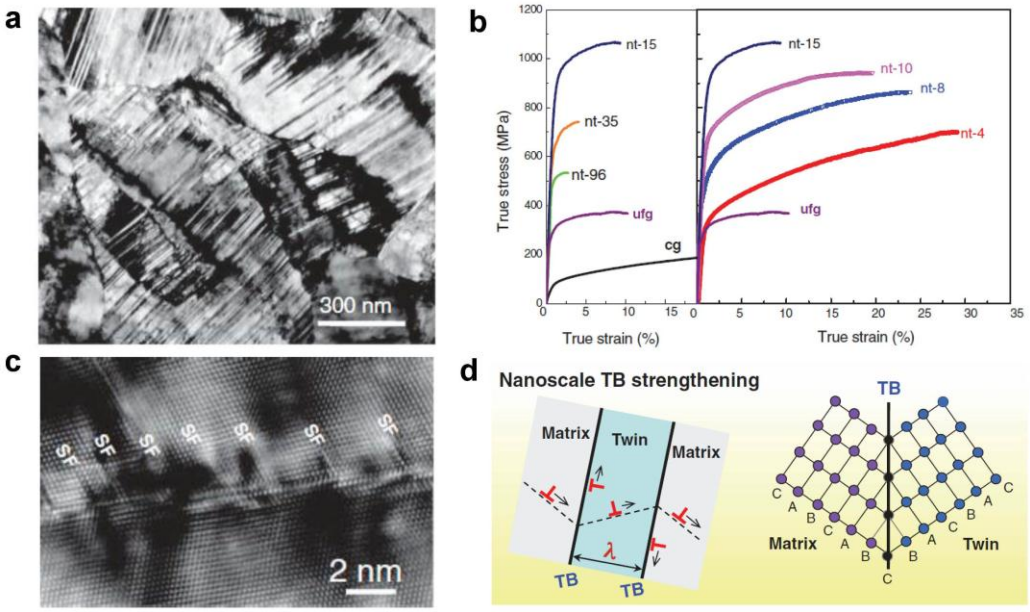

Figure 2.9 Microstructure, mechanical properties and deformation mechanism of nanotwinned nanocrystalline copper. (a) Nanocrystalline Cu with nanoscale growth twins[88]. (b) Mechanical properties of nanotwinned nanocrystalline Cu[88]. (c-d) Twin boundaries serve as the barrier of dislocation motion, contributing to the strain hardening[86,88].

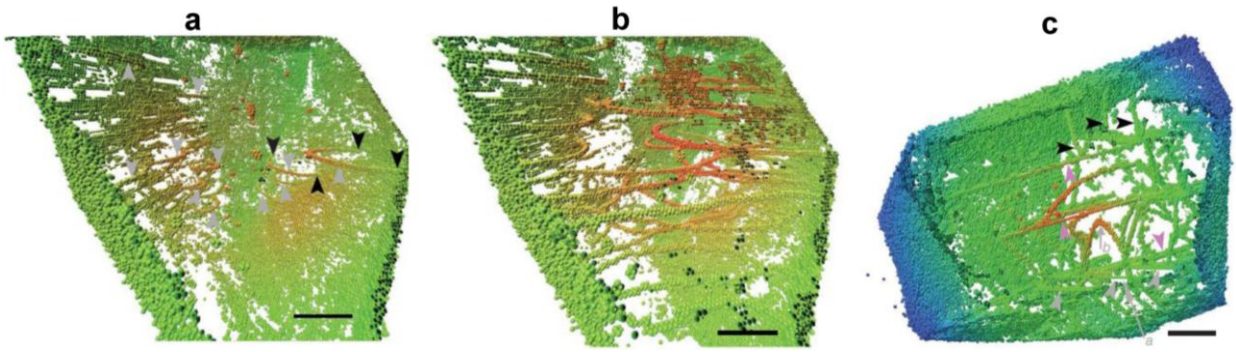

Figure 2.10 Strain softening in nanotwinned nanocrystalline Cu is governed by the dislocation nucleation from the intersection between grain boundaries and twin boundaries[41]. The black arrows point out the dislocation nucleation site. Scale bar, 10 nm.

Above discussions show that the nanotwinned samples used in previous studies are mainly nanocrystalline containing a large number of GBs, which could possibly facilitate the nucleation of partial dislocations from the pre-existing defects (e.g. GB/TB intersections) and lead to the softening. The heterogeneous nucleation of dislocations from preexisting sources also results in a yield strength that is much lower than the ideal limit of prefect crystals. On the other hand, the mechanical behavior of coherent TBs in polycrystalline materials cannot reflect the intrinsic property of samples with pure twins. In FCC single-crystalline nanowires without GBs, however, the effects of twin spacing on the plastic deformation remains largely unexplored, especially at the minimum limit of twin thickness.

2.2.2 Nanotwinned single-crystalline nanowires

Although bulk metals can be strengthened through different mechanisms, such as work hardening, solid solution strengthening, precipitation strengthening, dispersion strengthening, GB and interface strengthening[86], nanosized single-crystalline metals are more generally subjected to discrete plasticity without strain hardening after yielding due to the loss of mobile

dislocations at the free surfaces[42,53], and the maximum strength achieved in low-dimensional nanostructure is still considerably smaller than their ideal strength owing to the heterogeneous nucleation from surface and interface imperfections[53,76,96]. Therefore, attaining theoretical strengths in metallic nanostructures remains an outstanding challenge. On the other hand, nanoscale coherent twin boundary are frequently observed in the as-synthesized metallic and semiconductor nanowires, which exhibit superior electronic and photonic properties[10,12,79,81-84,97-100] . However, the effects of nanoscale growth twins on the mechanical properties of nanowires remain unclear.

Recently, Sansoz *et al.* studied the effect of coherent growth twins on the mechanical behavior of different metallic nanowires using MD simulation[76,101-105]. The theoretical studies indicate that the preexisting twin boundaries produce a large repulsive force on the moving dislocations due to the image effects across the twin boundaries, which can be expressed as $f_{CTB} = -\alpha \frac{\mu b^2}{4\pi x}$, where f_{CTB} is the force per unit length generated by coherent twin boundaries (CTB) on the dislocation, μ is the shear modulus of crystal along the slip direction, b is the Burgers vector, x is the distance between the moving dislocation and CTB, α is a dimensionless measure of the strength of CTB[104,106]. Simulation studies showed that such repulsive force expresses a linear increase relationship with $1/\lambda$. In other words, the smaller the twin spacing, the higher the yield stress of nanotwinned nanowire. Moreover, the slope of the repulsive force-$1/\lambda$ curve is found to be further affected by the nanowire diameter, which is doubled as nanowire diameter decreases from 25 nm to 8 nm[103]. As a result, the yield strength of materials can be effectively improved by reducing the twin size and crystal size simultaneously[103,104,106]. Figure 2.11 shows a typical tensile stress–strain curve and deformation snapshots of nanotwinned Au nanowire. The whole deformation is characterized by three deformation regimes: elastic, strain-

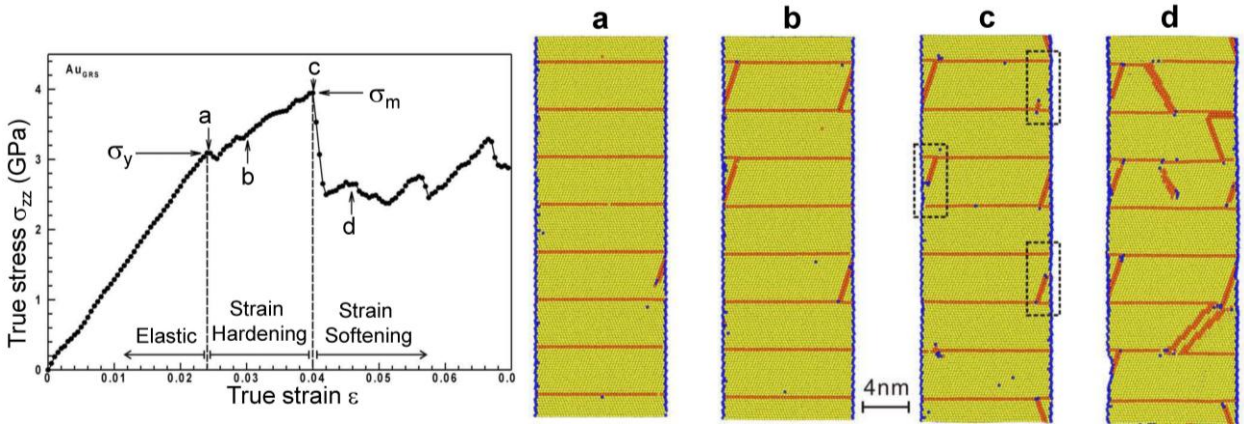

Figure 2.11 Tensile stress–strain curve and deformation snapshots of nanotwinned Au nanowire[101]. (a-d) Deformation snapshots at different stage of the stress-strain curve.

hardening and strain softening (Figure 2.11)[101]. After the initial yielding, the twin boundaries can serve as the barrier for the propagation of surface-nucleated partial dislocations, contributing to significant work hardening effects[101]. However, further deformation leads to the strain softening due to the detwinning (Figure 2.11), which is caused by the transmission of dislocation through the twin boundaries[101].

In the past few years, a lot of effects have been made to reveal the deformation mechanisms of materials at nanoscale, however, most experimental studies have been focused on the mechanical properties, deformation and failure of single-crystalline nanowires[53,96,107-109]. Although nanotwinned nanowires have been studied by simulations, the effects of twin spacing on the mechanical behavior and plasticity of ultrathin single-crystalline nanowires remained largely unexplored in experiments, especially at the theoretical limit of twin spacing, due to the difficulties in fabricating and handling samples at small length scale. Considering the unique and superior properties of nanotwinned materials and their potential application for nanodevices, revealing the effects of nanoscale twins in plasticity and fracture of nanotwinned nanowires are both fundamentally and technologically important.

2.3 DEFORMATION TWINNING IN NANOSIZED METALS

Deformation twinning is a particularly important deformation mechanism in controlling the plasticity of crystals, especially in materials with limited numbers of slip system or under extremely deformation conditions (such as low temperature or high strain rate condition)[59]. As a common and important deformation mode, the deformation twinning in bulk materials have been well documented and reviewed in literature[20,59,110-113], which thus will not be further summarized in detail. Major attentions will be paid on to the deformation twinning in nanosized materials, mainly metals. Moreover, it is known that deformation twinning in metals and alloys is strongly affected by their crystal structure, and thus it will be reviewed based on the different crystal structure, such as FCC, BCC and HCP.

2.3.1 Deformation twinning in FCC metals

It is generally believed that the deformation twins in FCC metals and alloys are generated by the successive nucleation and glide of twinning partial dislocation on the adjacent slip planes[110,112]. In the polycrystalline FCC metals and alloys, the deformation twinning is strongly affected by their stacking fault energy (SFE), grain size, strain rate and deformation temperature[110,112]; while in the single crystalline FCC materials (bulk or nanosize), it is mainly controlled by the crystal size and orientation (Schmid factor)[20]. The deformation twinning in polycrystalline FCC materials can be summarized as:

1. SFE is the major material's parameter in controlling the twinning ability in FCC metals and alloys. The lower the SFE, the higher the twinning ability under mechanical loading[110,112,114-116]. The effects of SFE on deformation twinning hold true at different length scales[20,110,112].

2. Low deformation temperature and high strain rate could promote the deformation twinning in the coarse-grained and nano-grained metals and alloys, due to the competition between nucleation stresses for dislocation and deformation twinning[110,112,113,117]. This is also hold true in metals with other structures, such as BCC and HCP[118-121].
3. Grain size affects the twinning ability of FCC materials. Deformation twinning is rarely observed during the deformation of coarse-grained FCC metals and alloys with medium to high SFEs, such as Cu, Ni and Al; however, as the grain size is further refined down to nanoscale (such as 100 nanometers) deformation twinning are frequently observed in those metals[122-127].

In the single crystalline FCC metals (bulk or nanosize), the deformation twinning is strongly controlled by the crystal orientation. For example, dislocation slip usually dominates the plastic deformation in bulk copper with coarse-grain; however, Han *et al.* discovered that deformation twinning can be effectively activated in single crystalline copper under specific crystal orientation[128]. In FCC metallic nanowires, the competition between dislocation slip and deformation twinning is influenced by crystal orientation, crystal size and nanowire side surfaces. Weinberger *et al.* summarized the competition between dislocation slip and deformation twinning in FCC metallic nanowires observed in MD simulation[20]. For a given FCC metallic nanowires, such as Au, the deformation mechanisms are usually strong orientation-dependent[20]. More specifically, whether dislocation slip or deformation twinning occurs is controlled by the Schmid factors of the leading and trailing partial dislocation. If the Schmid factor of leading partial dislocation is lower than that of trailing partial dislocation in a specific orientation, either full dislocation will nucleate directly, or the nucleation of leading partials will be followed by a trailing partial on the same slip plane with a stacking fault between them, forming a full-slip;

however, leading partial will nucleate successively and layer-by-layer on the adjacent slip plane to form a deformation twinning when the Schmid factor of leading partials are larger[20]. Whereas, the Schmid law may breaks down when a local stress concentration is induced by the side surface of nanowires, which could promote the deformation twinning[20]. This has been confirmed by both experiment and MD simulations[50,53]. Moreover, crystal size also affects the deformation twinning[129,130]. As the crystal size decreases, a transition from the dislocation mediated plasticity to deformation twinning dominated plasticity occurs, due to the high stress required for the deformation at small length scale, which will favor the twinning[130].

The deformation twinning in FCC metallic nanowires could mediate the superplasticity, shape memory effect, reorientation and pseudoelastic deformation[50,107,131], which has important applications in the energy-conversion, elastic strain engineering and MEMS. However, in a recent studied, ultrathin Au nanowires were observed to fail via brittle fracture[56]. Although it is attributed to the misalignment-induced deformation twinning, the physical origin of such brittle fracture is under debate, considering the twinning induced plasticity and ductile nature of Au. Revealing the physical origins of brittle fracture in Au nanowire is fundamentally important for nanoscale device applications.

2.3.2 Deformation twinning in BCC metals

Due to the high lattice friction of BCC metals resulting from their non-planar core of screw dislocation[20,132,133], their deformation mechanisms are significantly different from FCC metals. However, compared to their well-documented FCC counterparts[20,40,53,68,101,134], much less is known about the shifts in mechanical properties of BCC at small scales. As discussed above, deformation twinning is the main deformation mechanism for HCP and FCC metals with ultra-

low SFE at room temperature (RT)[110,114,116]. However, numerous studies have shown that the plastic deformation of BCC metals at RT is dominated by the motion of screw dislocations[40,85,118,134,135]. Deformation twinning in BCC metals is typically observed in the deformation at low temperatures and high strain rates[110,113,119,136], in which the stress for dislocation slip in BCC metals increases rapidly with decreasing temperature and increasing strain rate[113,125]. Whereas it remains unclear whether BCC metals can deform by deformation twinning at RT and at low strain rates. On the other hand, "smaller is stronger" has been well established in FCC and BCC metals[19,37,68,134], *i.e.*, the flow stress increases markedly with decreasing sample size. It is thus expected that a transition from dislocation slip to twinning may occurs if the size of a BCC metal is small enough. Moreover, the generalized SFE for deformation twinning in BCC metals is dramatically different from that of FCC metals[137-139], suggesting some fundamental differences in deformation twinning between FCC and BCC. Additionally, the plasticity and size dependent behaviors of nanosized FCC metals are dominated by the surface nucleation of dislocation, which, due to their high mobility, can easily escape the nanowire and leave it in dislocation-starved state[20,40,53,101]. In BCC nanocrystals, screw dislocations move slowly and have the potential to multiply[40,134], which reduces the tendency of the crystal to starve. As a result, the dislocation dynamics in nanosized BCC and FCC metals might be different. However, those fundamental questions remain unexplored at present.

Currently, the understanding of deformation twinning in nanosized BCC metals mainly depends on the MD simulations. In the nanocrystalline Mo and Ta, deformation twinning are frequently observed, however, it could propagate and hit the grain boundaries at the opposite side, inducing the generation of cracks[140-143]. In a recent experiment study of nanocrystalline Ta, the deformation twinning is claimed to occur under nanoindentation[144], however, it turns out that

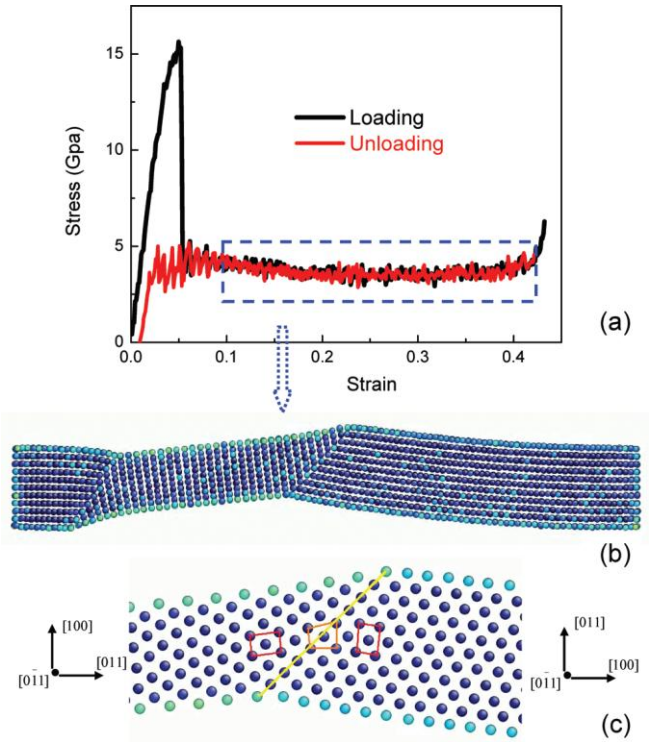

Figure 2.12 Stress-strain curves and deformation twining in a BCC W [100] nanowire[145]. (a) Stress-strain curves under loading/unloading cycle. (b) Deformation twinning mediated deformation. (c) Crystal orientation near a twin boundary.

the nanocrystalline Ta has a FCC structure. Thus, currently, the direct experimental evidence on the deformation twinning in small volume BCC metals is still missing. In MD simulations, it is reported that the deformation twinning is strongly materials-dependent in the single-crystalline BCC nanowires. MD simulations have showed that [100] BCC Mo, W and Fe nanowires exhibit reversible deformation twinning and superelasticity under different strain rates (Figure 2.12), driven by the minimization of surface energy[139,145-147], while the deformation of BCC V nanowire is dominated by the dislocation slip and thus shows limited ductility[139]. The distinct deformation mechanism of V nanowires is induced by the high energy barrier for deformation twinning than full dislocation slip[139]. For a given BCC nanowires, such as Mo, the deformation

twinning are strong crystal orientation dependent due to the different deformation induced surface facets[147].

From the above summarizations, it can be seen that the deformation of BCC metals at nanoscale mainly rely on MD simulations. However, due to the intrinsic high strain rate and truncated potential in MD simulations, the deformation mechanism of nanosized BCC metals need to be further confirmed by experimental evidences. Several critical issues need to be studied in experiments: the size dependent transition in deformation mechanisms, twinning and dislocation nucleation mechanisms in nanosized BCC metals, crystal orientation dependent deformation in nanosized BCC metals and their physical origins.

2.3.3 Deformation twinning in HCP metals

Due to the lack of sufficient slip systems to mediate the shape change, HCP materials are more likely to deform through mechanical twinning under external loading at room temperature compared to FCC and BCC metals[59,110]. Here we will focus on the deformation twinning in HCP metals at small length scale. Due to the low crystal symmetry, the plastic deformations of single crystalline HCP metals are typically anisotropic and thus the critical resolved shear stress for dislocation motion on a specific plane are strongly depending on the crystal orientation. However, Yu *et al.* discovered that such kind of anisotropic in plastic deformation can be significantly reduced by scaling down the crystal size[148]. In the $[10\bar{1}2]$ Mg submicron pillars, the plasticity is dominated by the basal-slip, which leads to a low strength and brittle-like fracture[148]. As the crystal size is decreased to around 100 nm, both basal-slip, prismatic-slip and pyramidal-slip are activated, which can effectively reduce the plastic anisotropic during the deformation and

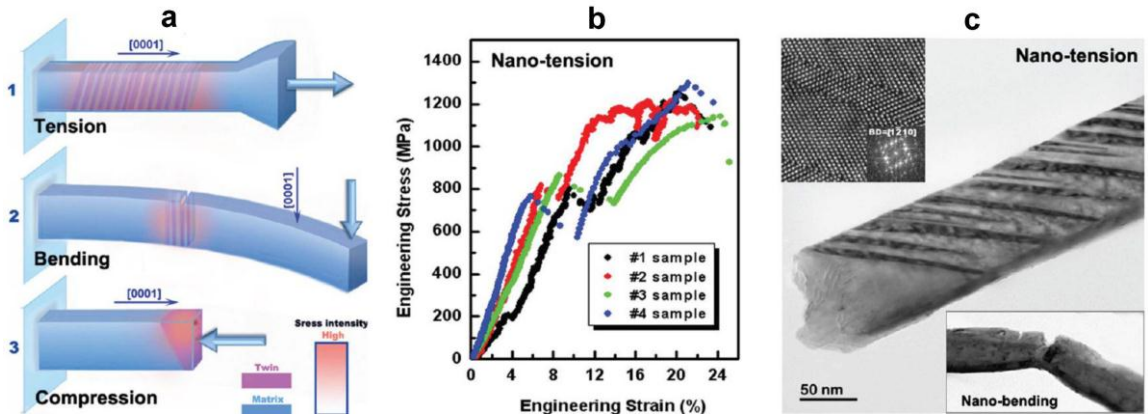

Figure 2.13 Nanostructured deformation twinning in [0001] Mg nanopillars[149]. (a) Different loadings. (b) Stress-strain curves of [0001] Mg nanopillars. (c) High density deformation twinning.

generate a more homogeneous plasticity with enhanced ductility[148]. In the orientation that suppresses the basal-slip, such as [0001], high density deformation twinning are formed under different mechanical loading (Figure 2.13)[149]. The size of those twinning are several nanometers (Figure 2.13), contributing to the so-called "twinning induced plasticity" (TWIP) and improved toughness of Mg nanopillars[149]. Moreover, deformation twinning in HCP metals also shows a strong dependence on crystal size. In the single crystalline sub-micron [0001] pillar of Ti alloy, the nucleation stress of deformation twinning increases significantly with the decrease of sample dimensions[150]. As a result, the twinning dominated plastic deformation is replaced by the ordinary dislocation plasticity below the critical size of about one micrometer[150]. Such size dependence of deformation twinning is attributed to the "stimulated slip". The theoretical study on the deformation twinning in HCP metals is rare[21], and thus will not be reviewed here.

In summary, the deformation twinning and size-dependent deformation in FCC and HCP metals at small length scale has been well-documented, both experiments and simulations; however, few is known about that of nanosized BCC metals. Whether the deformation transition

from dislocation slip to deformation twinning occurs in BCC metals remains unclear. Moreover, the atomic scale twinning mechanism in BCC and HCP metals remains unexplored at present, though the deformation of 100 nm HCP metals have been studied. Due to the challenges in obtaining the HCP metallic nanowires and their strong orientation dependence in deformation, we will focus on the BCC metallic nanowires.

2.4 MOTIVATION AND RESEARCH OBJECTIVES

"Seeing is believing". However, based on the foregoing discussions, it can be seen that current understanding of deformation at nanoscale mainly relies on the MD simulation. Limited experiment has been done concerning about the mechanical behaviors of nanomaterial, especially at the atomic scale in understanding the dislocation behaviors and deformation twinning. Revealing those real-time structural changes is critical to understand and control the mechanical degradations of high-performance nanomaterials. In present study, in-situ nanomechanical testing systems inside TEM will be used to uncover several critical issues concerning the deformation in nanosized metals:

1. Whether the dislocation can interact inside the small volume of nanowires and form the stable dislocation structure or high order defects?
2. The effects of microstructure, such as coherent twin boundaries, on the defect nucleation and plastic deformation.
3. The effects of crystal structure on the defect nucleation, propagation and annihilation via the comparisons between the deformation of FCC and BCC nanowires.
4. The orientation dependence of deformation mechanisms in nanosized BCC metals.

A fundamental understanding on the relationships between structure, mechanical properties and deformation mechanisms in nanosized metals will be obtained through the systemic studies conducted in here, which is of fundamental and technological importance for materials design and mechanical degradation control.

3.0 MATERIALS AND EXPERIMENTAL PROCEDURES

In this chapter, the experimental setup and materials used in experiments will be described. Single crystalline Au nanowires with different microstructure, *i.e.* twin-free, low density twins and ultrahigh density twins, will be used to uncover the effects of microstructure on the defect nucleation and deformation dynamics; while BCC tungsten (W), the typical BCC metals, will be studied and compared with Au to reveal the effects of crystal structure on the deformation. A novel method to fabricate the nanowires from bulk materials directly are developed inside TEM, which allows the in situ nanomechanical testing and can be applied to a wide range of materials including FCC and BCC metals. Additionally, several novel in-situ nanomechanical testing setups inside TEM will be discussed in detail in this chapter.

3.1 MATERIALS

3.1.1 Au nanowires

Due to its low electron-beam induced damage and non-oxide layer, Au will be used as the example to study the deformation of nanosized FCC metals. The synthesis of Au nanowires was based on the method reported by Wang *et al.*[9]. In a typical synthesis, 18 ml oleylamine (OAm) was heated to 60 ℃ under gentle N_2 flow. In another container, 44 mg $HAuCl_4 \cdot xH_2O$ was

dissolved in a mixture of 0.2 ml OAm and 2 ml hexane. The $HAuCl_4 \bullet xH_2O$ solution was injected into the 60 ℃ OAm and held at the same temperature for 15 hr without any disturbance such as magnetic stirring. After cooling to room temperature, 10 ml ethanol was added to precipitate the Au nanowires. Au nanowires with varied diameters and high density twins can be made from different synthesis temperatures.

Figure 3.1 shows the representative morphologies of as-synthesized Au nanowires with high density twins (UDTs). Typically, the diameter of Au nanowires presented in our study is uniform along the axial direction. Also, some variations in diameter were only observed at the two ends of the nanowires. Before carrying out the tensile test, the nanowires will be checked and samples with irregular shape specimens under TEM are "disqualified" for *in-situ* measurement. Only Au nanowires with uniform diameters and clean surfaces are chosen for the mechanical tests. High resolution TEM (HRTEM) study shows that the Au nanowires are highly twinned (Figure 3.2). However, some of the high-density TBs in the TEM images will be invisible if the view zone slightly deviates from the [110] zone axis (Figure 3.2). Au nanowires were tilted to the [110] zone axis before tensile testing for the *in situ* HRTEM study. Tensile loading was applied along the nanowire axis in the <111> direction until failure. Before testing, the nanowire ends were "glued" to the atomic force microscopy (AFM) cantilever, and therefore did not significantly contribute to the deformation and strength measurements. Furthermore, all samples failing near the nanowire ends will be excluded in the mechanical data and fracture analysis.

Au nanowires with low density twins (LDTs) and no twins are created inside the TEM by using the cold welding technique[151]. In a common welding process in bulk materials, local heating and damage are introduced, which will introduce some point defects, such as vacancy. To

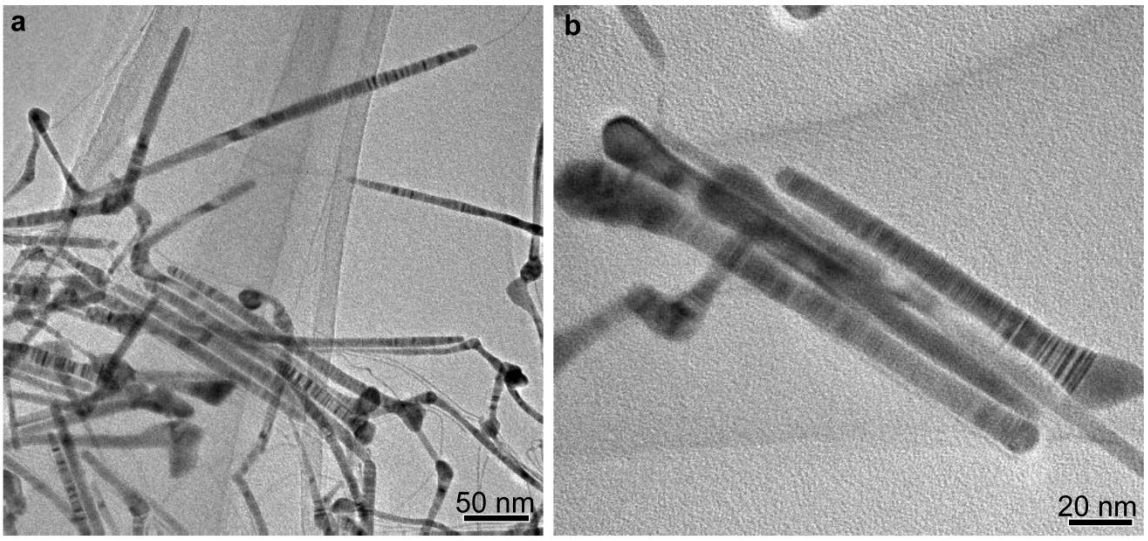

Figure 3.1 Representative morphology of as-synthesized Au nanowires with ultra-twins by TEM. The diameter of Au nanowires presented in our study is mostly uniform along the axial direction. Some variations in diameter are only observed at the two ends of the nanowires, which did not significantly affect the stress-strain measurements.[10]

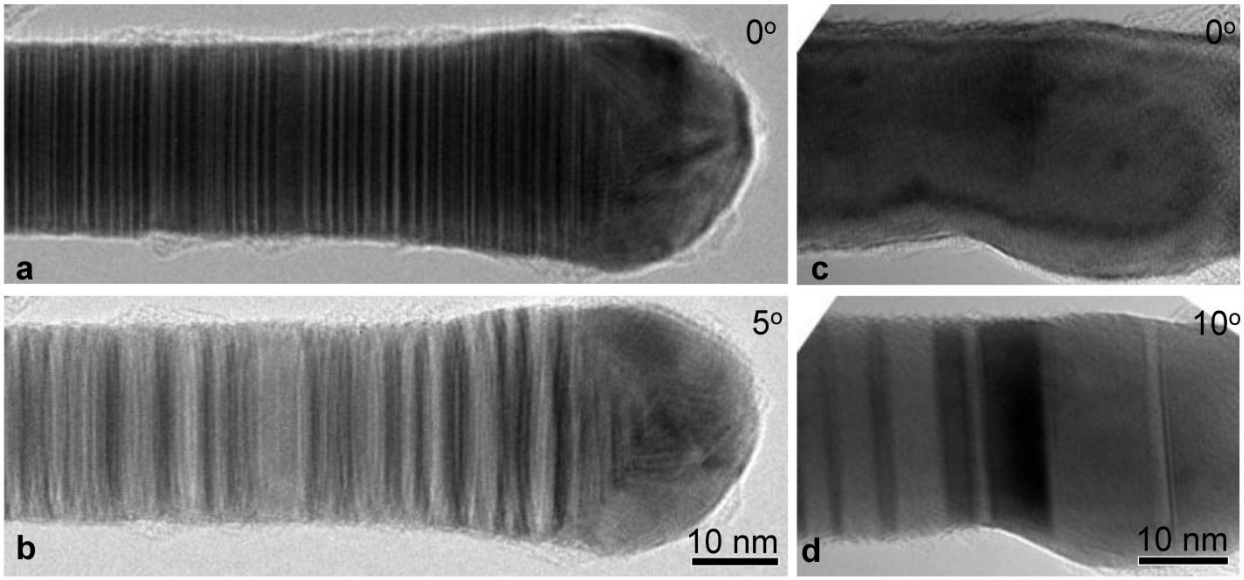

Figure 3.2 Twin morphology of Au nanowires at different tilt angles. (a) Au nanowires with UDTs in [110] zone axis. (b) After a tilt of 5° along α direction, the nanowire presents as bamboo-like structure with less visible UDTs. (c-d) The Au nanowire shows no TB at 0 °. However, several TBs appear after a tilt of 10° along α direction (d). Both of (c) and (d) are not taken perfectly in the [110] zone axis, but more TBs could show up when aligned closer to the [110] zone axis.[10]

avoid the effects of vacancies on deformation, cold welding was employed to fabricate the Au nanowires with LDTs and no twins. During the cold welding, an ultra-sharp Au probe was pushed into a single crystal Au nanoparticles or nanotooth. A strong contact can be made between Au probe and the nanoparticles or nanotooth under the drive of fast surface-atom diffusion favored by the large surface stress. As a result, the Au probe and the nanoparticles or nanotooth will be welded together by forming a nanowire between them. The Au nanowires fabricated by the cold welding showed an high strength and electrical conductivity[151]. In some cases, low density twin boundaries were formed after the cold welding, due to the plastic deformation occurred in the welding process. Mechanical measurements were further conducted by using those Au nanowires.

3.1.2 W nanowires

Polycrystalline W rods (99.98 wt.% purity, 0.010 in diameter), ordered from ESPI Metals Inc., were used for the experiments. The impurity concentrations of the W are: Cr < 10 p.p.m., Fe < 20 p.p.m., Ni < 130 p.p.m., Cu < 20 p.p.m. and K <20 p.p.m. Before the nanomechanical test, W nanowire were synthesized directly inside the TEM using a potential-induced welding process. The experiment setup is illustrated in Figure 3.3. A FEI Tecnai F30 field emission gun (FEG) TEM equipped with the Nanofactory TEM-scanning tunneling microscope (STM) platform was used to *in-situ* study the deformation mechanisms. In a typical experiment, a W rod with as-fabricated nano-sized teeth served as the one end of the platform (Figure 3.3a). A W STM probe etched with NaOH solution was used as the other end of the platform. A 2-4 V potential was applied, which, when the contact between W probe and nanotooth was made, welded the two tungsten crystals together forming either a nanosized bi-crystal or single crystal (Figure 3.3c-d).

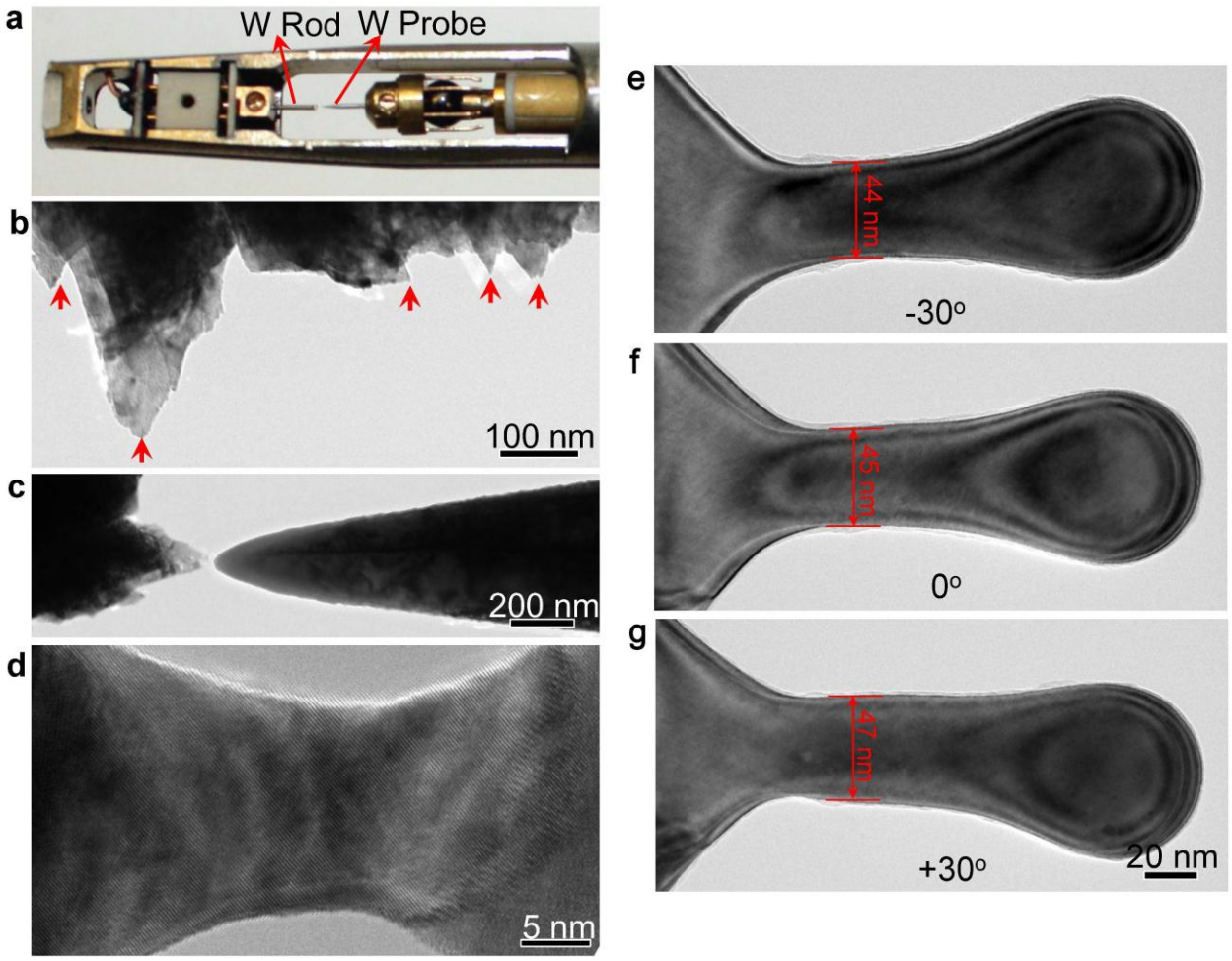

Figure 3.3 *In-situ* TEM experimental setup and the cross-section of a W nanowire. (a) The TEM-STM platform employed in our experiments. (b) The nanosized teeth on the edge of W rod. (c) The W probe was driven to contact with a nanotooth. A 3 V potential is applied on the W probe. (d) A W nanowire was formed when the contact between W probe and nanotooth was made. (e-g) The cross-section of the nanowire was determined approximately by tilting the nanowire by α from -30^{o} to $+30^{o}$. The diameter of the nanowire changes very little, which indicates that the cross-section of the W nanowire is close to circle.

The bi-crystal with a grain boundary formed due to the orientation differences between the W probe and the nanotooth. Tilting experiments showed that the cross-section of W nanowires was close to circle (Figure 3.3e-g). *In-situ* tension and compression experiments were conducted at room temperature by driving the W probe using a piezo-controller with a strain rate about 10^{-3} s^{-1}. A CCD (charge-coupled device) camera was used to record the real-time images of deformation process at 2 frames per second.

This *in situ* fabrication method is a breakthrough in making the sub-100 nm and clean metallic nanostructures, which can involve different crystal orientations/types (e.g. FCC (Au, Pt) and BCC (Mo, V and Ta)) and tunable dimensions. Considering the difficulties in handling and testing the nanomaterials, this method provides a relatively simple and novel approach to study the deformation mechanism of metallic nanomaterials, especially at the atomic scale. Moreover, this method may have potential applications in the assembly and interconnection of nanodevices.

3.2 EXPERIMENTAL METHODS

3.2.1 Experimental equipment and setups

During past 20 years, significant efforts have been made to study the mechanical behaviors of nanosized materials in TEM, scanning electron microscopy (SEM) and AFM by tensile, compression, nanoindentation and bending testing[152]. Among them, TEM is the most powerful method which allows the atomic-scale resolution. Different TEM sample holders and MEMS devices have been developed for the in situ nanomechanical testing inside TEM[44,64,152,153], however, in those experimental setups or TEM holders, the resolutions were relatively low due to

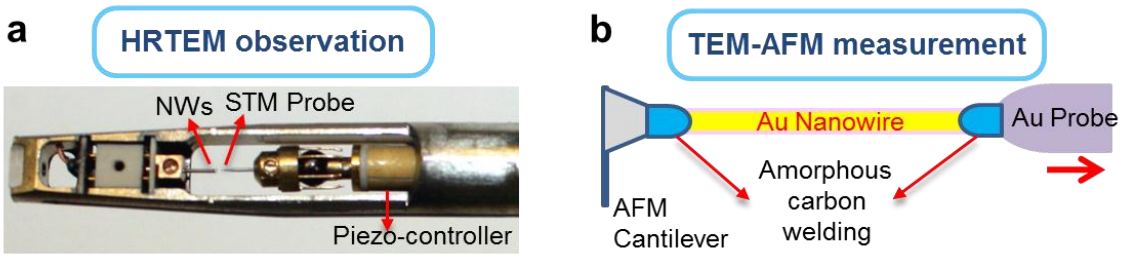

Figure 3.4 Experimental setups for (a) in situ HRTEM observations of the deformation mechanisms and (b) TEM-AFM measurement of stress-strain curves.

the mechanical vibrations and large sample sizes used. Recently, a novel TEM platform has been developed for the in situ nanomechanical testing by Nanofactory Inc. This experiment platform has high mechanical stability inside TEM, which allows the real time atomic-scale observations of deformation. In a typical experiment (Figure 3.4a), an ultrathin STM probe was employed to handle the nanosized samples (nanowires or nanoparticles). A piezo-controller was used to precisely drive the movement of the STM probe in three dimension spaces, in which the fine movement of STM probe can be as low as 0.05nm/s; as a result, the mechanical loading could be applied smoothly. Moreover, an electronic field can be added to the samples in the Nanofactory TEM-STM platform; as a result, the variations of current experiment setups might be used in the study of real time structure evolutions under external electronic potential, such as electrochemical reactions in lithium ions batteries and phase transitions in materials for memristor.

All experiments of current research project were carried out in Center for Integrated Nanotechnologies (CINT). CINT is a national user facility at Sandia National Laboratories, New Mexico, operated by the Department of Energy's Office of Science. It provides the approved users the access to its experimental capabilities for basic and applied research at nanoscale. For the in situ experiments, CINT has a FEI Tecnai F30 TEM and several in situ TEM holders for

different studies, such as Nanofactory TEM-STM holders for nanomechanical testing and nanomanipulation, Protochip TEM holder for in situ heating experiment and Hummingbird liquid cell TEM holder for electrochemical study. The point resolution of the FEI Tecnai F30 TEM is ~0.2 nm, making it a good candidate for the high resolution observations. Other experimental facilities at CINT, e.g. scanning electron microscopy (SEM), ion milling and glove box, also provide a good opportunity for the in situ nanomechanical experiments proposed in this research project. Finally, A user proposal was submitted and approved to access those user facilities.

During experiments, two different experimental setups are used for the nanomechanical testing, as shown in Figure 3.4. First, a Nanofactory TEM-STM platform with a STM probe (Au or W, depending on the materials used in experiments) was used to study the deformation mechanisms under *in-situ* HRTEM (Figure 3.4a). Before tensile testing, the nanowires were tilted into the suitable zone axis for different nanowires. Strong contacts between the samples and the probe were made by cold welding, potential induced welding or depositing amorphous carbon at the contact area, depending on materials. Tensile loading was applied along the axial direction of nanowire with an estimated strain rate of ~ 10^{-3} s^{-1}. Second, the Nanofactory TEM-STM platform with an AFM cantilever (App. Nano Inc.) serving as a force sensor was used to measure the stress-strain curves of Au nanowires (Figure 3.4b). The spring constant (k) of the cantilever is calibrated as 28 N/m. For the BCC nanowires, the stress-strain curve cannot be measured due to the difficulty in obtaining the tungsten AFM cantilever.

Before experiments, the nanowires were attached to a piezo-controlled STM probe by conductive epoxy and then driven to approach the cantilever or the other STM probe. Finally, they were welded together by cold welding[151] or amorphous carbon deposition at the contact area

via the illumination of low intensity electron beam. Subsequently, the nanowire was pulled back. The real-time images of sample elongation and the deflection (Δd) of cantilever were recorded by a CCD camera at 2 frames per second. The tensile loading force (F) is directly calculated by timing the deflection Δd by its spring constant k. The engineering stresses were calculated by using the formula $\sigma = 4F/\pi d^2$, where d is the nanowire diameter, and assuming that the nanowires have a quasi-circular cross section. The engineering strains were further calculated by measuring the real-time length of the nanowires from TEM images.

3.2.2 Defect identifications

The impurity atoms, such as oxygen and carbon, might be introduced into the Au and W nanowires during their synthesis processes. The impurity atoms can generate some local stress/strain field, and the high impurity levels can significantly change the mechanical properties and deformation mechanisms of materials. Thus, the impurity levels should be identified before the experiment. The electron energy-loss spectroscopy (EELS) spectra equipped in TEM is a good method to identify the impurity levels. In EELS, inelastic scattering occurs during the electrons passes through the materials studied, leading to the energy loss of those electrons. The amount of energy loss of electrons contains the elemental components information of the materials, which will be detected and analyzed. The detection limit of EELS in the TEM used for experiment is ~ 100 p.p.m. in weight percentage. During experiments, EELS spectra of Au and W nanowires were detected and analyzed. However, no observable oxygen and carbon signals were observed in their EELS spectra, suggesting very low levels of oxygen and carbon impurities in the as-fabricated nanowires. Thus, the effects of those impurities on the deformation were not considered during the studies.

After experiments, the different deformation induced defects were identified based on the atomic-scale lattice structure in HRTEM images[53]. Figure 3.5 show some examples on the defects identifications. In those HRTEM images, each atomic column can be identified, and any lattice irregularity can be easily observed. Figure 3.5a shows the unit cell of FCC materials. All the defects in FCC metals are located on the (110) planes and the favorable viewing direction is along [110]. Figure 3.5b shows an example of perfect dislocation in FCC unit cell. An extra lattice plane was observed in the upper part of the crystal, which is a perfect edge dislocation with the core marked out by an inverted "T". Its Burgers vector b (red arrow) was identified based on the Burgers circuit. In the small volume FCC metals, the plastic deformation is dominated by the leading and trailing partial dislocations with a stacking fault embedded between them. Figure 3.5c shows an example of the stacking fault. It can be seen that the stacking sequence of FCC lattice changes into a localized stacking order of HCP structure, i.e. from ABCABC to AC, suggesting a stacking fault in the deformed FCC metals. The identification of stacking fault tetrahedra (SFT) was conducted based on the stacking fault. A deformation twinning was presented in Figure 3.5d, which shows a mirror symmetry between the crystals on the two side of twin boundary. Fast- Fourier transformation (FFT) and inversed-FFT also can be used to further identify the symmetry between the defect and matrix. The above discussions demonstrate that HRTEM images can be used for the defects identification in different crystal structures. It should be noted that the deformation twinning in BCC metals occur on (112) plane, thus the analysis should be conducted in [110] zone axis. Moreover, the screw dislocations in BCC metals are difficult to be imaged due to their non-planar core. As a result, only edge component of the dislocations are studied in BCC metals in Chapter 6.

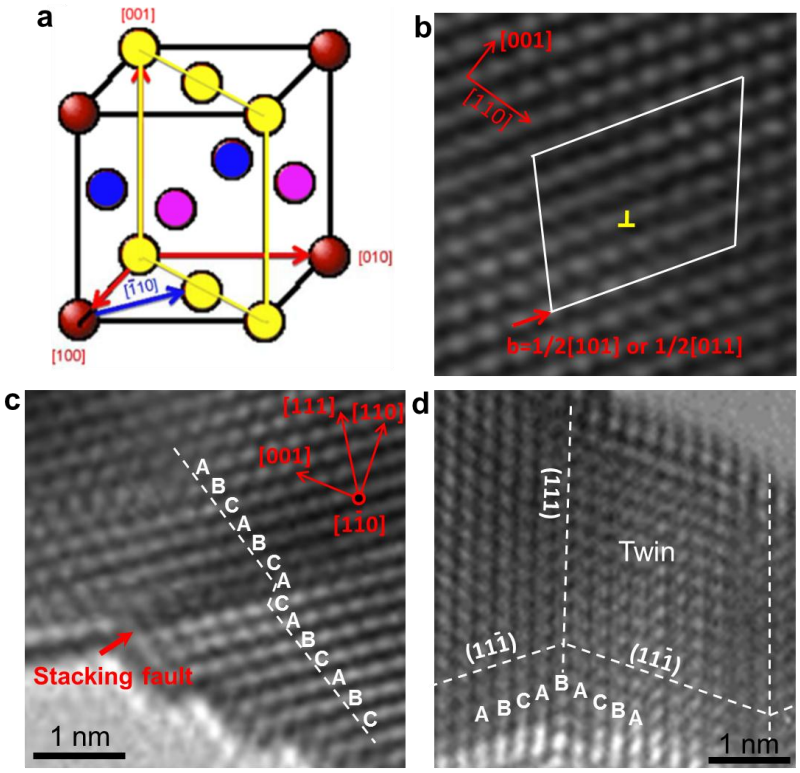

Figure 3.5 Identification of defects in FCC Au nanocrystal. (a) A FCC unit cell[53]. (b) A HRTEM image showing a pure edge dislocation in an Au nanocrystal. (c) Local stacking sequence in a stacking fault in Au nanocrystal. (d) Deformation twinning in Au nanocrystal.

3.3 SIMULATION METHODS

MD simulations were used to further understanding the experimentally-observed deformation mechanisms in Au and W nanowires, which were conducted by my collaborators. The simulations on the formation and dynamic processes of deformation-induced SFT in Chapter 4 were conducted by Dr. Ting Zhu and Mr. Sankar Narayanan in Georgia Institute of Technology; the simulations about the deformation of nanotwinned Au nanowires in Chapter 5 were conducted by Dr. Frederic Sansoz in The University of Vermont; the twinning mechanisms and dislocation mediated plasticity in W nanowires in Chapter 6 were carried out by Christopher R.

Weinberger in Drexel University (Figure 6.1), Dr. Ting Zhu and Mr. Zhi Zeng in Georgia Institute of Technology (Figure 6.5, 6.8 and 6.9). The MD simulation methods are summarized in the following.

3.3.1 MD simulations on deformation-induced dislocation-originated SFT

Three-dimensional MD simulations were carried out using LAMMPS[154]. The Embedded Atom Method (EAM) potential developed by Grochola *et al.*[155] is used to account for the many-body interactions between Au atoms. The Au nanowires simulated are aligned along the [111] direction, along which periodic boundary condition is applied. The nanowires are geometrically cut in double conical shape of length 28.26 nm instead of perfectly cylindrical ones; the diameters of the largest and smallest cross sections are 6 nm and 4 nm, respectively. This is done with the motivation of utilizing the stress concentration at the neck to promote sequential dislocation nucleation events instead of a large number of simultaneous nucleation events as would otherwise be observed in perfectly cylindrical single-crystal specimens. The nanowires are simulated with temperature T = 1K and loaded at a constant strain rate of 10^7 s^{-1}. The SFs in Figure 4.2, 4.4 and 4.6 are visualized by colouring the atoms based on the centro-symmetry parameters, while Figure 4.3 is based on the coordination numbers[156]. Figure 4.2e is plotted by reducing the atom sizes, so as to obtain the projected images of atoms on the white background of the paper, resembling the HRTEM image. To study the size effect, MD simulations are also carried out on a larger Au nanowire with the diameters of the largest and smallest cross sections being 10 nm and 6 nm, respectively. The generality of the SFT formation mechanism is verified by MD simulations of Cu nanowire. The simulation methodology and the geometry of the Cu nanowire are similar to those of Au nanowires. A recent EAM potential is used for Cu[157].

3.3.2 MD simulations on the deformation of nanotwinned Au nanowires

MD simulations were performed using the software LAMMPS[154] with an embedded-atom-method potential for Au by Grochola *et al.*[155]. It is noted that this potential was developed to simulate the growth and morphology of Au nanoparticles based on first-principles calculations, and therefore accurately predicts the stacking fault and surface energies of this metal. Twelve realizations with uniform ultrahigh density twins (UDTs) using different periodic lengths (68 nm and 270 nm), different twin densities ($0.7 \leq \lambda \leq 5.6$ nm), and different surface structures (perfectly circular and {111} microfaceted morphologies) were performed. [111]-oriented, periodically-twinned nanowires with a uniform λ were constructed by stacking platelet-like grains with a truncated octahedral shape made only by {111} surface facets. Due to UDTs, this type of structure produced smooth sidewalls with atomic facets similar to those observed in experiments in Figure 5.1. Cylindrical nanowires with same λ were also modelled with a circular cross section in order to characterize the effect of surface morphology. Each twin plane was perpendicular to the nanowire axis along the [111] crystallographic direction. Periodic boundary conditions were imposed along the nanowire axis, while the sides were kept free in all other directions. The diameter and periodic length were equal to 12 nm and 68 nm, respectively, for all wires. The time step was 2 fs. Each model was relaxed for 40 ps prior to deformation under zero pressure using an isothermal–isobaric (NPT) ensemble with a Nose-Hoover thermostat at 300 K ± 2 K. Temperature was rescaled after 500 steps. The nanowire was deformed in tension by stretching the simulation box at a constant engineering strain rate of 1×10^{8} s^{-1} along the [111] direction in the canonical (NVT) ensemble at the same temperature. Atomic-level snapshots of nanowire deformation were studied using the bond angle analysis and the local shear strain

calculation in the atomic visualization software Ovito[158]. The Virial theorem and deformed atomic volume were used to calculate the axial stress in the nanowires. Stress-strain calculations were based on the periodic lengths and average diameter, and did not take into account the local deformation due to necking. Error in strain calculations was limited because the simulations were performed at a constant engineering strain rate. However, caution was exercised in dealing with the stress values obtained after the onset of necking.

Moreover, it is noticed that the strength (5.5 GPa) of nanowires with UDTs predicted in simulations is higher than in experiments. The strain rate effects inherent to MD simulations could be a factor. Another reason is that the interatomic potential used in our simulations could largely overestimates the ideal strength of {111}<112> slip in Au (1.73 GPa) compared to more accurate *ab-initio* simulations (1.42 GPa)[159]. Thus, the ideal strength of 5.5 GPa predicted by our MD simulations should be viewed as an upper limit for the ideal strength of <111>-oriented Au crystals.

3.3.3 MD simulation on the deformation mechanisms of W nanocrystals

The twinning deformation (in Figure 6.1), detwinning deformation (in Figure 6.5) and dislocation shear deformation in W nanowires were obtained by MD simulations. The MD simulations were performed by using LAMMPS. The temperature of the system was maintained at 300K and the time step was 1fs. The Ackland-Thetford-Finnis-Sinclair potential was used to describe the interatomic forces. In the simulations of $[\bar{1}10]$ loading, a constant compressive strain rate of 10^8 s^{-1} was applied to generate twinning deformation. After the twin band formed, a constant tensile strain rate of 10^8 s^{-1} was applied to generate detwinning deformation. In the

simulations of [112] loading, a constant compressive strain rate of 10^8 s^{-1} was applied to generate dislocation shear deformation. All of the nanowires have circular cross sections. Some of the nanowires have uniform diameter along the nanowire length, while the others were constructed by creating a tapered solid of revolution about the nanowire axis. To create the bi-crystal, a $\langle 111 \rangle$ and $\langle 110 \rangle$ oriented single crystals (see Figure 6.1k for complete orientations) were created next to each other and allowed to bond through the nature of the interaction forces.

The twin embryo (in Figure 6.8 and 6.9) in W nanowires was first created under constraints and then fully relaxed by molecular statics simulations using LAMMPS with the conjugate gradient (CG) algorithm. To create a twin embryo, a pristine W nanowire was compressed to 4% so as to generate the internal stress to facilitate the twin formation. Then, a twin embryo was embedded into the nanowire through the following procedures: (a) A patch of five layers of atoms in favored $\{112\}$ planes were selected near the side face of the nanowire. (b) Each layer of atoms were moved by a prescribed displacement along the favored twin direction as follows: the displacement for the first layer was $1/3\langle 111 \rangle$, the second was $1/6\langle 111 \rangle$, the third was 0, the forth was $-1/6\langle 111 \rangle$ and the fifth was $-1/3\langle 111 \rangle$. (c) The nanowire was relaxed by CG while the displaced atoms in the patch were constrained from moving. Under such constrained relaxation, an incipient twin embryo was formed in the nanowire. (d) The constraints on atoms in the patch were removed and the system was fully relaxed. As a result, the twin embryo can be created in both the $[\bar{1}10]$ and [112] nanowires.

4.0 ATOMIC-SCALE DYNAMIC PROCESS OF DEFORMATION-INDUCED STACKING FAULT TETRAHEDRA IN GOLD NANOCRYSTALS

In this chapter, the dislocation dynamics inside the small volume of Au nanowire will be studied. It is well-known that smaller is stronger[19,37] and the widely-observed size effect is believed to arise from dislocation interactions inside nanocrystals[43]. However, the interaction mechanisms in the small-volume nanocrystals remain unexplored due to technical challenges. Moreover, it is still unclear whether the three-dimensional (3D) volume defects of stacking fault tetrahedra (SFT), the three-dimensional crystalline defects bounded by stacking faults and stair-rod dislocations which are often observed in quenched or irradiated face-centered cubic metals and alloys, can be generated by pure mechanical deformation since all of the SFT experimentally observed till date are supposed to originate from vacancies[59]. Combining in-situ high resolution TEM with atomistic modeling, it discovers that the surface-nucleated dislocations can strongly interact with each other inside the confined volume of Au nanowires. These interactions lead to a new type of dislocation-originated SFT, in distinct to the widely believed vacancy-originated SFT. The complete atomic-scale processes of nucleation, migration and annihilation of dislocation-originated SFT are revealed to conduct in the manner that is not expected in bulk samples. These results uncover a unique deformation mechanism via dislocation interaction inside the confined volume of nanocrystals, and have important implications regarding the size effect on the mechanical behavior of small-volume materials.

4.1 INTRODUCTION

Plastic deformation in metals and alloys is governed by the generation and evolution of defects of point, line, plane and volume types[59,86]. Among these defects, SFT, bounded by stacking faults (SFs) and stair-rod dislocations, are a peculiar type of volume defect typically found in FCC crystals with low stacking fault energy[59,160]. Generally, SFT can be introduced by three methods, *i.e.* quenching, high-energy particle irradiation and plastic deformation[160-165]. In 1959, Silcox and Hirsch[161] first observed SFT in quenched Au. They proposed that SFT were formed from the Frank dislocation loops generated by collapsed vacancy clusters, which further dissociated through the Silcox-Hirsch mechanism[59,161] to produce the 3D SFT. Since then, extensive studies have been conducted on the vacancy-originated SFT in quenched, irradiated, or plastically deformed bulk FCC crystals[160-181]. However, whether the SFT can be possibly initiated by dislocations without the aid of vacancies remain largely unexplored. If possible, how do SFT form, migrate and annihilate, particularly at the nanoscale?

It is well known that the smaller tends to be stronger[19,37] and the free surface in nano-sized crystals acts as an effective source of dislocations[10,43,53]. However, surface nucleation only leads to a weak size effect on the strength of nanocrystals[43,182], e.g., the predicted logarithmic scaling of strength versus nanopillar/nanowire diameter, as opposed to the measured power law scaling. Hence, the widely-observed size effect is generally believed to arise from dislocation interactions inside nanocrystals. Moreover, the study of plasticity in nanocrystals has until now been focused on one-dimensional (dislocation) and two-dimensional (grain boundary) defects[10,41,43,45,53,183]. It remains unclear if higher order defects, such as the 3D volume defect of SFT, can be generated inside the confined volume of nanocrystals by pure mechanical

deformation. Furthermore, since the sources of partial dislocation are abundant at the surface[10,43,53], they might facilitate the interactions between partials and SFT in the small volume of nanocrystals. It is thus expected that the dynamic evolution of the SFT might be uniquely mediated by SFs in the nanoscale regime. However, due to technical difficulties in controlling the samples at the nanoscale, it has been a challenge to directly explore the dislocation interaction, as well as the formation and evolution of higher order defects, in small-volume nanocrystals.

Here, *in situ* HRTEM observation shows that the dislocation can strongly interact with each other inside the small volume of nanocrystal and higher order defects, such as SFT, can be can be produced in nanocrystals directly through dislocation interactions and cross-slip, which are further confirmed by the large scale MD simulations. The presence of vacancies that is critical for the initiation of SFT in the bulk is no longer a pre-requisite for the SFT formation in the nanoscale. The SFT formed in the nanocrystals is termed as 'dislocation-originated' SFT, specifically due to its origin being solely controlled by dislocation interaction events. Moreover, the migration and annihilation of the dislocation-originated SFT are proved to be a direct outcome of dislocation-SFT interactions.

4.2 EXPERIMENTAL PROCEDURES

The details of the experimental procedures were described in Chapter 3. The growth direction of as-synthesized Au nanowires is along the [111] direction, with few TBs parallel to the cross section of nanowires. The tensile experiments were conducted inside a TEM equipped with a Nanofactory TEM-STM holder. Before tensile testing, the Au nanowires were tilted into the

$[1\bar{1}0]$ zone axis and a strong contact between the Au nanowire and STM probe was made by depositing amorphous carbon at the contact area. Tensile loading was applied along the [111] direction with an estimated strain rate of ~ 10^{-3} s^{-1}. Moreover, cold welding method[53] was used to prepare some samples with the loading directions of [111] and others. In the typical cold-welding process, the Au STM was driven forward with a speed of 1~2 nm/s by a piezo-controller, while the linear size of deformation-affected area was about 10 nm, thus the strain rate of the cold-welding process was estimated to be on the order of 0.1 s^{-1}. The determination of dislocation types in HRTEM images was based on the method discussed by Zheng *et al.*[53].

4.3 EXPERIMENTAL RESULTS

4.3.1 Formation of dislocation-originated SFT by dislocation interactions

Figure 4.1 show the formation of a dislocation-originated SFT through the interactions of partial dislocations in an Au nanowire. The Au nanowire is 16 nm in diameter and contains a growth twin boundary. It is loaded along the [111] direction and viewed along the $[1\bar{1}0]$ direction (Figure 4.1a). During tensile deformation, the partial dislocation typically nucleates from the free surface and moves into the Au nanowire (Figure 4.1b), which is consistent with our previous experimental observations[10,53]. It is observed that several SFs nucleate sequentially at different sites of the free surface. They glide on the equivalent, inclined {111} planes (denoted as SF_1, SF_2 and SF_3, respectively) and interact with each other inside the Au nanowire, forming a wedge and then a zigzag dislocation structure (Figure 4.1c-d). Such interaction between SFs are the first step

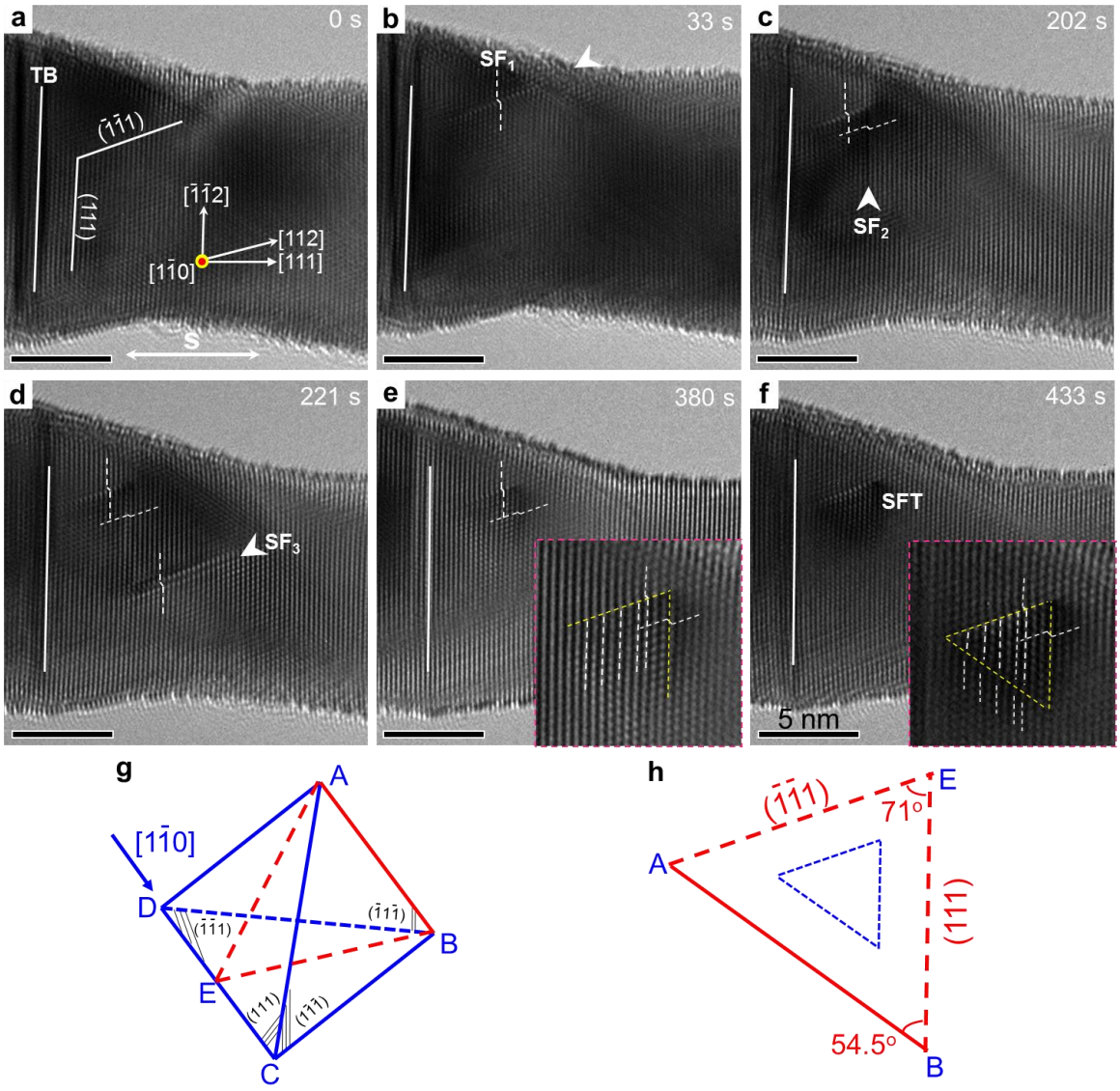

Figure 4.1 Formation of dislocation-originated SFT. (a) Crystallographic orientation of the Au nanowire. The nanowire diameter is ~16 nm. (b-f) Sequential HRTEM images showing the evolution of dislocation structure and the formation of a dislocation-originated SFT via the interactions of partial dislocations under [111] tension. Upon tensile loading, the partial dislocations with SFs nucleate sequentially from free surface on the equivalent inclined {111} planes and interact with each other, forming a wedge (c) and then a zigzag (d) dislocation structure. (e) At 380 s, SF_3 propagates and annihilates at free surface, leaving behind the wedge structure. The inset shows the enlarged image of the wedge structure (yellow dashed line). (f) The wedge structure further evolves into a triangular defect, which is identified to be an SFT (marked out by the yellow triangle in inset). (g-h) Projected view of SFT along $[1\bar{1}0]$ direction.[184]

step of the formation of dislocation-originated SFT. As the tensile load increases, SF_3 starts to move and eventually annihilates at the free surface, leaving behind a wedge structure between $SF_1$and SF_2 (Figure 4.1e). This wedge structure involves both SF_1 and SF_2 with a 1/6<110>-type stair-rod dislocation at the intersection between the two SFs (inset in Figure 4.1e). It further evolves under the applied load, resulting in a 2-3 nm sized triangular defect (as indicated by the yellow triangle in the inset of Figure 4.1f). Such triangular defect is identical to the projected view of SFT along the $[1\bar{1}0]$ direction, in both its shape and geometric angles (Figure 4.1g-h). Moreover, the morphology of this triangular defect appears to be the same as that of the vacancy-originated SFT reported in the literature[163,169,185]. Based on the experimental observation, an interaction-cross slip mechanism of dislocation is proposed for the SFT formation, which will be discussed later with MD simulation.

Figure 4.2 shows the formation of dislocation-originated SFT via dislocation interactions in an Au nanowire, as realized in our MD simulations. The Au nanowire is subjected to tensile loading along the [111] axial direction. Similar to our experimental observation, a leading partial dislocation of 1/6<112>-type and of a Schmid factor of 0.31 (denoted as βA in Figure 4.2f) is seen to nucleate from the nanowire surface; and it propagates on the $(\bar{1}\bar{1}1)$ plane, leaving SF_1 behind (Figure 4.2a). Subsequently, two new partial dislocations, denoted as δA and γA (and with the same Schmid factor of 0.31) are triggered on the $(\bar{1}1\bar{1})$ and $(\bar{1}\bar{1}1)$ planes, respectively, enclosing SF_2 and SF_3 (Figure 4.2b,f). Note that SF_3 is covered visually by SF_1 and SF_2 and thus cannot be seen in Figure 4.2b-c. Partials of δA and γA propagate into the nanowire and lock with βA, forming three 1/6<110>-type sessile stair-rod dislocations, denoted as $\beta\gamma$, $\delta\beta$ and $\gamma\delta$ in Figure 4.2f. The dislocation reactions can be expressed as:

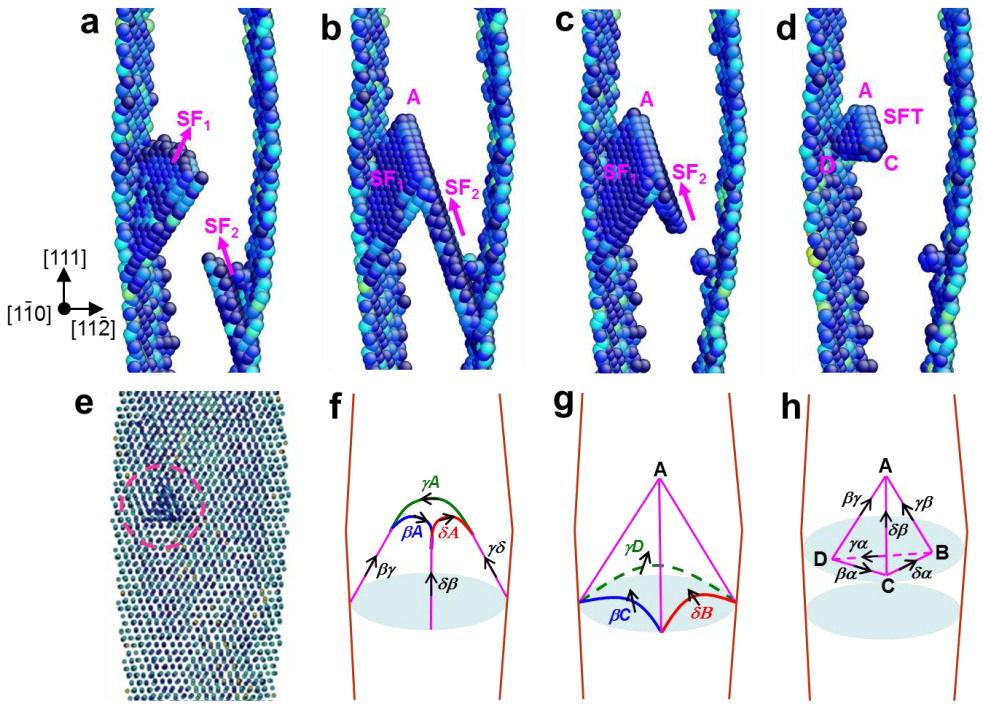

Figure 4.2 Formation of dislocation-originated SFT in MD simulation. The Au nanowire is loaded in the [111] direction. (a) A leading partial with trailing SF_1 nucleates from the free surface on the $(\bar{1}\bar{1}1)$ plane under tensile loading. (b) Two new SFs, SF_2 and SF_3, nucleate on the $(\bar{1}1\bar{1})$ and $(1\bar{1}\bar{1})$ plane respectively, and intersect with SF_1, forming the initial open-SFT. Note that SF_3 is covered visually by SF_1 and SF_2 and thus cannot be seen directly. (c) The nucleation of trailing partials sweeps out part of the SFs, thus removing the trails of the initial open-SFT. (d) The closed SFT finally forms by dislocation cross-slip. (e) Projection view of the closed SFT along the <110> direction. (f-h) Schematic illustration of the detailed dislocation processes during the SFT formation.[184]

$$\frac{1}{6}<\bar{1}2\bar{1}>+\frac{1}{6}<1\bar{1}2>\rightarrow\frac{1}{6}<011> \qquad (\beta A+\gamma A\rightarrow\beta\gamma;\ \delta A+\beta A\rightarrow\delta\beta;\ \gamma A+\delta A\rightarrow\gamma\delta)$$

These sequential dislocation nucleation and interaction events create an initial 'open-SFT' with only three completed faces (Figure 4.2b). Under further tensile loading, the trailing partial dislocations βC, δB and γD, which have a Schmid factor of 0.16, nucleate as in Figure 4.2g, the propagation of which eliminates a part of the SFs on each of the three faces of the open-SFT (Figure 4.2c,g), thus removing the trails of the initial open-SFT. A closed-SFT finally forms via

the cross-slip of one of the trailing partials into the open (111) plane, producing SF_4 that constitutes the base of the closed-SFT; the three 1/6<110>-type sessile dislocations $\beta\alpha$, $\delta\alpha$ and $\gamma\alpha$ enclose the base of the closed-SFT (Figure 4.2d,h). The dislocation reactions can be expressed as:

$$\delta B \xrightarrow{cross-slip\ into\ BCD} B\alpha, C\alpha, D\alpha$$

Each of the three partials in BCD react with the other trailing partials to form the three stair-rod dislocations $\beta\alpha$, $\delta\alpha$, and $\gamma\alpha$, constituting the base BCD of the SFT:

$\gamma D + D\alpha \rightarrow \gamma\alpha$ (along BD)

$\beta C + C\alpha \rightarrow \beta\alpha$ (along DC)

$\delta B + B\alpha \rightarrow \delta\alpha$ (along CB)

Figure 4.2e shows the projected image of the SFT in Figure 4.2d as viewed along the <110> direction, which is same as the experimental observation under HRTEM in Figure 4.1f.

The structure of the dislocation-originated SFT is compared with the vacancy-originated SFT. Figure 4.3a presents the schematics of intrinsic and extrinsic SFs by using a line of atoms with the single and double faults of stacking along the close-packed direction of <110>. With such schematics as reference, it is evident that the SFs (e.g., SF_1 and SF_2) in a dislocation-originated SFT are of the intrinsic type (Figure 4.3b), each of which involves only one faulted plane of stacking. In Figure 4.3c, a vacancy-originated SFT is "artificially" created in a nanowire by relaxing a triangular vacancy loop (i.e., a Frank loop)[169,174]. Each of the SFs also involves only one faulted plane of stacking, and thus is of the intrinsic type. The minor differences in colour between the two types of SFT arise owing to the fact that the former is subjected to a large tensile stress, while the latter is stress free. Comparisons between the two types of SFT prove that the dislocation-originated SFT is structurally equivalent to the vacancy-originated SFT

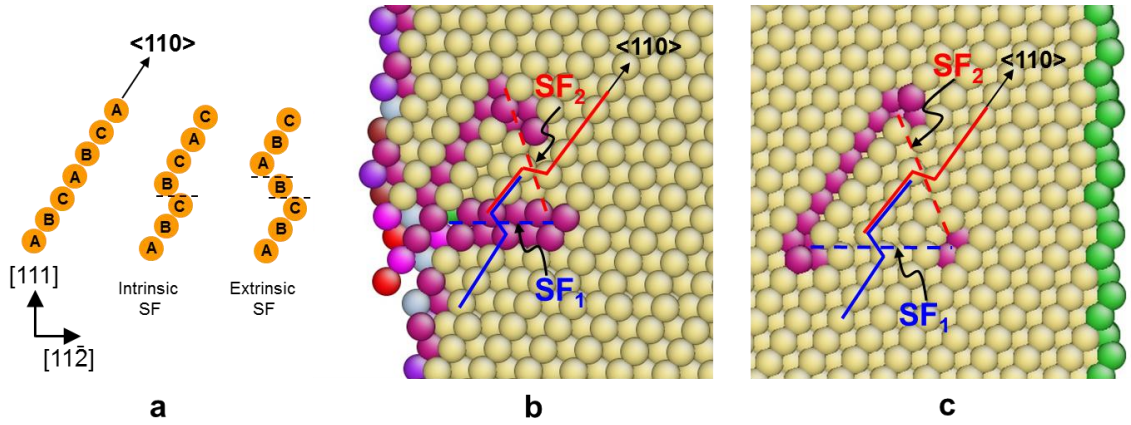

Figure 4.3 Crystallographic structure of the dislocation-originated and vacancy-originated SFT. (a) Schematic representation of the intrinsic and extrinsic stacking faults in terms of the A/B/C atomic layer stacking, as well as the single and double kinking (faults) along the close-packed direction of <110>. (b) {110} cross section of a dislocation-originated SFT, with atoms colored by their coordination numbers. (c) Same as (b) except for a vacancy-originated SFT formed via the Silcox-Hirsch mechanism.[184]

. However, the dislocation-originated SFT can play an important role in controlling the plasticity of FCC metallic nanostructures (see the Discussion).

4.3.2 Migration of dislocation-originated SFT

Similar to the Lomer-Cottrell lock, the SFT is bounded by SFs and stair-rod dislocations[59], and is usually sessile. In nanocrystals, however, the SFs are frequently nucleated from the surface and could induce migration and annihilation of the dislocation-originated SFT by dislocation-SFT interactions. Figure 4.4 show the migration of a dislocation-originated SFT during tensile deformation of an Au nanowire. In this case, two dislocation-originated SFT (SFT_1 and SFT_2) are produced sequentially via partial dislocation interactions (Figure 4.4a). Upon further loading, a group of partial dislocations, which consists of four leading partials on the adjacent $(\bar{1}\bar{1}\bar{1})$ planes

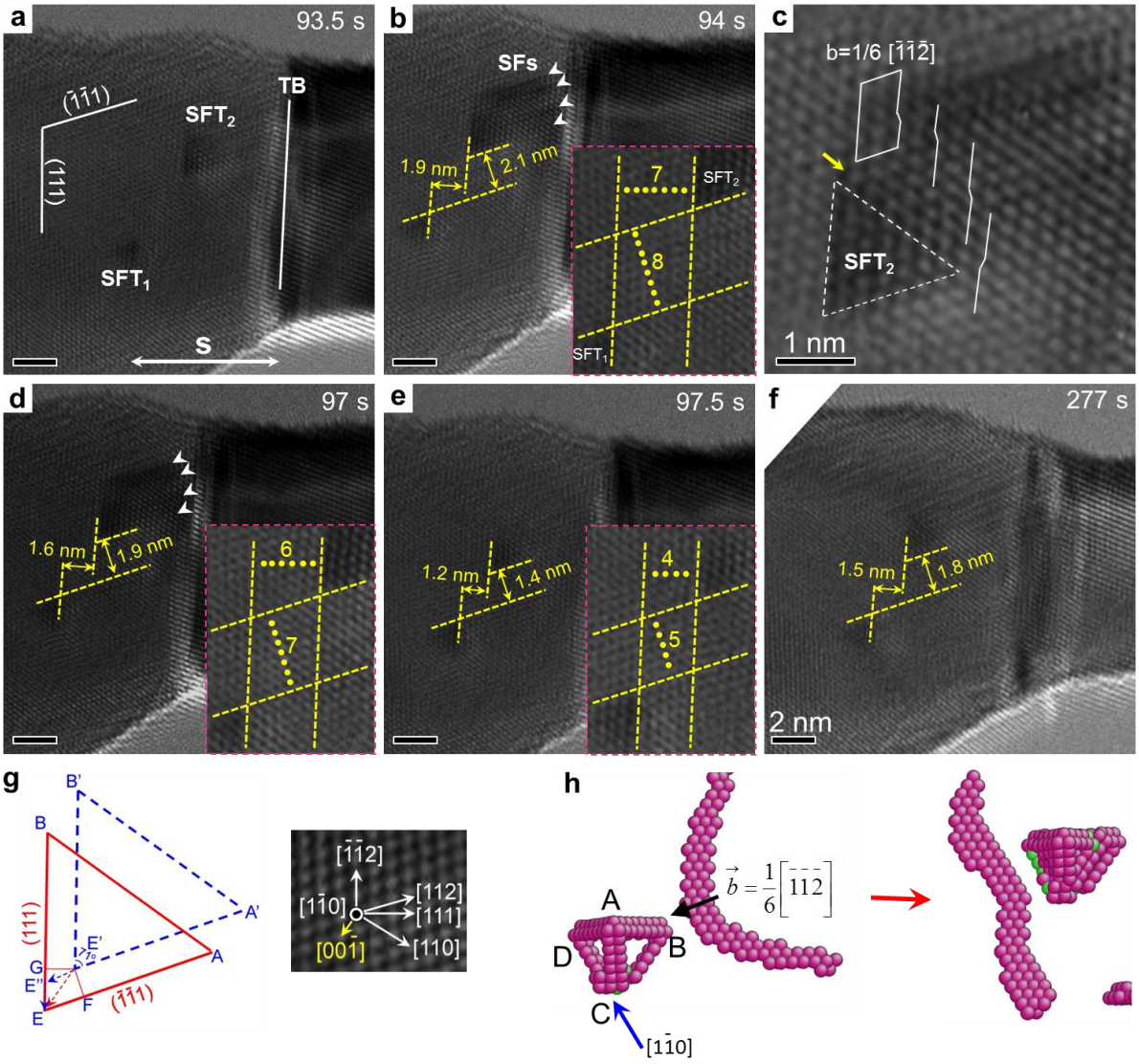

Figure 4.4 Migration of dislocation-originated SFT during deformation. (a) Under tensile loading, two dislocation-originated SFTs (SFT_1 and SFT_2) are produced sequentially. (b) Upon further deformation, a group of partial dislocations (indicated by the white arrows) nucleate from the TB and interact with SFT_2. (c) Structure of the partial dislocations group, which consists of four parallel leading partials with SFs. The yellow arrow indicates the strain contrast induced by dislocation-SFT_2 interaction. (d-f) The dislocation group drives SFT_2 to migrate, as indicated by the changes of distance and atomic layers between SFT_1 and SFT_2 on the (111) and $(\bar{1}\bar{1}\bar{1})$ plane, respectively. Insets in (b) and (d-e) are the changes of atomic layers between SFT_1 and SFT_2 on the (111) and $(\bar{1}\bar{1}\bar{1})$ plane, respectively. (g) Migration direction of SFT_2. (h) Interaction of a partial dislocation with SFT and the surface step on SFT created by the interaction.[184]

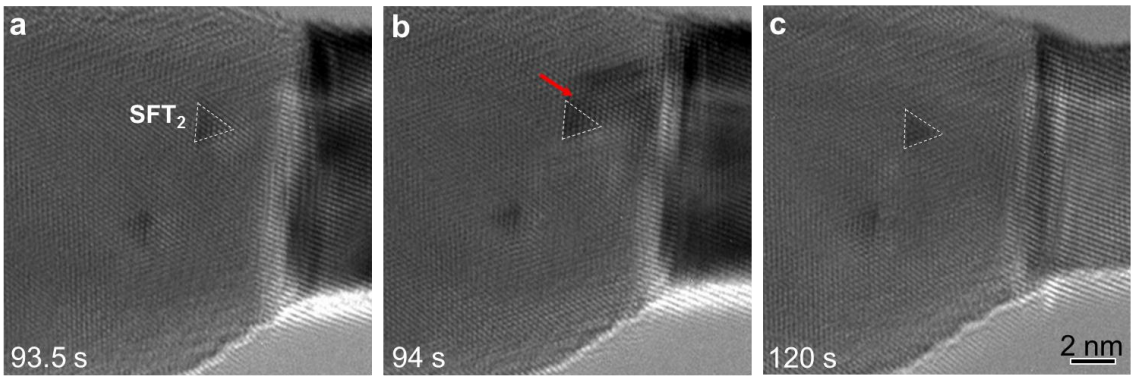

Figure 4.5 Comparison of the size of SFT_2 before and after migration. TEM images of (a) Figure 4.4a; (b) Figure 4.4b; (c) Figure 4f. Red arrow in (b) indicates the strain contrast induced by dislocation-SFT_2 interaction. It can be seen that the size of SFT_2 does not change after migration.[184]

(Figure 4.4c), nucleates from the TB at a nucleation stress of about 2.3 GPa and interacts with SFT_2 (Figure 4.4b). The dislocation group drives the migration of SFT_2 along the $[00\bar{1}]$ direction, which can be seen from the changes in the distance (or the number of atomic layers) between SFT_1 and SFT_2 (Figure 4.4b-f and 4.4g). In the beginning, the measured distance between the two SFT on the (111) and $(\bar{1}\bar{1}1)$ planes is respectively 1.9 nm and 2.1 nm (Figure 4.4b), corresponding to 7 and 8 atomic layers (inset in Figure 4.4b). Subsequently, the interaction between the dislocation group and SFT_2 reduces the distance between the two SFTs (Figure 4.4d). Finally, after the dislocation group is annihilated at the free surface, the distance between the two SFT decreases respectively to 1.2 nm and 1.4 nm on the (111) and $(\bar{1}\bar{1}1)$ planes (Figure 4.4e), corresponding to 4 and 5 atomic layers (inset in Figure 4.4e). The measured changes in the distance between the two SFT match well with the distance between the corresponding atomic layers. Interestingly, the distance between the two SFT increases after a further increase of

tensile loading (Figure 4.4f). It is worth pointing out that the size and shape of SFT_2 remain unchanged before and after its migration (Figure 4.5).

The migration of dislocation-originated SFT can, in principle, result from thermal or mechanical activation. Migration of dislocation loop and vacancy cluster has been observed in irradiated or quenched metals[185-187], the reason for which is attributed to thermal activation[187]. In the present experiment, thermal activation is unlikely, since the migration is only observed when a group of dislocations interact with the SFT. Therefore, we attribute the migration of SFT to the activation by mechanical stress that leads to dislocation-SFT interactions. It is known that due to applied loads, the vacancy-originated SFT can be sheared or distorted by interactions with dislocations[174-177], which could result in the movement of the apex atoms of SFT to new positions[174] and thus produce ledges on SFT[177]. The migration of these ledges by the absorption of vacancies or atoms can cause the growth or shrinkage of the vacancy-originated SFT[181,188]. Similarly, the gliding dislocation upon interaction with the dislocation-originated SFT can produce ledges on the side of SFT for a single dislocation-SFT interaction event (Figure 4.4h). As a result, the SFT can effectively migrate via simultaneous interaction events with multiple dislocations. Moreover, the relatively large surface-to-volume ratio in nanocrystals, as opposed to their bulk counterparts, could promote the SFT migration by feeding more SFs from the fertile surface nucleation sites. Additionally, it should be noted that the movement of SFT is distinct from the climb or glide process of dislocation under mechanical loading. The dislocations can climb or glide by themselves under external loading, whereas the SFT cannot move by itself and its migration must be driven by the dislocations through dislocation-SFT interactions.

4.3.3 Annihilation of dislocation-originated SFT

The annihilation of dislocation-originated SFT is also observed by our *in-situ* experiment (Figure 4.6 and Figure 4.7a,c). The pristine Au nanocrystal in Figure 4.6 is created by cold welding between two Au nanostructures[151]. Interestingly, SFT_1 is observed in the pristine Au nanocrystal right after cold welding (Figure 4.6a), which indicates the occurrence of plastic deformation during the cold welding process. Generally, when two nanostructures come into contact, a large mechanical stress could be induced at the contact zone, owing to the mismatch of geometry and orientation, which can result in the so-called dislocation-mediated pseudoelastic deformation if the contact surface is atomically flat[189]. In our experiment, however, the surfaces of the two nanostructures are not atomically flat (Figure 4.6a), resulting in the residual dislocations or SFT after contact. Moreover, due to the relatively low strain rate of cold welding and the large image stress associated with a small sample size, supersaturation of vacancies is unlikely in the cold-welding process and hence SFT_1 should be of the dislocation-originated type.

Upon mechanical loading, a new SFT (SFT_2) is produced near SFT_1 (Figure 4.6b). However, further deformation leads to the annihilation of SFT_2 and nucleation of SFT_3 (Figure 4.6c). Since the SFT_2 disappears fast (in less than 0.5s), the details of annihilation are not captured during *in-situ* experiment. However, the SF trace left indicates that the annihilation of SFT is mediated by dislocation-SFT interactions (Figure 4.7a,c). MD simulations (Figure 4.6d-h) further prove that the annihilation of dislocation-originated SFT is indeed a dislocation-mediated process, which is similar to that found for the vacancy-originated SFT in the bulk[170-176]. Figure 4d shows a closed dislocation-originated SFT near a TB inside the nanowire. Under tensile loading, a partial dislocation loop enclosing SF_1 nucleates on (111) plane and makes an edge-on

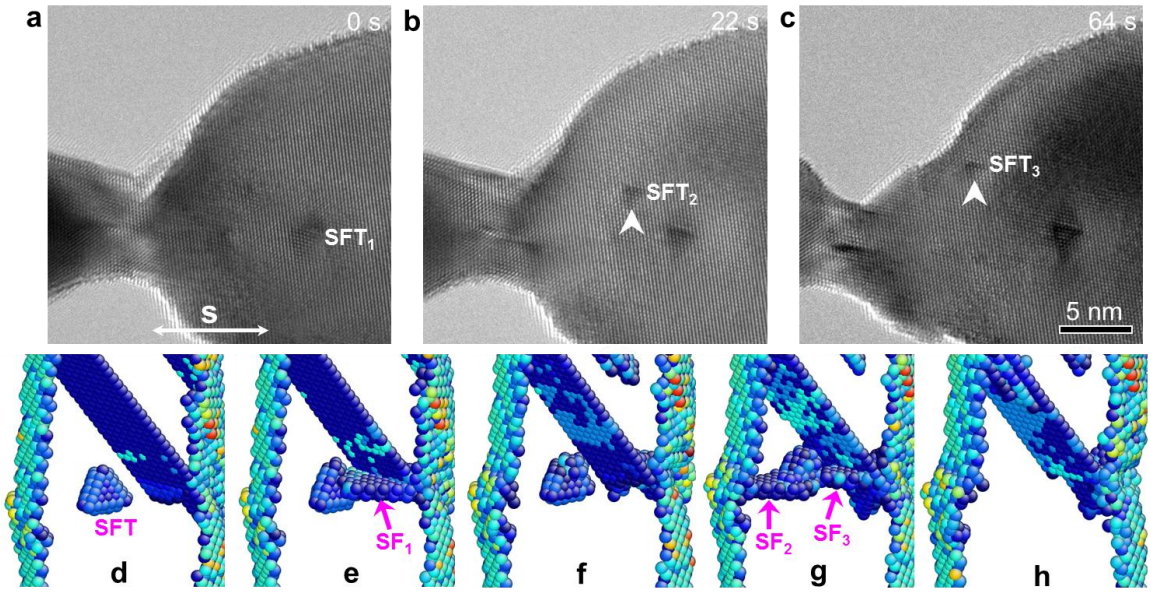

Figure 4.6 Annihilation of dislocation-originated SFT under tensile deformation. (a) SFT_1 is observed in the pristine nanocrystal after cold welding. (b) Upon tensile loading, SFT_2 is produced near SFT_1. (c) Further deformation induced the annihilation of SFT_2 and nucleation of SFT_3. (d-h) MD snapshots showing the annihilation of a dislocation-originated SFT by dislocation-SFT interactions.[184]

interaction with the SFT at the third atomic layer of the SFT from its apex. The closed-SFT is sheared and distorted (Figure 4.6e-f). This event is followed by similar events of newly nucleated partial dislocations shearing the closed-SFT (Figure 4.6g-h). The Shockley partial dislocation with the trailing SF_2 nucleates and interacts with the 1/6<110>-type sessile stair-rod dislocations constituting the basal plane of the SFT. These processes lead to the formation of new 1/6<112>-type Shockley partials which would be expected to glide on the tetrahedral planes of the SFT and partially remove the SFs, as has been reported for the SFT using MD simulations[174]. But what we observe for the SFT in the nano-sized sample is its complete destruction (Figure 4.6h) due to the SFs intersecting at its base and/or above (SF_2 and SF_3 in Figure 4.6g), instead of only a partial destruction as in the bulk samples[172,176]. Moreover, since the free surface in the sub-20 nm

nanocrystal serves as an efficient nucleation source of dislocations, it could thus play an important role in the annihilation of SFT by providing nucleated dislocations.

4.4 DISCUSSION

SFT have usually been classified as a vacancy-originated volume defect in quenched or irradiated metals and alloys[59,160-163]. However, it is unlikely that the SFT observed in the Au nanocrystals of this work are vacancy-originated. Firstly, a high density of vacancies is required to nucleate the vacancy-originated SFT, which is often present in quenched or irradiated metals[59,160-162] but is hardly achievable in our nano-sized metallic samples. Secondly, there are two possible factors regarding the electron beam effect, i.e., knock-on displacement and beam heating. For the knock-on displacement to occur, the threshold electron energy for Au is 1320 KeV[190]. The 300 KV acceleration voltage used in our experiments is therefore insufficient to produce such kind of beam damage[53]. For the beam heating issue, the thermal conductivity of Au is very high (300 W/mK) and the two ends of Au nanowires are respectively connected to an Au substrate and an Au probe with large sizes compared with the samples. Considering the low beam current applied in our experiments (80~100 A cm^{-2}) and the fact that both the Au substrate and the probe act as the effective heat sinks, the temperature rise induced by beam heating should be negligible in the sample[53,191]. More importantly, SFT are also observed to form during the deformation without any beam irradiation and beam-induced temperature rise (Figure 4.8), which further supports the conclusion that the SFT observed during plastic deformation is dislocation-originated and not vacancy-originated. Therefore, the beam irradiation and heating would have little influence on the SFT formation and dislocation-SFT interactions. Additionally,

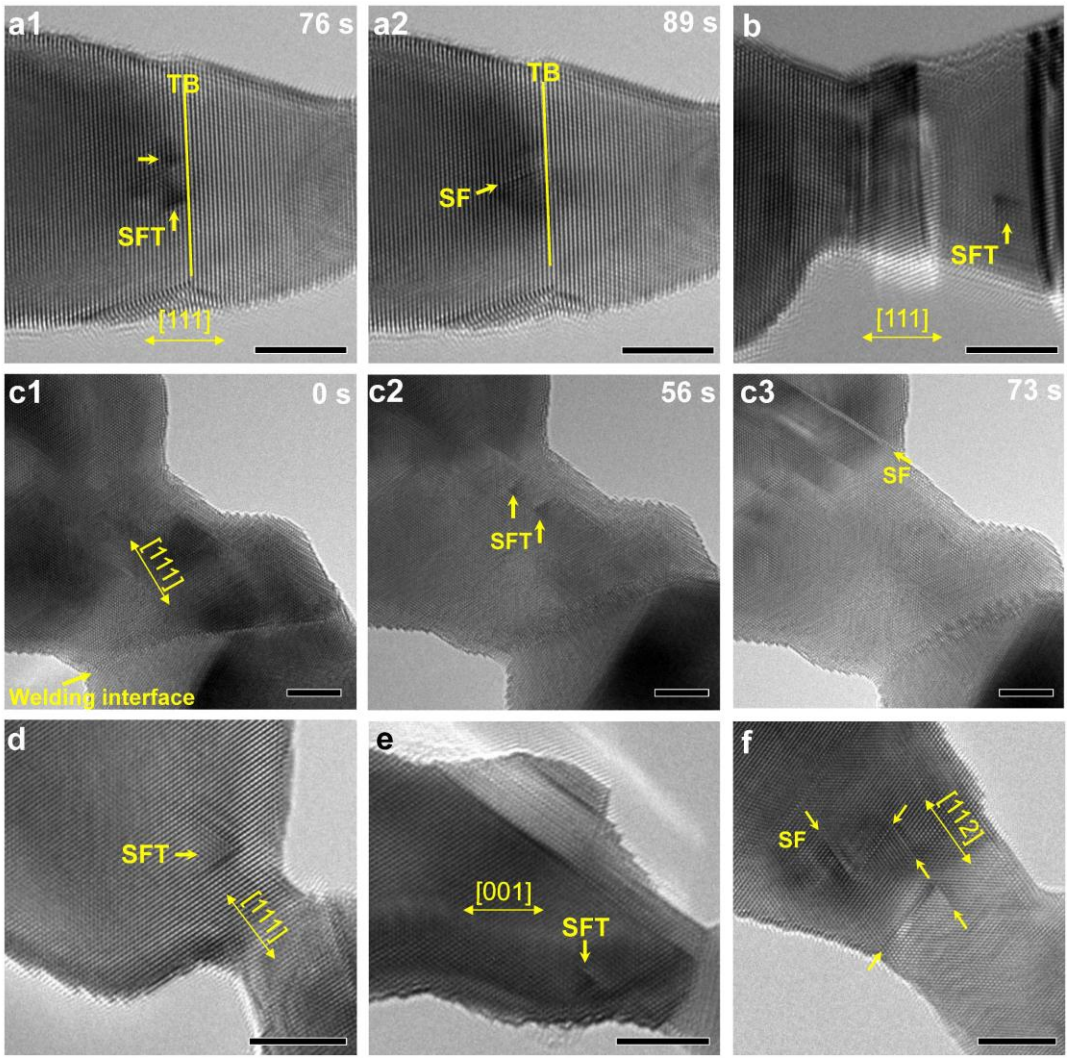

Figure 4.7 Additional examples of dislocation-originated SFT and dislocation interactions observed in different samples under tensile loading. The sizes of samples range in between 10~30 nm and they were loaded along different directions (e.g., [111], [001], [112]). (a) Annihilation of dislocation-originated SFT in Au nanowire. Under [111] tensile loading, the dislocation-originated SFT are formed near a TB. Further deformation induces the annihilation of SFT. The SF left in (a2) indicates that the SFT annihilation process is mediated by the dislocation-SFT interactions. (b) A dislocation-originated SFT formed during the necking process of a nanotwinned Au nanowire. (c) Generation and annihilation of dislocation-originated SFT in a sample made by cold-welding. The sample is loaded along the [111] direction. A welding interface was created in the sample due to the mismatch of geometry and orientation, as marked by the yellow arrow in (c1). (d) A dislocation-originated SFT formed in another [111]-loaded sample made by cold-welding. (e) A dislocation-originated SFT observed in a [001]-loaded sample made by cold-welding. (f) Dislocation interactions in an Au nanowire under the [112] loading. Scale bar in (a-f), 5 nm.[184]

although vacancy clusters and vacancy-originated SFT can be generated by plastic deformation, high strain rates are usually required[167,168]. In our experiments, the strain rate employed is relatively low and thus cannot produce sufficient vacancies by plastic deformation alone. Even if a smaller number of deformation-induced vacancies may exist, they could easily escape the nanocrystal from its free surface, owing to the large image stress associated with the small crystal size and the low strain rate employed, rather than condense into vacancy clusters inside the Au nanocrystal. Therefore, the observed SFT likely result from the interactions of partial dislocations, and our large scale MD simulations lend a direct support to this mechanism. On the basis of these considerations, we believe that the formation, migration and annihilation of the dislocation-originated SFT are revealed for the first time in sub-20 nm nanocrystals.

It is generally recognized that the surface-nucleated dislocations initiate the plastic deformation in nano-sized crystals[10,43,53]. The partial dislocations nucleated on the equivalent, inclined {111} planes can strongly interact with each other inside the small volume of Au nanocrystals, which results in the stair-rod dislocations and nano-sized dislocation-originated SFT. The dislocation-originated SFT have been frequently observed during the deformation of Au nanocrystals with different sample sizes and loading conditions in both experiments and MD simulations (Figure 4.7, 4.8 and Table 4.1). Hence, the formation and evolution of SFT should be considered as an important deformation mechanism at this length scale. Moreover, both SFT formation and dislocation-SFT interaction can contribute to the strain hardening of small-volume samples. Nanocrystals are known to have limited strain hardening due to the lack of sufficient hardening obstacles (dislocations or other defects) as well as the easy annihilation of dislocations at the surface owing to the large image stress[10,53,76]. In contrast, the formation of dislocation-originated SFT is a novel mechanism, by which the nanocrystal could achieve finite amounts of

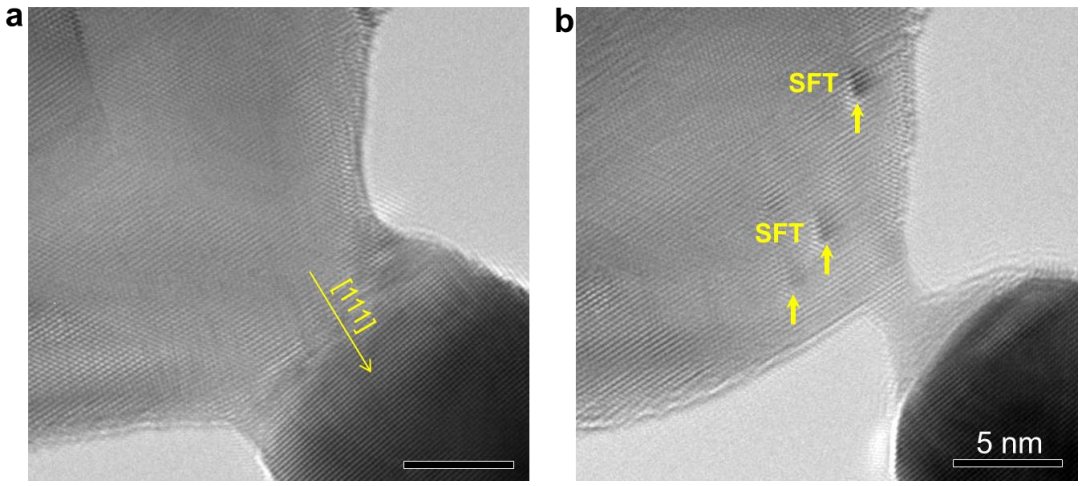

Figure 4.8 SFT observed in tensile experiment conducted under beam-blank. (a) Pristine sample. (b) Sample after beam-blank deformation. The sample is loaded along the [111] direction. SFT are observed to be formed during deformation without any beam irradiation and beam-induced temperature rise.[184]

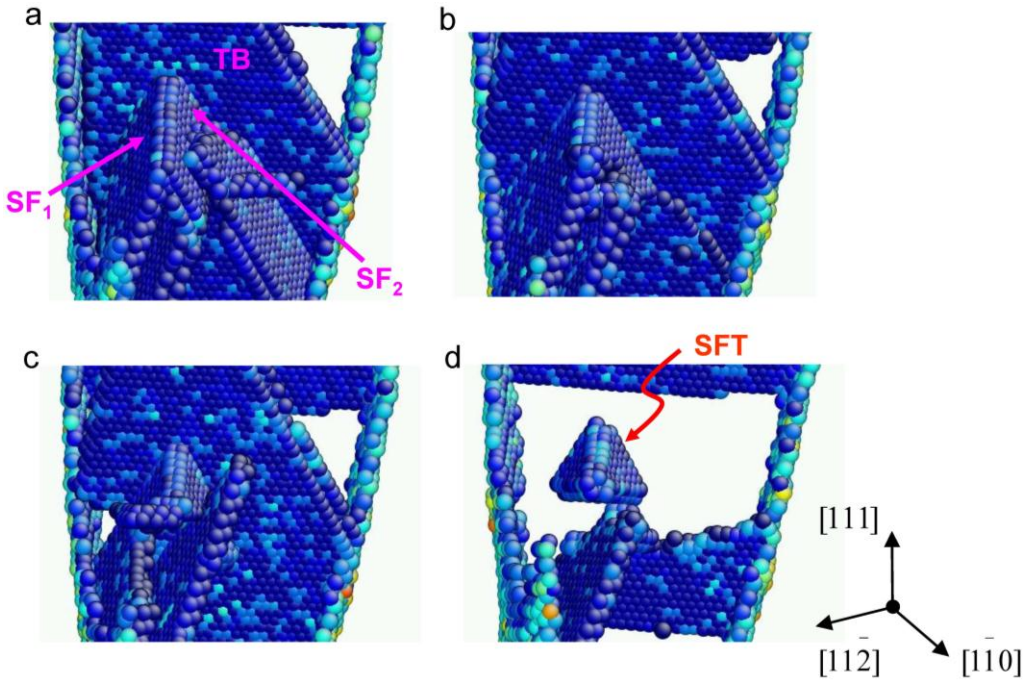

Figure 4.9 Formation of SFT in MD simulation of a deformed Cu nanowire through the same mechanism explained in Figure 4.2. The simulation methodology and the shape and the dimensions of Cu nanowires are similar to those for Au nanowires. It is observed that SFT were formed in the Cu nanowire, following the sequence of dislocation interactions, as in Au nanowires. The initial open-SFT is formed by the locking of the partial dislocations as can be seen in (a). As in Fig. 2(b-c) only two of the three SFs constituting the open-SFT are seen in this viewing angle. Trailing partials nucleate and sweep out a part of SF_1 and SF_2 in (b) and (c), respectively. Subsequent cross-slip of the trailing partial occurs to form the fourth (basal) face and the complete SFT is formed as shown in (d).[184]

Table 4.1 Summary of the SFT formation in 11 samples of Au nanocrystals tested in this work.[184]

Samples	Orientation	Samples tested	With SFT	Without SFT
Pristine nanowire	[111]	5	4	1 (dislocation interaction)
Cold-welded nanowire	[111]	4 (One beam-blank experiment)	4	0
	[001]	1	1	0
	[112]	1	0	1 (dislocation interaction)

inherent hardening. In addition, SFT act as strong obstacles to the motion of other dislocations (as shown in Figure 4.4) and contribute to further hardening. Furthermore, present results indicate that the SFT formation is not limited to the specific set of dimensions of the simulated nanowire, and the size of SFT formed depends on the sample size. Dislocation-originated SFT are also formed in a deformed Cu nanowire following the same dislocation-mediated mechanism as in the Au nanowires (Figure 4.9)[184]. This result indicates that the dislocation-originated formation of SFT is a general deformation mechanism applicable to a broad class of FCC metals and alloys with medium to low stacking fault energies under mechanical loading. On the basis of the above discussions, it can be concluded that SFT formation is a general plastic deformation mechanism in metallic nanocrystals, and has important consequences with respect to plastic deformation at small length scales.

The deformation-induced formation of 3D defects has never been reported for nanocrystals. In the conventional bulk samples, SFT form mostly due to irradiation or quenching alone[160,161], while in the nanocrystals SFT can form directly from dislocation interactions. Moreover, the dislocation-SFT interaction is known to cause the SFT to be sheared into two defects, converted to other types of defects or structurally destroyed[170,175-178]. However, our work

also reveals that the SFT can interact with a group of dislocations nucleated from the surface, resulting in the migration of SFT in a small and confined volume without any change in its shape and size. Such migration (i.e., displacive movement) of SFT can be attributed to the active operation of surface dislocation sources that is promoted by the high stress, large image force and abundant surface nucleation sites associated with the small crystal size, while it would be rare to achieve these conditions necessary for the SFT migration in the bulk. These unusual phenomena represent the novel deformation mechanisms at the nanoscale, and their potential effects on the strength, hardening and fracture warrant further study in the future.

4.5 CONCLUSIONS

In conclusion, *in-situ* HRTEM experiments were conducted to directly visualize the atomic-scale, dynamic evolution of a novel defect structure − dislocation-originated SFT − in Au nanocrystals. For the first time, we report the formation and the dynamics of a 3D crystalline defect in small-volume nanocrystals, which plays an important role in the plasticity at small length scales. These results reveal a novel deformation mechanism of dislocation interaction inside the confined volume of nanocrystals. This result has significant implications on understanding the deformation behavior of nanocrystals, including plastic yielding, strain hardening, ductility, size effects, *etc.*, which will motivate further experimental and modeling investigations of dislocation interactions and formation of higher-order defects in small-sized materials. On the other hand, it also provides an example of the deformation-induced and dislocation-originated formation mechanism of SFT in contrast to the conventional wisdom of vacancy-originated SFT, which

thus expands the fundamental knowledge of 3D volume defects in small-sized, non-irradiated materials. A more detailed understanding of various factors affecting the formation of SFT warrants further study in the future.

5.0 NEAR-IDEAL THEORETICAL STRENGTH IN GOLD NANOWIRES CONTAINING ANGSTROM-SCALE TWINS

Although nanoscale twinning are effective means to enhance the strength of metals[86], these metals generally prove to fail well below their theoretical strength due to heterogeneous dislocation nucleation from boundaries or surface imperfections[76]. Moreover, the twin size (λ) effect on the deformation and failure of nanosized single-crystals remains unexplored, especially at the minimum limit of twin size. Using in-situ tensile tests and atomistic modeling, the effects of angstrom-scale twins on the plasticity and fracture of Au nanowires have been studied. When the twin thickness is reduced to the smallest possible size of angstrom-scale (0.7 nm), Au nanowires exhibit a remarkable ductile-to-brittle transition that is governed by the heterogeneous-to-homogeneous dislocation nucleation transition, profoundly contrasting with the deformation behavior of metallic nanowires with twin-free or larger twins reported so far. Our quantitative measurements show that approaching such nanotwin size limit gives rise to an ultra-high tensile strength (up to 3.12 GPa) in Au nanowires, close to the ideal strength limit of perfect Au crystals. Such twin-size dependent dislocation nucleation and deformation represents a new type of size effect distinct from the sample size effect described previously. Those discoveries constitute an important step forward in understanding the angstrom-scale twins on the plasticity and fracture of metals, which are of fundamental and technological importance for future design and fabrication of ultra-strength materials.

5.1 INTRODUCTION

The device integration of Au nanowires hinges upon better understanding the ultra-high strength[19] and fracture behavior of individual nanowires under nanoscale deformation by direct measurements. As a model material, bulk Au is intrinsically the most ductile and malleable metal with a tensile ductility in the range of 0.2~0.4[73]. Past experimental studies showed that Au nanowires can be pulled with strain up to 50%[107], and long atom chains can be formed until the last atomic bond breaks[192]. Recent experiments and MD simulations also showed that sub-10nm-sized Au single crystals possess very good ductility before fracture[53,102]. However, it was also reported in another recent study that ultrathin Au nanowires can fail *via* brittle fracture with negligible ductility[56]. Brittle failure was attributed to deformation twinning[56] whereas this mechanism is recognized as promoting superplastic deformation in metallic nanowires[50,107,131]. In view of these conflicting observations, one question naturally arises: how to decisively control fracture in metallic nanowires?

The plastic deformation and fracture of bulk ultrafine-grained metals with grown-in nanoscale twins has been extensively studied since their first discovery 8 years ago[87]. It is now well-established that nanotwinned FCC metals have superior mechanical strength, remarkably-high ductility, and better tolerance to fatigue crack initiation with decreasing twin thickness (λ)[41,88,89]. Below a specific limit (λ < 15 nm), reducing λ dramatically enhances ductility due to softening effects attributed to heterogeneous nucleation and propagation of partial dislocations at the intersection of preexisting TBs with GBs[41,88,92,193]. Likewise, in FCC single-crystalline nanowires without GBs, heterogeneous nucleation of new partial dislocations from free surfaces is prominent[53,76,102]. Moreover, introducing low density twins (LDTs) to single-crystalline

nanowires can give rise to extensive strain-hardening and plastic flow after yielding owing to the blockage of partial slip by TBs[76,102]. However the maximum strength achieved in such materials is still considerably smaller than the ideal strength, which theoretically refers to the stress at elastic instability in a defect-free infinite crystal[76]. Furthermore, although ultrahigh density twins (UDTs) are frequently observed in metallic nanowires synthesized chemically[81-83], deformation and failure in nanowires with growth UDTs remain largely unexplored, specifically near the minimum limit of twin size (*i.e.* λ = 0.7 nm).

Here a series of *in-situ* tensile tests on Au nanowires with UDTs are conducted under TEM-AFM, as well as a detailed description of underlying mechanisms of deformation by HRTEM combined with MD computer simulations. It shows that UDTs provoke a ductile-to-brittle transition at a critical size (λ = 2.8 nm) controlled by homogeneous nucleation of dislocations inside the nanowires followed by shear localization and confined microplasticity at TBs. This new regime turns ultrathin Au nanowires into brittle-like materials with near-ideal strength, and is unlike the heterogeneous nucleation of partial slip from free surfaces that has commonly been reported for Au nanowires with no twins and LDTs.

5.2 EXPERIMENTAL PROCEDURES

Two types of experiment were conducted: nanomechanical testing and in situ HRTEM observation on the deformation. Experimental details were discussed in Chapter 3. In the nanomechanical testing, the spring constant (k) of the cantilever is 28 N/m. During deformation, a CCD camera was used to record the real-time images of sample elongation and the deflection

(Δd) of cantilever. The tensile loading force (F) was directly calculated by $F = k*\Delta d$. The engineering stress was calculated by using the formula $\sigma = 4F/\pi d^2$, where d is the minimum diameter of nanowire. The engineering strain was calculated by measuring the real-time length of the nanowires from TEM images. More than 20 samples were tested and about 40% were found to break with a brittle-like fracture. Au nanowires with LDTs and no twins were created inside the TEM by using the cold welding technique.

5.3 EXPERIMENTAL RESULTS

5.3.1 In-situ mechanical measurements in Au nanowires

Figure 5.1 presents the microstructure of ultra-twinned Au nanowires as synthesized in this study, along with mechanical properties of these materials under pure tensile loading. The growth direction of Au nanowires is along <111> (Figure 5.1a), with the diameter between 8 nm and 20 nm. Detailed TEM analysis reveals that parallel UDTs are perpendicular to the wire axis, and that the nanowire surface is made of {111} microfacets (Figure 5.1b). Figure 5.1c-d shows the two types of typical twin distributions in Au nanowires. The first type represents nanowires with UDTs, in which λ varies over a narrow range from 3 atomic layers ($\lambda = 0.7$ nm) to ~2 nm (Figure 5.1c). In the second type, the nanowires show a bimodal twin distribution with a mixture of UDT and LDT spacings (Figure 5.1d). The Au nanowires with different twin structures exhibiting distinct mechanical behavior.

Figure 5.2 shows that the mechanical response of Au nanowires with UDTs differs markedly from that of Au nanowires with LDTs and no twins. In the Au nanowires with no twin,

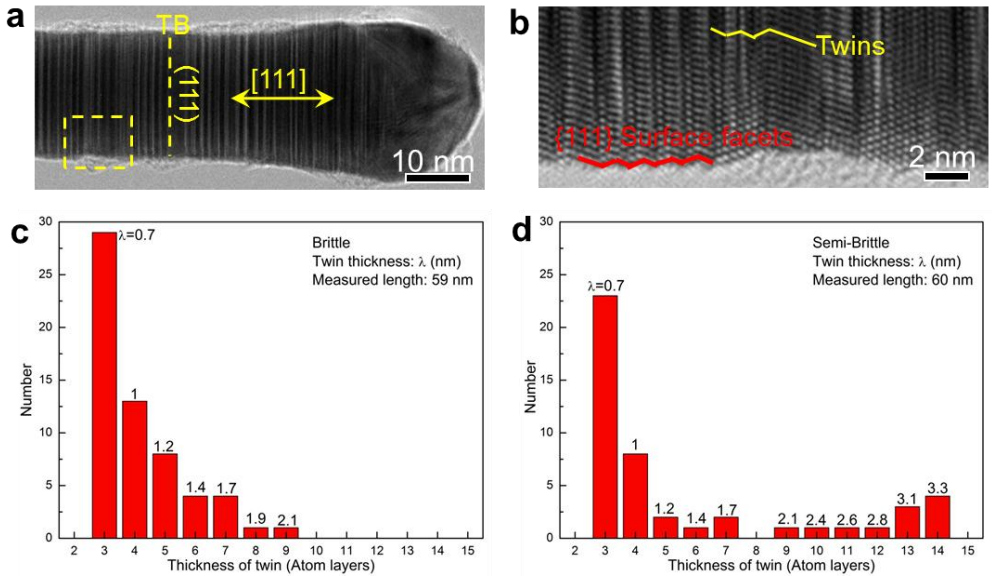

Figure 5.1 Microstructure of ultra-twinned Au nanowires. (a) Morphology of as-synthesized Au nanowire. (b) HRTEM image of the yellow-boxed area in (a) shows high density twins distributed along the nanowire axis ranging from 3 atomic layers (0.7 nm) to a few nanometers. {111} microfaceting can also be observed at the free surface. (c-d) Two types of twin distributions in ultra-twinned Au nanowires. (c) Nanowires with UDTs is made of twins less than 2.1 nm in thickness with a predominance of twins at the minimum limit of 0.7 nm and exhibited brittle-like fracture. (b) The nanowire with bimodal twin distribution showed a mixture twin spacing with UDTs and low density twins (LDTs).[10]

the ultimate strength was found equal to 1.43 GPa with no strain-hardening after yielding, in excellent agreement with past experimental measurements in pure single-crystalline Au nanowires[194]. This value is more than 30 times higher than the tensile strength of micrometer-thick polycrystalline Au films, which is typical due to plasticity size effects[195]. The mechanical response of Au nanowires with LDTs is characterized by significant strain-hardening with an ultimate strength of ~2.05 GPa after yielding (~1.7 GPa), as well as by a sizeable ductility (35%). Figure 5.2a shows that this behavior contrasts with that of Au nanowires with UDTs where strain-hardening is found to disappear, ductility is considerably reduced, and the elastic limit increases to ~3.12 GPa (Figure 5.2a-b), which is much higher than that of our Au nanowires with LDTs and no twins (Figure 5.2a-b) and single-crystalline Au nanocrystals reported in literatures

(Figure 5.2c)[42,68,73,107,194,196-199]. Remarkably, this limit corresponds to a critical resolved shear stress of 0.98 GPa for partial {111}<112> slip (Schmid factor = 0.314), which is very close to the ideal shear strength of 1.42 GPa for pure Au reported from past first-principle calculations[159]. Moreover, the fracture behavior of Au nanowires with UDTs is brittle-like with a flat fracture surface perpendicular to the loading axis (Figure 5.2d). Although the total elongation is about 7.2% due to the high elastic strain, plastic elongation at failure is negligible (less than 1%). More than 20 nanotwinned samples were tested and about 40% were found to break with a brittle-like fracture. In contrast, the behavior of nanowires with bimodal structure appears to be semi-brittle with slightly lower yield strength (~2.1 GPa) and limited, but finite inelastic deformation (~5%) and strain-hardening up to ~2.52 GPa (Figure 5.2a-b). For both brittle and semi-brittle fracture modes, no apparent plasticity is observed away from the fracture zone, but an interesting feature is that a tiny tip is formed on the failure surface in semi-brittle nanowires only (Figure 5.2e).

5.3.2 Homogeneous dislocation nucleation and deformation mechanisms

The above results enable us to conclude that a sharp transition from ductile plasticity to brittle fracture takes place in ultra-twinned Au nanowires with increasing twin density. The nature of the ductile-to-brittle transition is further examined by *in-situ* HRTEM and MD computer simulations. First, we consider the deformation and fracture of Au nanowires with LDTs and twin-free. Figure 5.3 confirm that the deformation of Au nanowires with LDTs and twin-free is dominated by dislocations nucleated from free surfaces[53,76,102]. In the Au nanowires with LDTs, uniform plastic elongation followed by necking primarily occurs between TBs with the largest λ. TBs are also found to act as barriers for partial dislocation motions (Figure 5.3b-c), thus leading

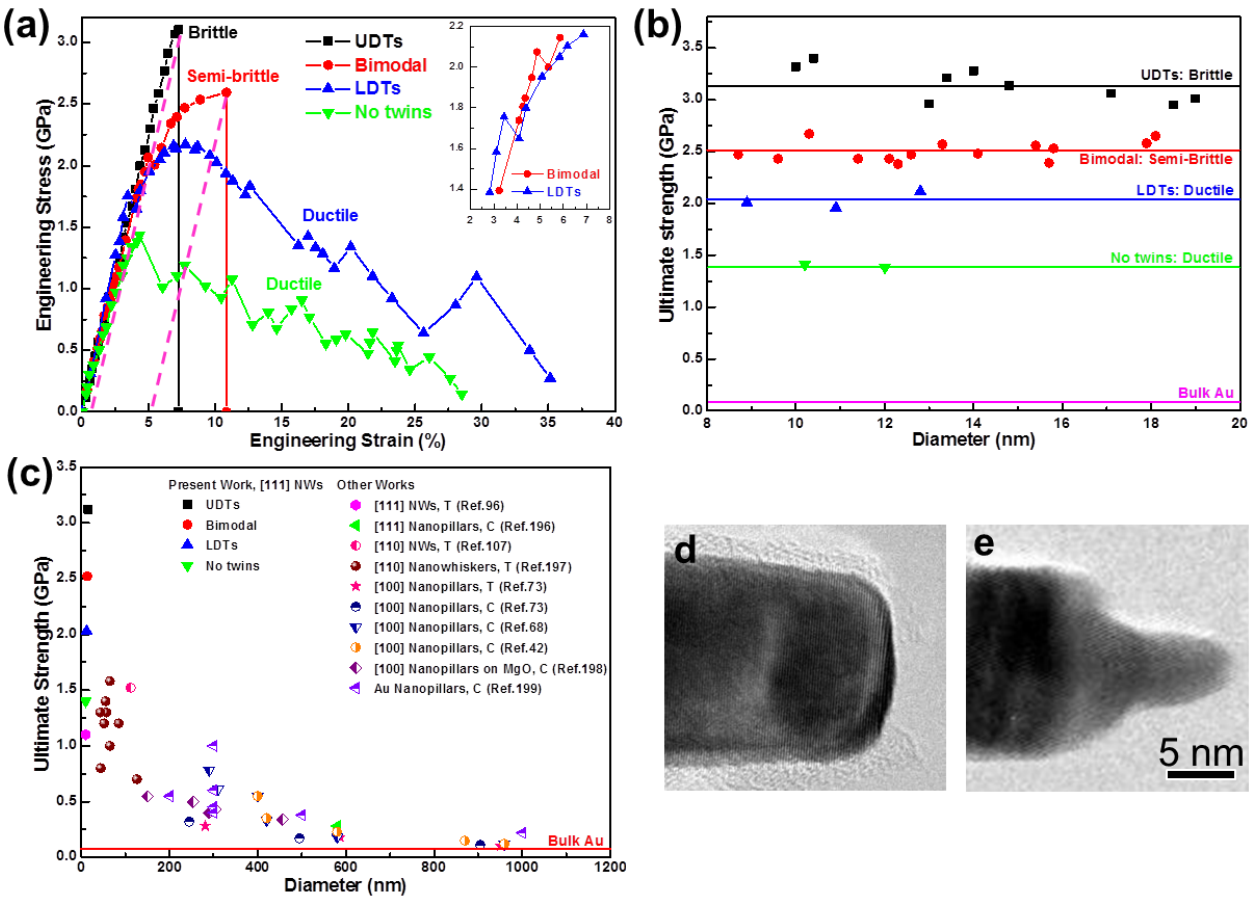

Figure 5.2 Mechanical properties and fracture modes of Au nanowires. (a) Representative stress-strain curves for Au nanowires with different structures. Dash lines in pink color indicate the permanent inelastic deformation after fracture. The diameter of samples with either UDTs or bimodal structures are almost identical, 14.5 nm and 13.4 nm respectively. The inset shows a close-up view of the yield points in the specimens with bimodal and LDTs. (b) Strength distribution in Au nanowires with different structure tested in this study. (c) Comparison of ultimate strengths in Au nanocrystals deformed by tension (T) or compression (C) experiments. The flow stress at 10% strain is used as the ultimate strength of compression tests on nanopillars. (d) Brittle-like fracture with a flat fracture surface observed in the sample with UDTs. (e) Semi-brittle fracture with a tiny tip in the fracture zone observed in the sample with bimodal twins.[10]

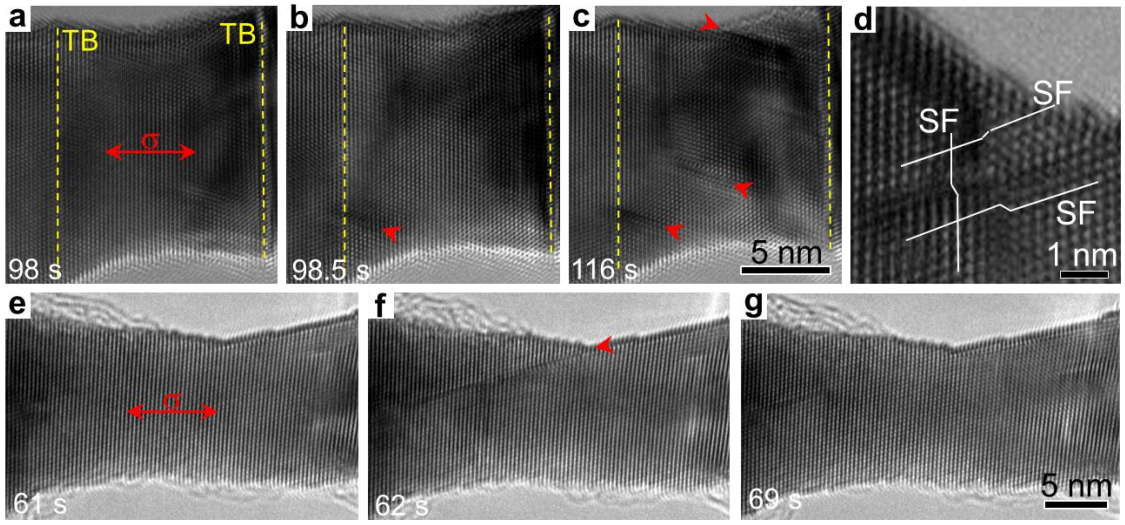

Figure 5.3 Heterogeneous dislocation nucleation in Au nanowires with LDTs (λ > 5.6 nm). (a) TEM image of an Au nanowire with LDTs. TBs are marked out by a dash line in yellow color. (b-c) During tensile loading, partial dislocations with SFs nucleate heterogeneously from the free surface, propagate and are blocked by the TBs, as marked out by the red arrows. (d) Interaction of surface dislocations on different {111} slip planes to form SF cross-structures from a different nanowire with λ ~ 10 nm. (e-f) The deformation of Au nanowire with no twins is dominated by the surface emission of partial dislocations, similar to the deformation of Au nanowires with LDTs.[10]

to the observed strengthening and strain-hardening effects[76,88,102]. Interestingly, the stacking faults nucleated on different {111} planes interact to form SF cross-structures (Figure 5.3d).

The fracture of a brittle-like nanowire with UDTs is displayed in Figure 5.4 for comparison. In this example, the twin thickness λ is less than 2.1 nm with a predominance of twins at the minimum limit of 0.7 nm (Figure 5.1c). Under tension, the nanowire first experiences considerable elastic elongation as evidenced by the space increase between TB_3 and TB_4 in Figure 5.4b, but sudden failure occurs at an applied strain of 6.8% (Figure 5.4c-e). The fracture process is materialized over such a short time scale that rare dislocation activity is observed, which is at odds with the larger slip deformation and high ductility observed in single-

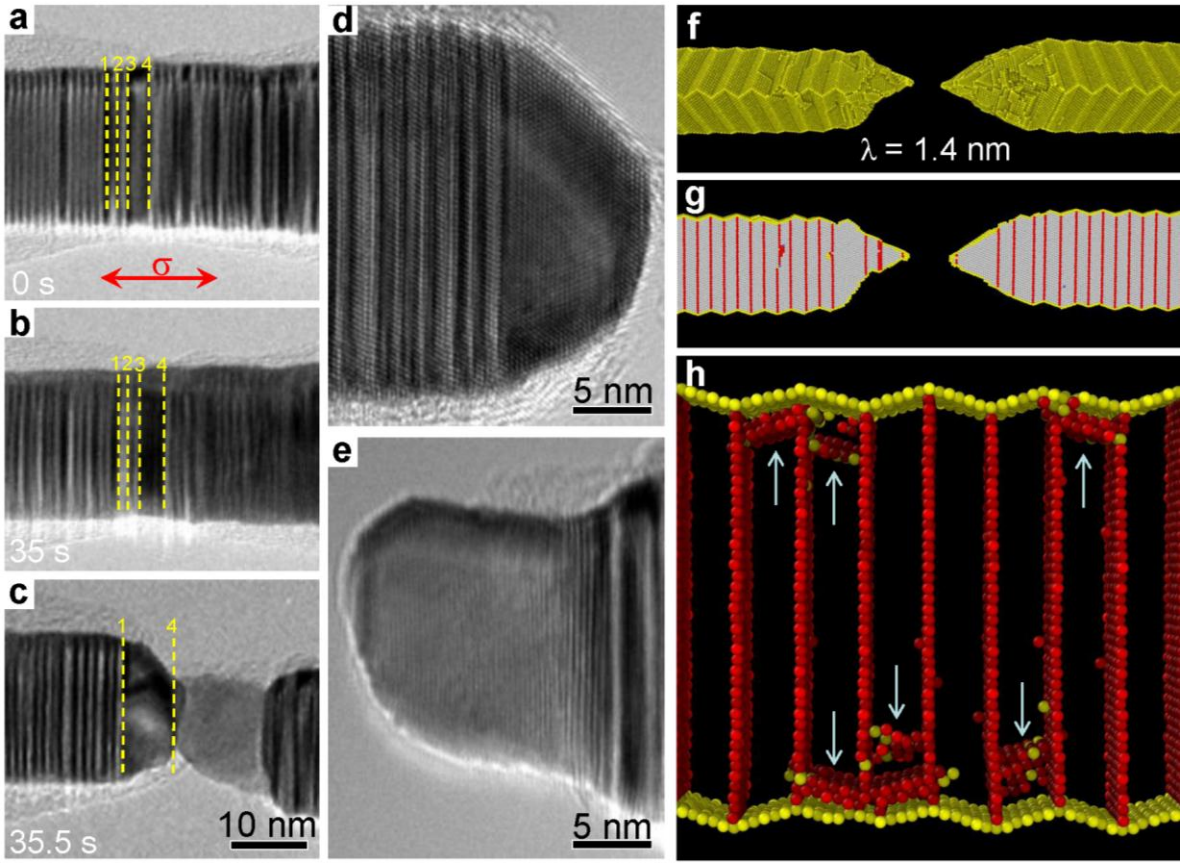

Figure 5.4 Tensile deformation and fracture in brittle-like Au nanowires with UDTs (λ < 2.8 nm). (a) TEM image of a pristine Au nanowire showing UDTs ranging from 0.7 to 2.1 nm, viewed in [110] zone axis. Twin interfaces of interest in the fracture zone are marked as TB_1 - TB_4. (b) Under tensile loading, the nanowire experiences elastic elongation as evidenced by the increase in spacing between TB_3 and TB_4. (c) At the elastic strain of 6.8%, the Au nanowire breaks suddenly with a relatively flat fracture surface, typically encountered in brittle fracture. (d-e) Post-deformation fracture morphology of Au nanowires at the two ends. A large de-twinned grain is found at both ends. (f) Full atomistic view and (g) cross-sectional view of Au nanowire with uniform twin distribution and λ = 1.4 nm after fracture at 5.5% tensile strain by MD simulation. (h) Close-up view of the fracture region at the onset of yielding showing the homogeneous nucleation of dislocations indicated by vertical arrows, near surface facets but inside the nanowire. Atoms in perfect FCC crystal arrangement have been omitted for clarity.[10]

crystalline twin-free Au nanowires[53,107] and Au nanowires with LDTs. However, the grains formed in the fractured tips (Figure 5.4d-e) indicate that significant slip and the de-twinning have occurred in the confined zone separating TB_1 and TB_4. This result is further supported by the MD simulations where a net reduction in ductility and shift to brittle-like fracture are manifest in nanowires with a {111}-microfaceted surface structure and $\lambda \leq 2.8$ nm (Figure 5.4f-h). Moreover, the simulated fracture is contained within a short nanowire segment exhibiting significant de-twinning (Figure 5.4f-g) as in the TEM experiments. A salient feature in MD simulations is that the onset of yielding in brittle-like nanowires proves to be controlled by homogeneous nucleation of dislocations between TBs (Figure 5.4h), as opposed to heterogeneous deformation from free surfaces (Figure 5.3).

We further examine the local shear strains computed at atomic-level from MD simulations to gain insight into the relationship between homogeneous nucleation, the de-twinning process, and brittle-like fracture. Here, particular focus is placed on an ultra-twinned Au nanowire with $\lambda = 1.4$ nm and a {111} microfaceted morphology (Figure 5.5). At the yield point, nucleation of dislocation loops on different slip planes is solely found inside the crystal (Figure 5.5a-b), and the nucleation sites are primarily adjacent to surface facets (see inset of Figure 5.5b), suggesting the homogeneous nucleation of dislocations. At this stage of deformation, the average shear strain at a nucleation site is equal to 0.136 ± 0.011, which agrees well with the ideal shear strain of 0.142 found theoretically by *ab-initio* simulations[159] for {111}<112> slip in Au. It can also be noticed that the yield strength of 5.5 GPa for <111> tension is generally higher than in experiments, which can be attributed to the strain rate effects inherent to MD simulations, the interatomic potential used, and the uncertainty in nanowire shape. However, it can be concluded that the yield strength of Au nanowires with UDTs rises up

to the ideal strength limit, thereby making the homogeneous dislocation nucleation the rate-limiting process controlling fracture.

Homogeneous nucleation is a nucleation mode of defect occurred inside the initially perfect crystal directly[200,201], which is triggered by the strain localization-induced local plastic displacement under the deformation loading[202]. Although the higher activation energy is required for the homogeneous dislocation nucleation than that of the heterogeneous nucleation from surface site, it could alleviate the plastic strain and storage energy in deformed materials due to their zero net elastic dilatation and short-range stress field[203], and thus it can occur in perfect FCC crystals subjected to nano-indentation[204], shock loading[201] or serve plastic deformation[205], in which the local shear stress can achieve the idea shear stress of metals. As discussed later, we hypothesize that homogeneous nucleation in ultra-twinned Au nanowires is induced by a shear instability under the ideal shear strength limit favored by the UDTs.

Homogeneous dislocation nucleation is rapidly followed by shear localization and specimen necking, which are both accommodated by twin migration and de-twinning (Figure 5.5d). Here, de-twinning arises from the atomic ledges formed at neighboring TBs during homogeneous nucleation, and the shear localization when dislocations transmit through the TBs (Figure 5.5c-f). While de-twinning promotes softening[92] and can partly enhance ductile plasticity, shear localization and necking accelerate the state of instability, which may partly explain the occurrence of both de-twinned tips and limited elongation in ultra-twinned Au nanowires (Figure 5.5e-f). Figure 5.5c-d also suggests that the absence of work-hardening in nanowires with UDTs is related to the lack of dislocation blockage by TBs[102] and dislocation storage. As λ decreases to the minimum limit, the shear localization-induced necking becomes increasingly more important over de-twinning.

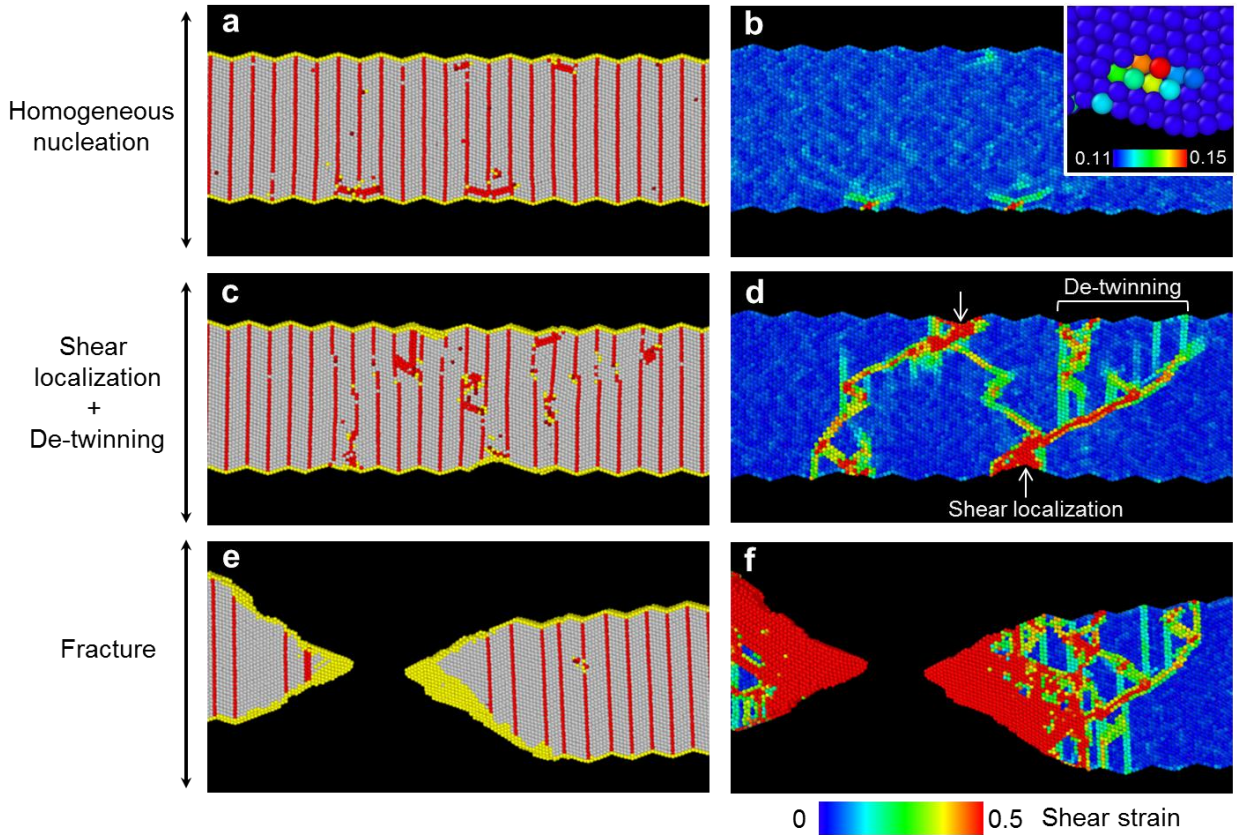

Figure 5.5 Simulated deformation structure and shear strain in a brittle-like Au nanowire over the yielding process. The Au nanowire contains UDTs with λ = 1.4 nm and {111} surface microfacets. (a-b) Homogenous nucleation, 5.2% strain. (c-d) Plastic shear localization and de-twinning, 5.6% tensile strain. (e-f) Fracture above 5.75% strain.[10]

5.3.3 Semi-brittle fracture in Au nanowires with bimodal twin structures

A striking aspect is the strong dependence of fracture on λ in ultra-twinned Au nanowires. Remarkably, ultra-twinned Au nanowires with bimodal twin structures show a compromise between strength due to homogeneous slip, and some microplasticity *via* de-twinning and strain-hardening, leading to the semi-brittle fracture (Figure 5.2c). Further TEM evidence is shown in Figure 5.6 where TBs of interest in the fracture zone are marked out in yellow color. It is noticed that λ is not uniform along the axial direction in this sample (Figure 5.6a), and follows a bimodal

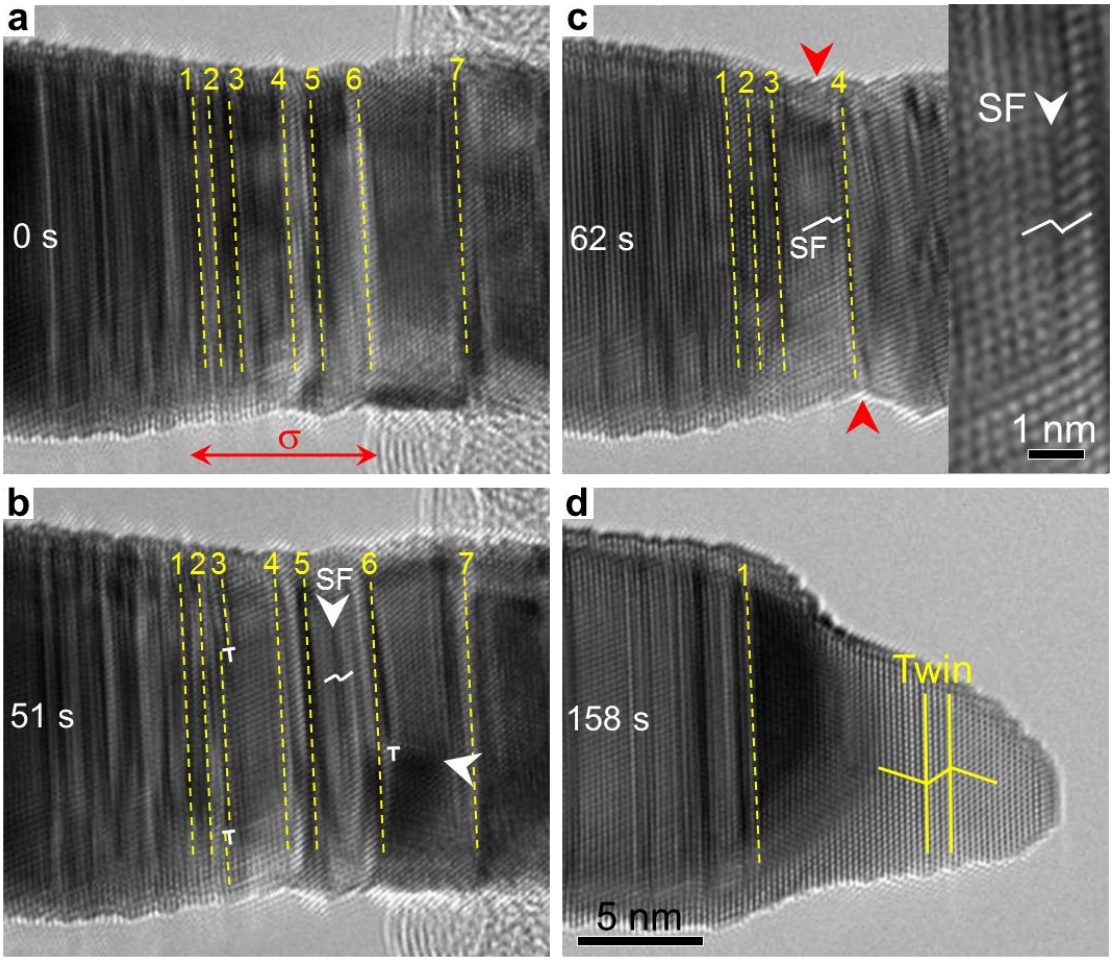

Figure 5.6 Deformation and fracture in a semi-brittle Au nanowires with bimodal twin structures. (a) Pristine Au nanowire with a bimodal twin structure as marked out by dash lines in yellow from TB_1 to TB_7. (b) As deformation proceeds, dislocations are observed to homogeneously nucleate in the segment with the largest twin thickness. The dislocations propagate and are blocked by the neighboring TBs, causing strain-hardening. (c) Shear localization-induced necking formation under tensile loading, as marked out by the red arrows. Inset: Close-up on a partial dislocation with SF propagating along the radial direction from the neck, which softens this region and accelerates failure. (d) Fracture morphology of semi-brittle fracture with de-twinned tips.[10]

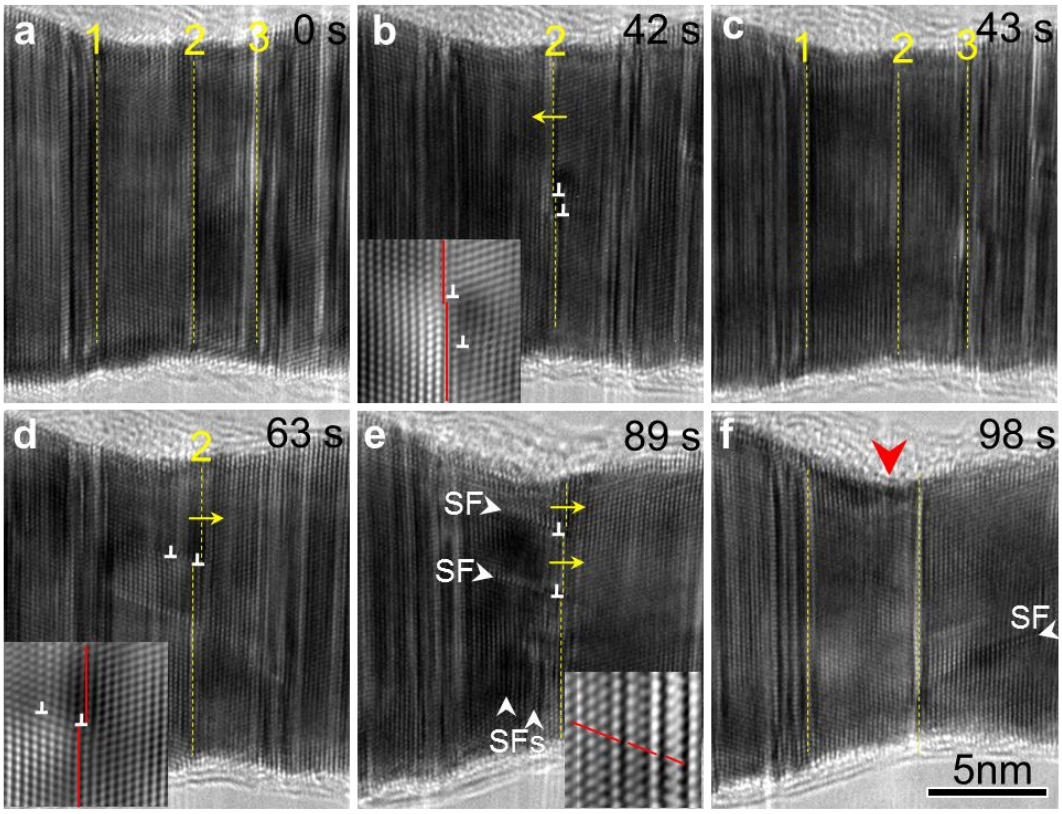

Figure 5.7 Sequential images showing the de-twinning and necking process in a semi-brittle Au nanowires with bimodal twin structures. (a) Pristine Au nanowire with bimodal twin structures. The deformation mainly occurs at the part with larger λ, as marked out by dash lines in yellow from TB_1 to TB_3. (b-d) Dislocations nucleate homogeneously in the part with larger λ, propagate and are blocked by the TB_2, which produce atomic ledges to TB_2 and finally induce the TB_2 migration. The inset in (b) and (d) are the inverse FFT images showing the dislocations blocked by TB_2. (e-f) The propagation of SFs parallel to the twin plane accompanied with necking formation. Inset shows the structure of SFs. The red arrow points out the localized necking.[10]

twin distribution (Figure 5.1d). In Figure 5.6b, plastic deformation starts in the region with the largest λ (between TB_3 and TB_7 with $\lambda \sim 2.4$ - 3.3 nm) in good agreement with past theoretical predictions[139]. As described above, dislocations and SFs are observed to nucleate directly inside the crystal (Figure 5.6b), i.e. homogeneous nucleation, which is consistent with the MD simulation; however several partial dislocations are blocked by TBs (TB_3 and TB_6 in Figure 5.6b), which likely contributes to the apparent strain-hardening of the bimodal sample (Figure 5.2c). Twinning partials produce some atomic-scale ledges on TBs and drive the moving TBs, causing de-twinning (shown in white reversed "T" at TB_3 in Figure 5.6b and TB_2 in Figure 5.7) are clearly visible because the Schmid factor for this type of slip is extremely low due to the TB orientation orthogonal to the axial direction of the nanowire. As deformation proceeds, shear localization promotes necking formation at the free surface (marked out with red-color arrows in Figure 5.6c and Figure 5.7f) after limited uniform plasticity. Propagation of SFs parallel to the twin plane accompanies necking (Figure 5.6c and Figure 5.7), and appears to soften the material in this region until failure. Also a tiny tip is visible in the fracture zone as a signature of post-yielding plasticity from de-twinning (Figure 5.6d).

5.3.4 Elastic strain limits in ultra-twinned Au nanowires

In perfect crystals without deformation, all atoms locate at their equilibrium lattice positions. However, under mechanical loading, the elastic strain will accumulate inside the crystal and induces the atoms deviating from their equilibrium positions, which will be reflected in the change of the inter-planar spacing[32,206]. At the elastic strain limit of crystals, the elastic strain accumulated in the crystal lattice will be partially released by the nucleation of lattice defects[53], leading to the yielding and the occurrence of permanent plastic deformation inside the crystals.

Therefore, the elastic strain limit for Au nanowires with different structures can be estimated by comparing the inter-planar spacing of the pristine state and the deformed state at the moment just before the nucleation of first lattice defects, *i.e.* yielding. Figure 5.8 shows the deformation of an [111]-Au nanowire with thinner irregular twins. Attentions will be paid to the thickness evolutions of two adjacent twins with the pristine values of 16.4 Å (T_1) and 40.1 Å (T_2), respectively (Figure 5.8a). It is observed that the thicknesses of T_1 and T_2 increase to 17.3 Å and 42.0 Å, respectively, before the yielding (Figure 5.8b). The maximum elastic strain experienced in T_1 and T_2 is ~ 5.5% and ~ 4.7% respectively, while the value obtained from the change of $d_{(111)}$ in T_1 is about ~ 5.1%, in consistent with each other. The above results suggest that the smaller the twin thickness, the higher the elastic strain limit.

Figure 5.9 summarizes the twin-size and crystal-size dependence of elastic strain limit in Au nanocrystals, including the values from present work and both experiments[53,73,107,197,207] and MD simulations[76] in the literature. Figure 5.9a shows that the elastic strain limits of Au nanowires are strongly twin-size dependent, in which all of the nanowires are loaded along [111] direction and have the similar diameter (10~20 nm). The elastic strain limits of [111]-Au nanowires can be effectively improved via nanoscale twins, as indicated by both the experiments and simulations[76]. As the twin size are reduced to angstrom-scale, the elastic strain limit rapidly approaches the ideal one of [111]-Au (Figure 5.9a). Figure 5.9b summarizes the maximum elastic strain in single-crystalline or nanotwinned Au nanowires with different crystal-sizes and loading geometries. It is obvious that the elastic strain limits (Open symbols in Figure 5.9b) of single-crystalline Au nanowires along different directions (e.g. [001], [110], [111]) keeps at a low level as the crystal size decreases to sub-10 nm, though improved when compared with the bulk one. However, a net improvement in the elastic strain limit can be achieved by introducing

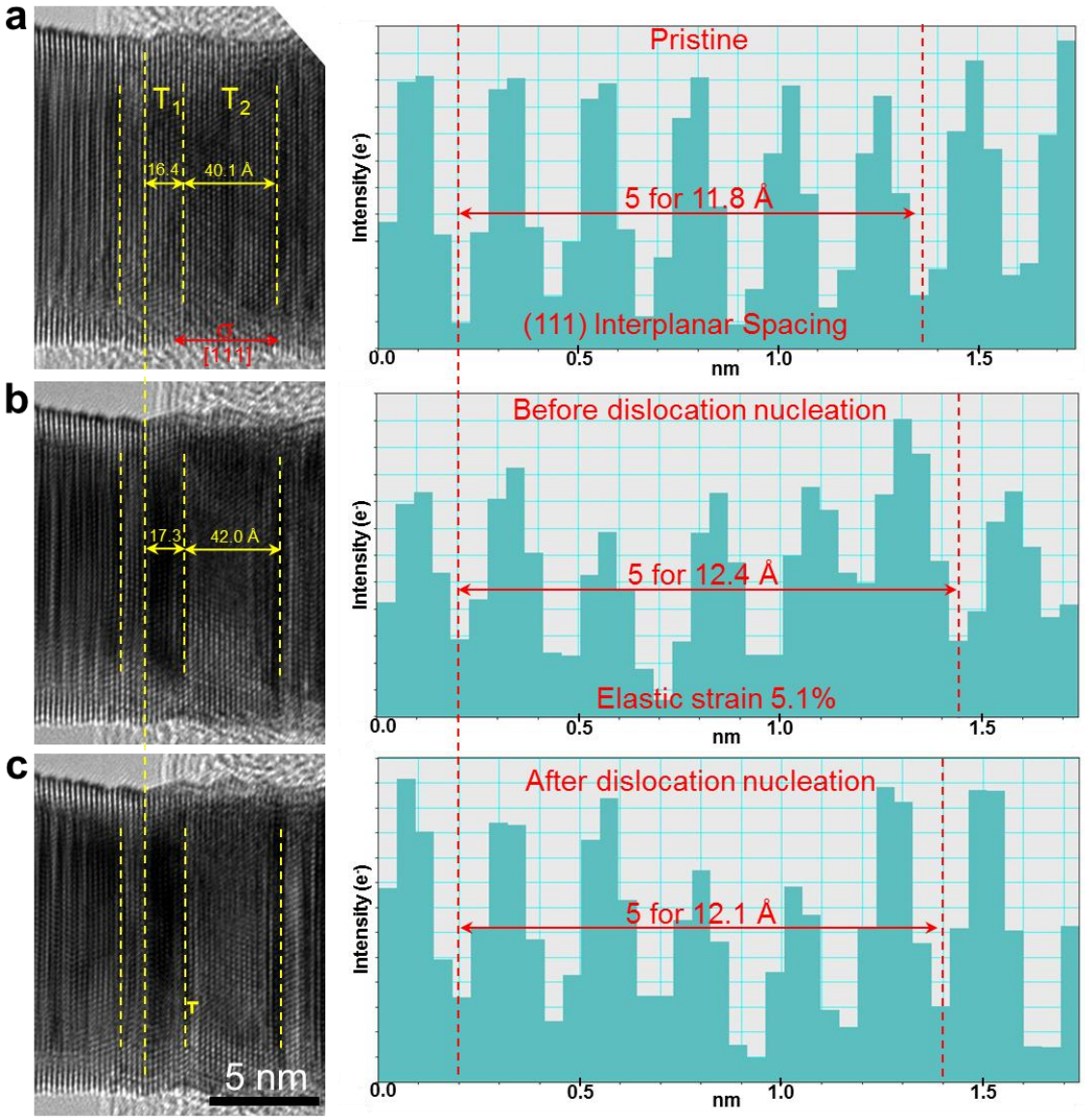

Figure 5.8 Twin thickness and interplanar spacing evolution of a nanotwinned [111]-Au nanowire with smaller λ during deformation. Two twins are marked out and labeled as T_1 and T_2, respectively. (a) Pristine nanowire. (b) Twin thickness and measured lattice spacing in Au nanowire before yielding. (c) Dislocation nucleates in T_2 with larger thickness firstly.

nanoscale twins, and near-ideal elastic strain limit can be approached when the crystal size and twin size are reduced simultaneously, as indicated by both [001] and [111] nanotwinned nanowires (Solid symbols in Figure 5.9b). It is also worth to note that the crystal-size dependence of elastic strain limit in Au is not so significant as that of Cu nanowires[206] in which the strong crystal-size dependence are observed. Structure modification, *i.e.* twins, is further needed to approach its ideal limit. Similar phenomenon may exist in other metallic or semiconductor nanowires systems, in which high density growth twins are frequently observed[10,12,79,81-84,97-100]. These findings shed some lights on the elastic strain engineering of metallic and semiconductor nanowires, in which the desirable physic-chemical properties can be obtained when they are elastically strained to the high strain-level[19].

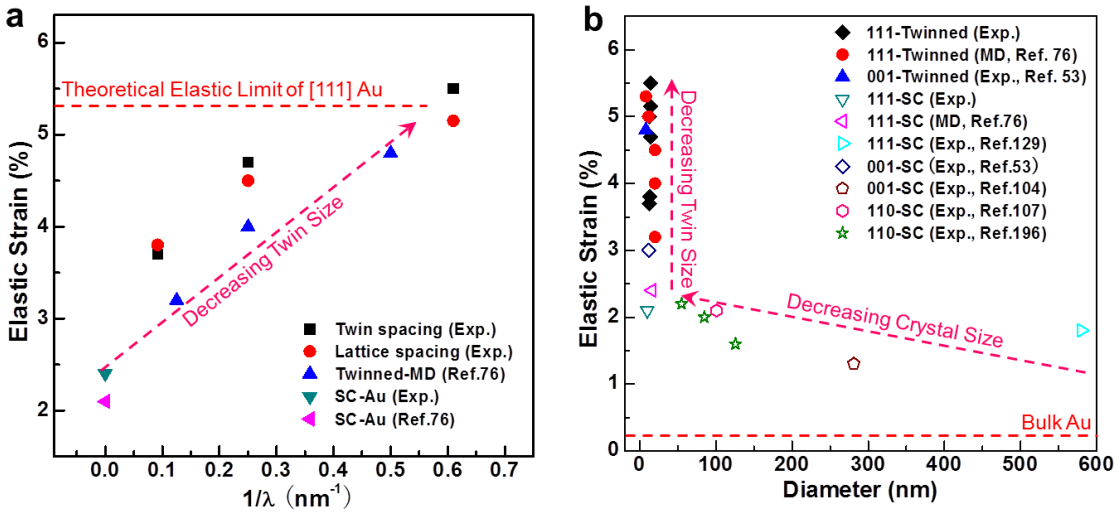

Figure 5.9 Effects of twin size and crystal size on the elastic strain limit in Au. (a) Twin size dependence of the elastic strain limit in [111]-Au nanowires. (b) Crystal size and twin size dependence of the elastic strain limit in Au nanowires with different orientations. The open symbols shows the elastic strain limits of single-crystalline Au nanowires, while the solid symbols shows the elastic strain limits of nanotwinned Au nanowires. "SC" in (a-b) means the data of single-crystalline Au nanowires; while "Exp." in (a-b) means that the values of elastic strain were obtained from experiments.

5.4 DISCUSSION

This study provides strong evidence for a heterogeneous-to-homogeneous dislocation nucleation in ultra-twinned Au nanowires below a critical twin size. In experiments, it was difficult to synthesize the nanotwinned with uniform twin distributions, and thus to reveal the critical twin size on the deformation mode transition. However, the stress-strain curves obtained by MD simulations reveal that a significantly ductile-to-brittle transition occurs when the twin thickness $\lambda \leq 2.8$ nm (Figure 5.10), accompanied with the heterogeneous-to-homogeneous transition in dislocation nucleation. Moreover, since significant slip activity was observed before failure, yielding in Au nanowires with UDTs should be viewed at the atomic scale as being different from classical brittle fracture by atomic cleavage[60]. With UDTs, slip is confined in such a way that the elastic strain energy cannot be easily released by means of dislocation propagation[53]. Instead, the homogeneous dislocation nucleation multiplies primarily near the low-index surface

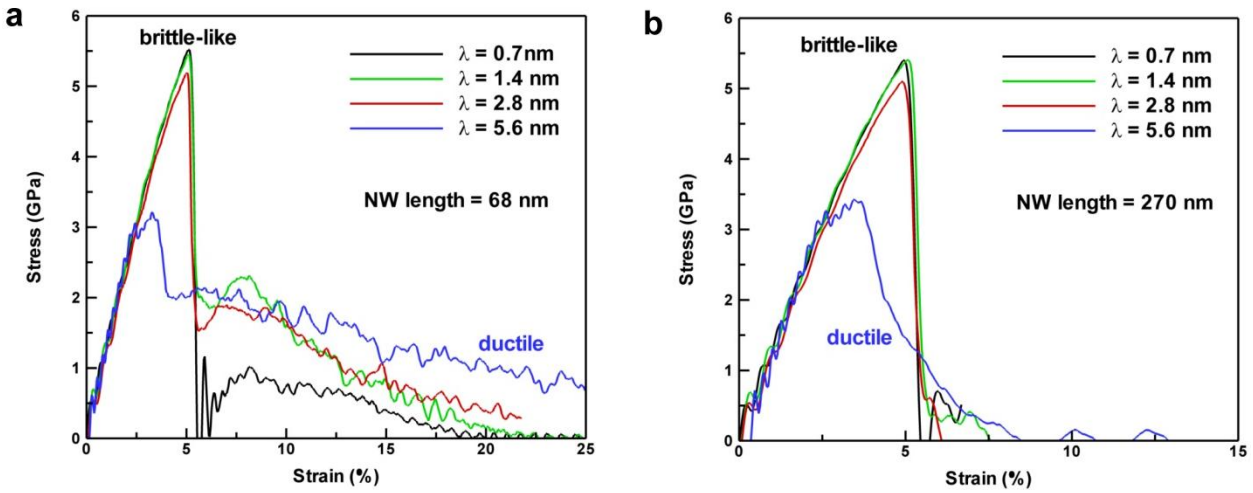

Figure 5.10 Stress-strain curves of ultra-twinned Au NWs computed from molecular dynamics (MD) simulations as a function of twin thickness (λ). All models have uniform twin distribution. The NW periodic length is 68 nm in (a) and 270 nm in (b).[10]

facets, such as {111} microfacets, causing an avalanche of new dislocations that accelerates shear localization and necking. Therefore, Au nanowires with bimodal twin structures show a composite behavior between ultimate strength and a few percent of ductility, within a relatively-narrow twin size distribution. In this case, the local increase in λ provides enough volume for dislocations to propagate and interact with neighboring TBs in other areas of the nanowire, thereby explaining the emergence of strain-hardening and ductility *via* de-twinning[76,102].

Surprisingly, the ductile-to-brittle transition promoted by the heterogeneous-to-homogeneous dislocation nucleation with increasing twin densities, is totally opposite to the change from brittle fracture to ductile plasticity reported so far in nanotwinned ultrafine-grained Cu materials[88], and recent experiments on single-crystalline Cu nanopillars and nanowires with ultrathin twins[83,208]. The ultrafine-grained Cu containing nanotwins exhibits increasing softening and ductility with decreasing λ[41,88], because deformation mediated by GBs are typically responsible for a transition from brittle fracture to extended ductility with decreasing λ[41]. Recent experiments on nanotwinned Cu nanopillars without GBs[208] have shown a brittle-to-ductile transition in samples loaded perpendicularly to TBs, as the TB spacing decreases below a critical value (~3 - 4 nm), in which the deformation was found to be dominated by the heterogeneous nucleation of dislocations from the intersections of TBs with the free surface. The brittle-to-ductile transition resulted from such heterogeneous nucleation of dislocations from the TBs/surface intersections, and shear band formation propagating across the samples[208].

This distinctive behavior can possibly be understood by considering three factors. First, the stacking-fault energy curve being different between metals[209], the stresses required to nucleate new dislocations from both heterogeneous and homogeneous nucleation is 2-3 times larger in Cu than Au[101]. However, the tensile strength previously measured in 50-nm

nanotwinned Cu nanopillars (1.35 GPa)[208] is twice as small as that of our ultra-twinned Au at a comparable twin size (λ = 1.4 nm), which is indicative that the deformation mechanisms in Cu nanopillars with ultrathin twins are not related to homogeneous dislocation nucleation like Au nanowires with UDTs. Second, the diameter of Au nanowires in this study is the smallest ever reported in the literature for metallic nanowires with UDTs. Past theoretical studies have shown that TBs exert a repulsive force on gliding dislocations due to image effects across the interface[106,139]. Such repulsive force increases linearly with $1/\lambda$, and the slope of this linear relationship was found to double with decreasing nanowire diameter from 25 nm to 8 nm[103,139]. Brittle-like fracture may therefore occur in ultra-twinned Au nanowires with $\lambda \leq 2.8$ nm because the theoretical strength limit is likely more rapidly attained than in larger nanowires. This assumption is also supported by the fact that only softening due to heterogeneous dislocation nucleation from the TB-surface intersection was found in larger Cu nanopillars with ultrathin twins[208]. Third, the ideal strength limit in a metal has been shown to be dictated by instabilities in the acoustic phonon spectra[80]. In semiconductor crystalline nanowires, phonon spectra and vibrational behavior can be markedly influenced by the type of surface facets, such as {111} microfacets[75]. Furthermore, past atomistic studies in circular metallic nanowires have shown that the TB-surface intersections may have the largest atom vibration and higher stress concentration[103,210]. In metallic nanowires, however, surface effects remain largely unexplored, primarily because characterizing the details of the surface structure at the atomic scale is extremely challenging experimentally. Nevertheless, the fact that ultra-twinned nanowires in Cu and Au have been synthesized by different methods suggests that these nanowires may have different surface structures and, therefore, different mechanical behavior with increasing twin density.

5.5 CONCLUSIONS

In conclusion, direct quantitative measurements on individual, ultrathin Au nanowires with UDTs by *in-situ* tensile testing are conducted inside a TEM. We found that Au nanowires containing angstrom-scaled twins (0.7 nm in thickness) exhibit tensile strengths up to 3.12 GPa, near the ideal limit, with a remarkable ductile-to-brittle transition with decreasing twin size, opposite to the behavior of metallic nanowires with lower-density twins reported so far. Ultrahigh-density twins (twin thickness < 2.8 nm) are shown to give rise to homogeneous dislocation nucleation and plastic shear localization, contrasting with the heterogeneous slip mechanism observed in single-crystalline or low-density-twinned nanowires. The twin-size dependent dislocation nucleation and deformation represent a new type of size effect distinct from the sample size effects described previously. These findings shed lights on a new regime of fracture in metallic nanowires, and its physical mechanism, which can be controlled by modulating twin densities and therefore represents a new type of size effect distinct from sample size effects described previously. Furthermore, the conclusions of this study demonstrate the possibility of fabricating gold nanostructures with a desirable combination of ultrahigh strength and some ductility through optimization of the twin structure, which is of technological importance for micro-devices subjected to extreme stresses.

6.0 IN SITU ATOMIC-SCALE OBSERVATION OF DEFORMATION TWINNING DOMINATED PLASTICITY IN TUNGSTEN NANOCRYSTALS

Twinning is a fundamental mode of plastic deformation that competes against dislocation slip in crystalline solids[86,110,112,211]. In metallic nanocrystals, plastic deformation requires higher stresses than needed in their bulk counterparts, known as "smaller is stronger"[19,37,212,213]. Such high stresses are thought to favor twinning over dislocation slip. Indeed, deformation twinning has been well-documented in FCC nanocrystals[107,112,130,197,214,215]. However, it remains unexplored in BCC metallic nanostructures. By using in situ high-resolution transmission electron microscopy and atomistic simulations, here it finds that twinning is the dominant mode of plastic deformation in BCC tungsten nanocrystals. Such deformation twinning is pseudoelastic[145,216,217], manifested as reversible detwinning during unloading. Moreover, the competition between twinning and dislocation slip can be mediated by loading orientation, an effect attributed to the defect growth controlled plasticity in BCC nanocrystals. This work directly reveals the deformation twinning phenomenon and provides crucial insight into plasticity mechanisms in BCC nanocrystals.

6.1 INTRODUCTION

The past decade has witnessed a dramatic increase in the study of mechanical properties and deformation mechanisms in metallic nanostructures[19,20,112,212]. Among those works, one prominent approach is to conduct the in situ mechanical testing of nanostructures[37,44,184,218]. These real-time experiments have revealed a wealth of novel deformation behaviors and size effects in small-volume nanocrystals, including dislocation starvation[68], mechanical annealing[44], surface dislocation nucleation controlled yielding[43,184], and transition from dislocation to twinning dominated plasticity[107,130,197], etc. However, the majority of those results are obtained for FCC nanocrystals. Given the widespread use of bulk BCC metals, BCC nanocrystals are expected to play significant roles in future nanotechnologies. Hence it is natural to ask to what degree those phenomena and size effects still hold in BCC nanocrystals.

One fundamental question on deforming nanocrystals is to twin or not to twin[214,215,219]. In bulk crystals, deformation twinning usually occurs under high strain rates or low temperatures[110,119]. In metallic nanostructures, plastic deformation requires higher stresses than needed in their bulk counterparts, owing to the starvation of plastic carriers in small crystal volumes with large surface areas. Such high stresses are thought to favor twinning even at room temperature and low strain rates, which can critically affect the strength and ductility of metallic nanocrystals[107,136]. Recently, both in situ and ex situ nanomechanical experiments have revealed the deformation twinning behaviors in FCC nanocrystals, including Au nanowhiskers[197] and Cu single crystalline nanowires[130]. In contrast, the mechanical testing of small-volume BCC crystals only reported the dislocation mediated plasticity, for example, in single crystalline W, Mo, Ta, Nb, V, Fe nanowires or nanopillars[220-222], Mo alloy nanofibers[70], and Mo nanopillars[134]. Other

mechanical testing of BCC micro- and nano-pillars without TEM analysis of pre- and post-existing dislocations also attributed plastic deformation to the dislocation-mediated processes[26,223]. The lack of observed deformation twinning in BCC nanocrystals is unexpected. In bulk BCC metals, ambient-temperature plasticity is usually controlled by screw dislocations that have high lattice resistance and low mobility[40,132,224,225]. In plastically deforming BCC nanocrystals, on one hand, the large surface area tends to destabilize dislocation sources, and on the other hand, the sluggish movement of screw dislocations can be insufficient to accommodate applied loads. As a result, twinning is expected to operate and even become a dominant deformation mechanism.

To understand the competition between dislocation slip and twinning in small scale BCC metals, here we investigate the deformation behavior of BCC tungsten (W) nanocrystals using in situ mechanical testing under high-resolution TEM (HRTEM). A unique in situ welding process to fabricate the BCC W nanowires has been developed. This method overcomes the difficulties in synthesizing the sub-100 nm and clean BCC samples without preexisting defects, in contrast to the commonly used sample preparation method by focused ion beam cutting that tends to create the feature size larger than ~100 nm and surface damages[44,68,134]. With in situ fabricated samples, it demonstrates that at room temperature and low strain rates, deformation twinning is the dominant mode of plastic deformation in W nanocrystals. Such mechanical twinning is shown to be pseudoelastic, since the twin band can be reversibly eliminated during unloading. It is also found find that the loading orientation can mediate the competition between twinning and dislocation slip. Atomistic simulations are performed to provide insights into the twinning dominated plasticity in BCC nanocrystals.

6.2 EXPERIMENTAL PROCEDURES

The single and bi-crystal W nanowires were fabricated directly inside TEM using in situ welding process discussed in Chapter 3.1.2. The bi-nanocrystals with a grain boundary were created due to the orientation difference between W probe and the nanotooth. Samples with different loading geometries, such as <110> and <112>, were created for the *in-situ* tension and compression experiments to study the orientation-dependent deformation. All the nanomechanical testing of W nanowires were conducted under room temperature and at the strain rate of 10^{-3} s^{-1}. For the observation of deformation twinning, the W nanowires were tilted into [110] zone axis, while [112] zone axis were used for the observation of dislocations. MD simulations were further conducted to reveal the mechanism of reversible deformation twinning and the loading orientation dependent plasticity in W nanowires. MD simulation method can be found in Appendix B.3.

6.3 EXPERIMENTAL RESULTS

6.3.1 Deformation twinning in W nanowires

Figure 6.1 shows the in situ observation of uniaxial compression of a nanoscale W bi-crystal at room temperature. The bi-crystal nanowire sample is prepared by the in situ welding of two nano-sized W single crystals. This sample contains a large single crystal whose $[\bar{1}10]$ direction is aligned with the overall axial direction of the bi-crystal nanowire. Hence, the applied axial load

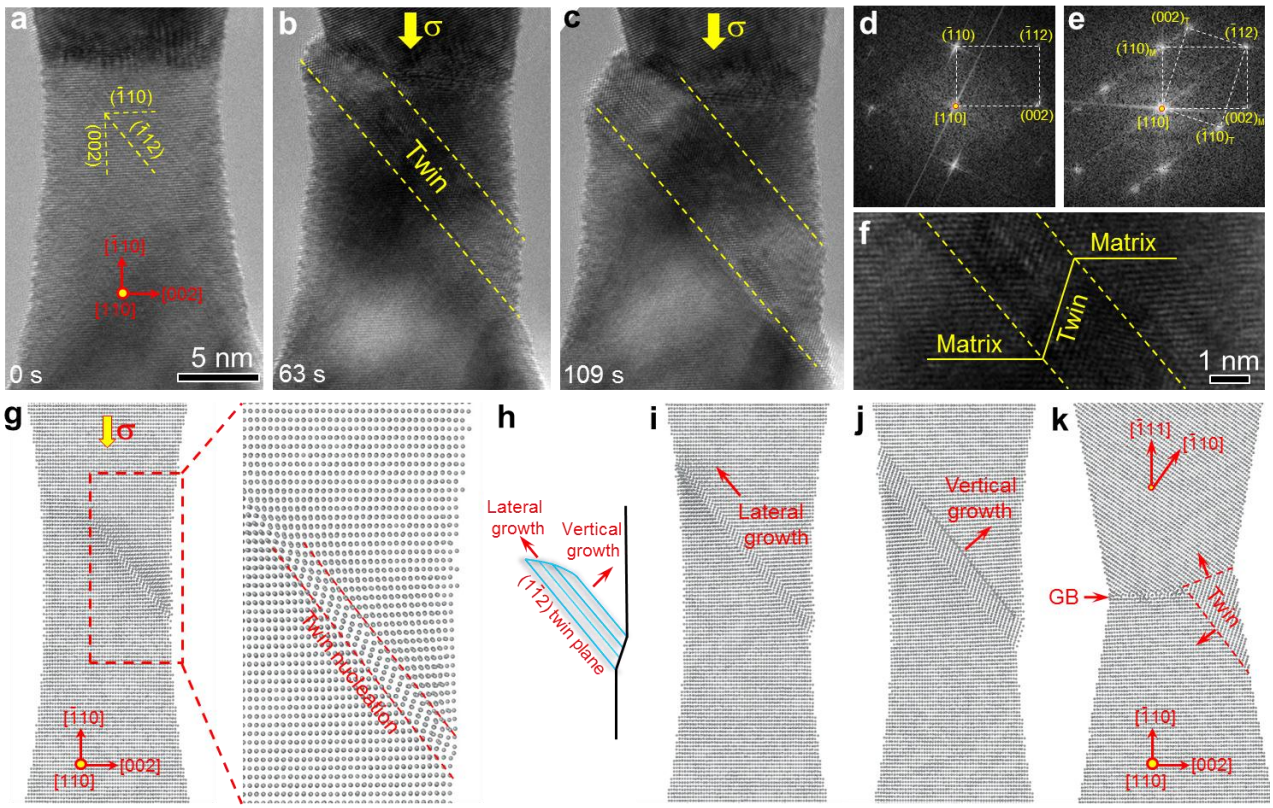

Figure 6.1 Deformation twinning in a W nanocrystal under $[\bar{1}10]$ compression. (a-c) Sequential images showing deformation twinning in a W nano bi-crystal (15 nm in diameter) at room temperature under a strain rate of 10^{-3} s^{-1}, which is loaded along $[\bar{1}10]$ and viewed along [110]. (d-e) The Fast-Fourier transformed (FFT) pattern of the pristine W nanocrystal and the deformation twin. (f) An enlarged image of the deformation twin. (g) A MD snapshot and zoom-in image showing the nucleation of a deformation twin embryo in a W single crystal nanowire. (h) Schematic of the lateral and vertical growth modes of a twin band. (i-j) MD snapshots showing the lateral and vertical twin growth. (k) The nucleation and growth of a deformation twin in a W bi-crystal nanowire. The crystal orientation is same as the orientation of Figure 6.3.

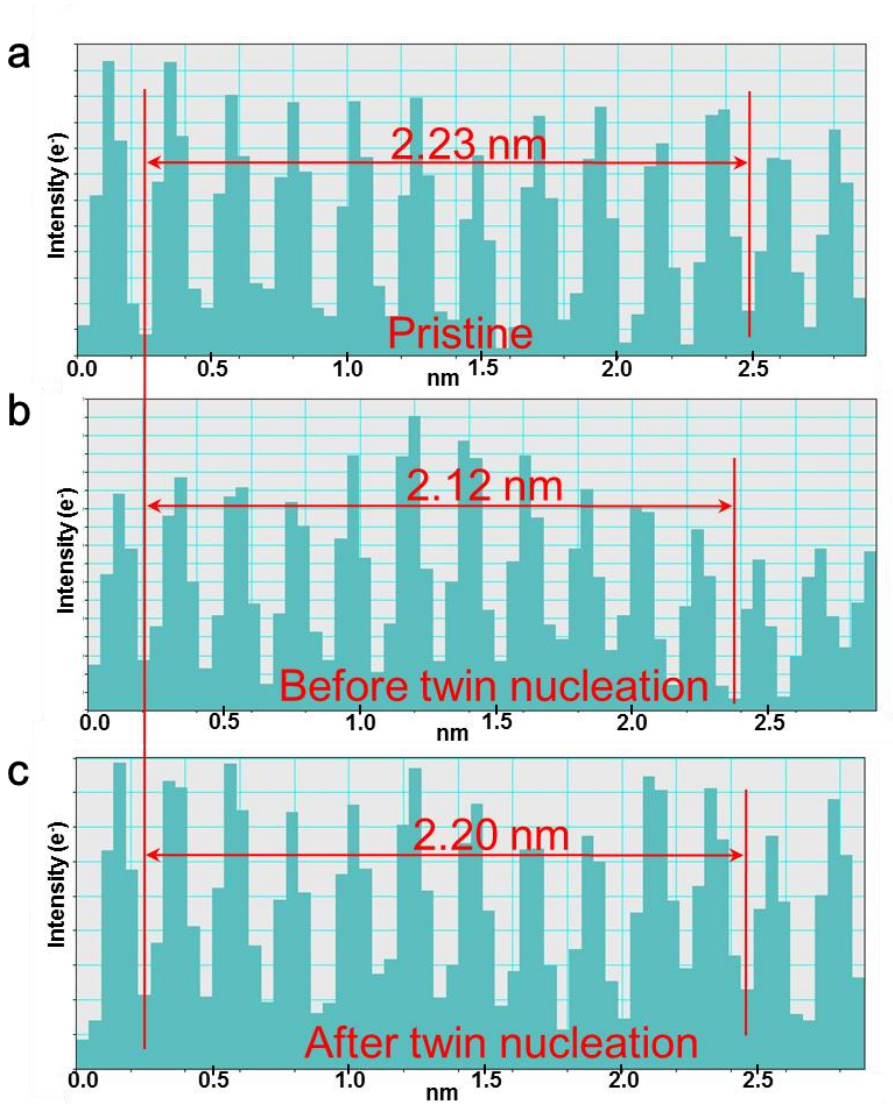

Figure 6.2 The inter-planar spacing evolution of the $(\bar{1}10)$ plane under compressive loading. The strain, and hence stress, of twin nucleation is estimated by measuring the inter-planar spacing of the $(\bar{1}10)$ planes. (a-b) The inter-planar spacing of the $(\bar{1}10)$ plane decreases gradually as the elastic compressive strain increases. At an elastic strain of 4.9 %, the W bi-nanocrystal yields suddenly via the emission of a deformation twin. The Young's modulus of W along ⟨110⟩ direction is 389 GPa (See Appendix A), thus the estimated yield strength is about 19.2 GPs. Considering that the deformation twin is formed via slip on the $[\bar{1}11](\bar{1}12)$ twin system and the Schmid factor is 0.47, the resolved shear stress for the twin nucleation is estimated to be 9 GPa. (c) After the nucleation of the deformation twin, the compressive strain is released to about 1.3%.

is effectively along the $[\bar{1}10]$ direction of the large single crystal. The viewing direction is along the transverse [110] direction (Figure 6.1a). Upon compressive loading, the large $[\bar{1}10]$ oriented W nanocrystal initially undergoes elastic deformation. As the lattice strain accumulates to ~ 4.9% (Figure 6.2b), a small twin embryo nucleates from the intersection between the grain boundary (GB) and free surface, and grows to transverse through the nanocrystal under continual loading (Figure 6.1b). Figure 6.1d-f confirms that the observed shear band in the $[\bar{1}10]$ oriented crystal is indeed a twin band with the active twinning system of $[\bar{1}11](\bar{1}12)$, as evidenced by the Fast Fourier Transform (FFT) pattern and a zoom-in image. The resolved shear stress on the $(\bar{1}12)$ plane for twin nucleation is about 9 GPa (Figure 6.2). After formation of a complete twin band, the lattice strain is released to about 1.3% (Figure 6.2c). A further increase of the applied strain causes thickening of the twin band, thus producing an increased amount of plasticity (Figure 6.1c). Moreover, the deformation twins are also observed under other loading orientations, such as ⟨100⟩ tension and ⟨111⟩ compression (Figure 6.4).

To understand the twinning mechanism of W nanocrystals, MD simulations are performed for both single and bi-crystal W nanowires (Figure 6.1g-k). In the $[\bar{1}10]$-oriented single crystal, a twin embryo nucleates from the surface (Figure 6.1g) and grows laterally to penetrate the whole nanowire (Figure 6.1h-i). Then, the twin band thickens through layer-by-layer vertical growth at the twin boundary via 1/6⟨111⟩ twinning dislocations nucleated on adjacent {112} planes (Figure 6.1j). The resolved shear stress on $(\bar{1}12)$ plane for twin nucleation obtained from the simulations is 8 GPa, in reasonable agreement with experiment. The bi-crystal nanowire exhibits twin nucleation and growth from the GB/surface intersection (Figure 6.1k),

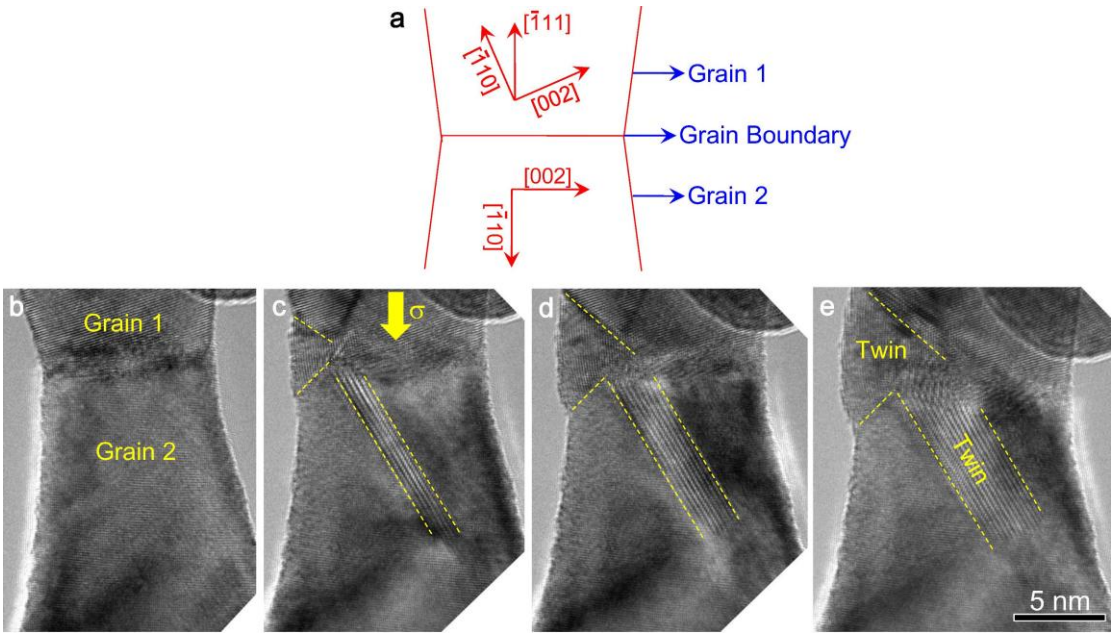

Figure 6.3 Nucleation of deformation twins at the GB/surface intersections in a W bi-nanocrystal under compression. (a) The orientation relationship between the two grains in the W bi-nanocrystal. The upper grain is loaded along $[\bar{1}11]$ while the lower grain is $[\bar{1}10]$. (b-c) Under compression, deformation twins are observed to nucleate from both the GB and the GB/surface intersection. (d-e) The deformation twin grows layer-by-layer both inside one of the grains in one location and into both of the grains of W bi-nanocrystal in another.

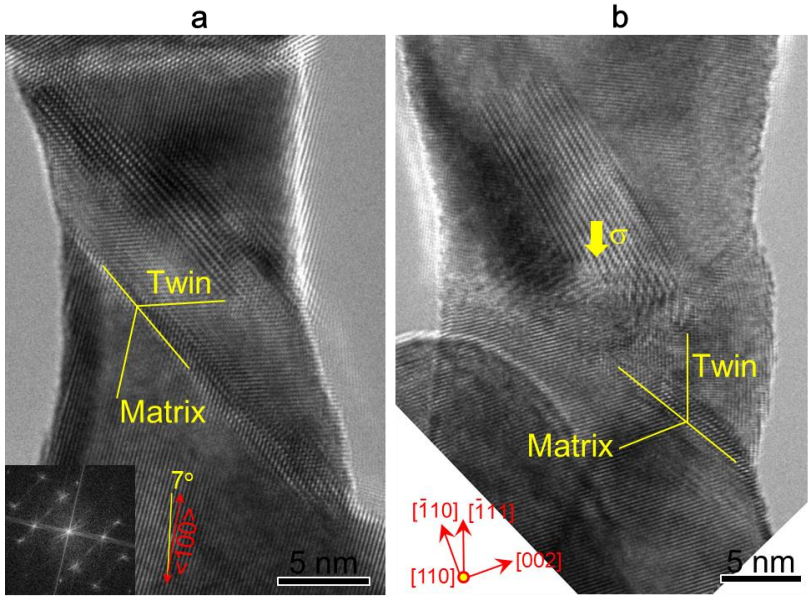

Figure 6.4 Orientation-dependent deformation twinning in W nanocrystals. (a) Deformation twinning under [100] tension. (b) Deformation twinning under $[\bar{1}11]$ compression.

which penetrates into both crystals, similar to the observations in some of our experiments (Figure 6.3). The behavior and morphology of deformation twinning depend significantly on the nucleation site, the geometry, and most notably the diameter of the nanowires. First, for W nanowires with thicknesses around 1-2 nm, the twin can penetrate the whole cross-section of the nanowire when nucleates with layer-by-layer growth occurring after nucleation. However, when the W nanowires are several nanometers in diameter, the twin thickens after nucleation, during propagation (Figure 6.1g-j). Second, the nucleation and growth of the twin is affected by the nucleation site and nanowire geometry, indicated by the different nucleation behaviors between single crystal and bi-crystal. For the bi-crystal, the twin nucleates from the GB/surface intersection and only has to propagate through a small fraction of the thickness, and thus only single twinning dislocations are observed. In this case, the twin is not observed to thicken prior to the twinning dislocation passing through the crystal (Figure 6.1k). In the single crystal (Figure 6.1g-j), however, the twin must nucleate from the surface and must penetrate the whole diameter which allows for the observation of multiple twinning dislocations (*i.e.* thickening prior to complete propagation). These MD simulation results compare favorably with our experimental observations, which suggest that the twinning mechanism in W nanocrystal changes from pole mechanisms typically used to explain twinning in the bulk[110,226] to surface or GB nucleated twining dislocations at the nanoscale (Figure 6.1 and 6.3).

6.3.2 Pseudoelastic behavior of deformation twinning in W nanowires

Deformation twinning in W nanocrystals is found to be pseudoelastic, manifested as reversible detwinning during unloading. That is, during compressive loading, the W nanocrystal experiences large plastic deformation via deformation twinning (Figure 6.5a-b,f-g), the thickness

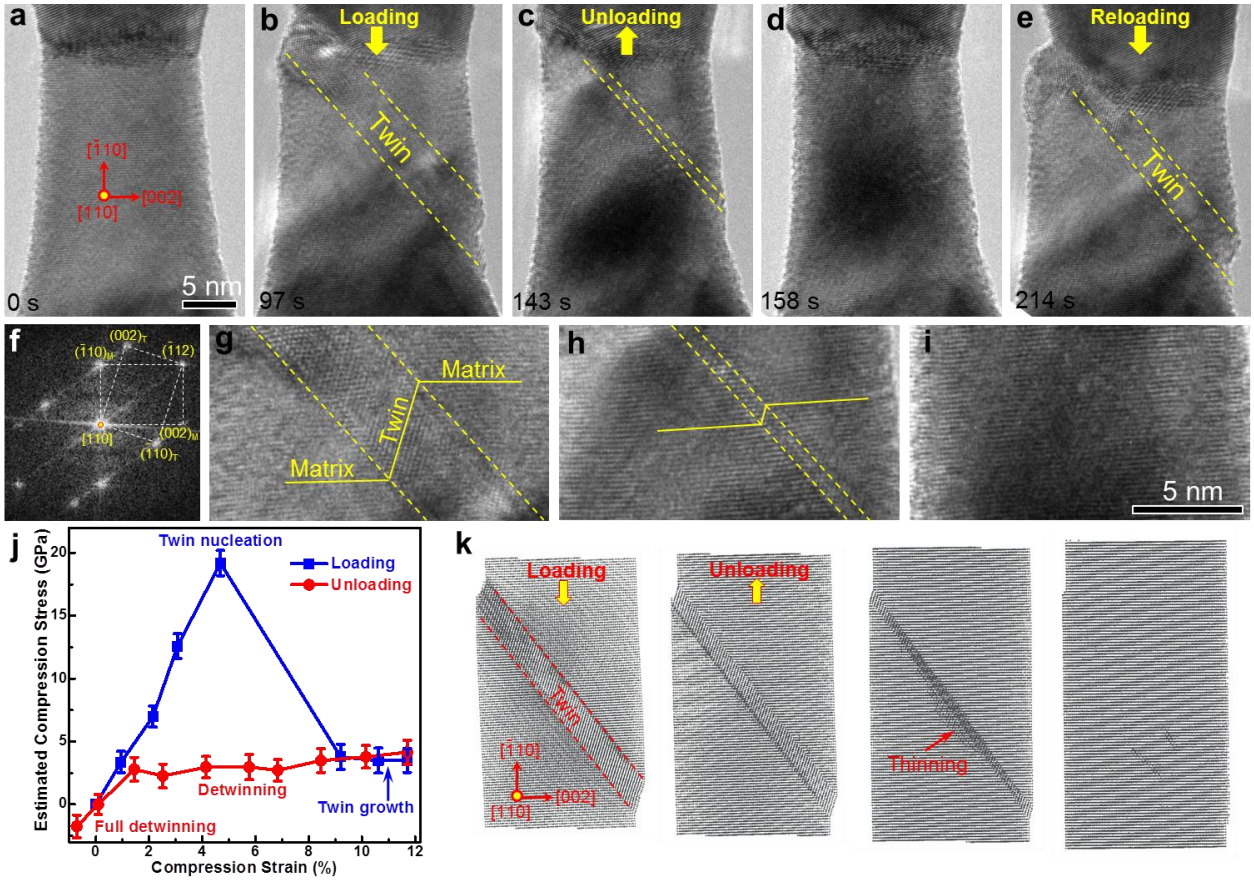

Figure 6.5 Reversible deformation twinning and detwinning processes in a W nano bi-crystal under $[\bar{1}10]$ cyclic loading. (a) A pristine W nano bi-crystal nanowire with the diameter 14.7 nm as viewed along [110] and loaded along $[\bar{1}10]$. (b, g) Under compression, the deformation twin nucleates and grows to about 4 nm. (c, h) A layer-by-layer detwinning process occurs when the loading is reversed (also see Supplementary Movie 3). (d, i) After complete detwinning, the W nanocrystal recovers its original shape. (e) A deformation twin nucleates at the same place in subsequent deformation cycles. (f) The FFT pattern of the deformation twin. (j) Stress versus strain curve during compressive loading and unloading, showing the pseudoelastic response. The stress is estimated based on the lattice strain, while the compression strain is measured from the change of nanowire length. (k) MD snapshots, showing the twinning and detwinning process similar to TEM observations.

of which is about 4 nm just before the unloading (Figure 6.5g). However, when the loading is reversed plastic deformation mainly occurs at the twin boundary via layer-by-layer detwinning (Figure 6.5c,h). The detwinning process occurs in the same fashion as the twinning process through the nucleation and propagation of twinning dislocations, which decreases the twin thickness and returns the nanocrystal to its original shape with no apparent defects finally (Figure 6.5d,i). Pseudoelasticity is also manifested in the stress-strain curve which shows the recovery of initially zero stress and strain values after a loading-unloading cycle (Figure 6.5j). During multiple loading/unloading cycles, the deformation twin is always observed to nucleate at the same location (Figure 6.5e). The pseudoelastic twinning is also observed in the MD simulations. Figure 6.5k shows the MD snapshots of a detwinning process during unloading, which occurs layer-by-layer at the twin boundary via 1/6⟨111⟩ dislocations nucleated on adjacent {112} planes, consistent with TEM observation.

6.3.3 Loading orientation dependent deformation in W nanowires

The deformation twinning dominates for several other loading orientations tested, including <110> compression, ⟨100⟩ tension and ⟨111⟩ compression (Figure 6.1, 6.3 and 6.4). However, the dislocation slip prevails under ⟨112⟩ loading, for both tension and compression. Figure 6.6 and 6.7 shows the dislocation-mediated plastic deformation of a W nanocrystal under [112] compression and tension, respectively. Since the deformation of W nanocrystals under under [112] compression and tension are similar, here it will focus on the deformation under [112] compression. At the beginning, the W nanocrystal is nearly pristine with no observable dislocations (Figure 6.6a). Under the compressive loading, dislocations are observed to nucleate

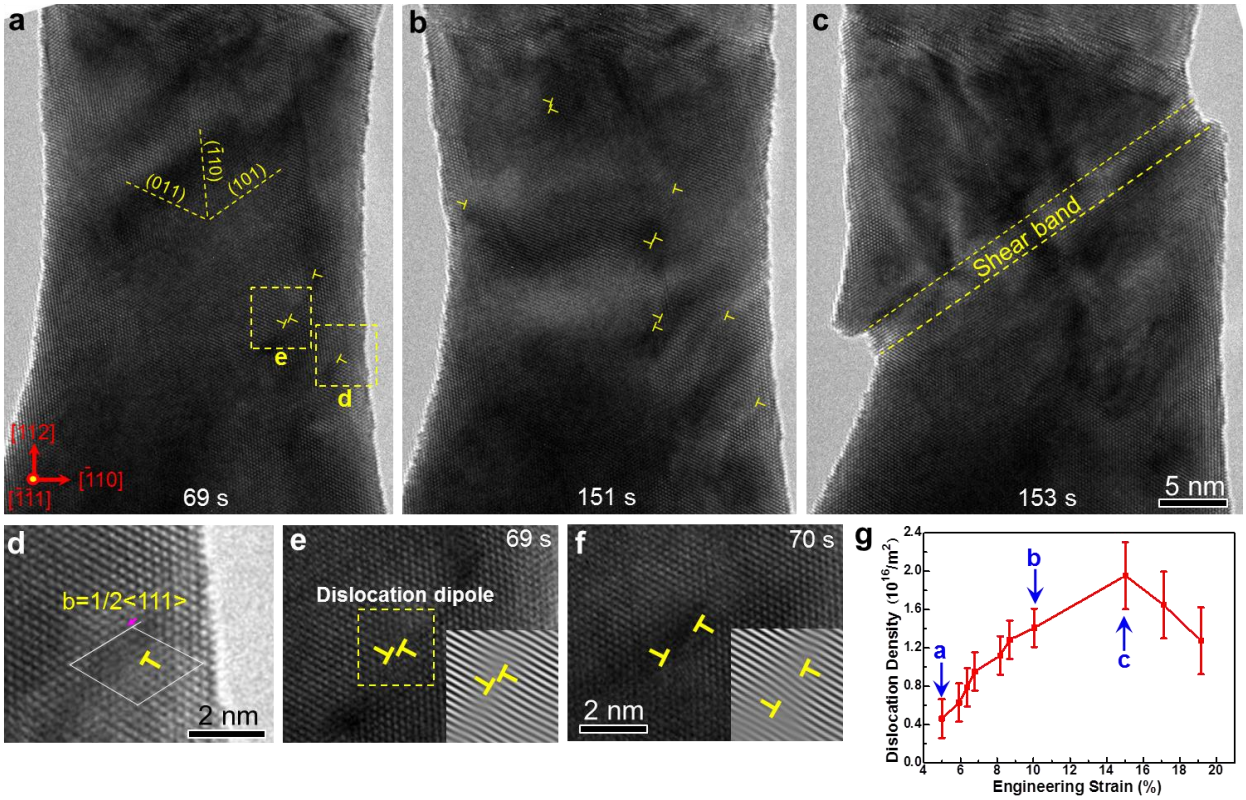

Figure 6.6 Dislocation dynamics inside a W nanocrystal under [112] compression. (a-c) Sequential images showing the deformation of a W nanocrystal under [112] compression, as viewed along $[\bar{1}\bar{1}1]$; exhibiting dislocation nucleation and the formation of a shear band. The dislocations are marked by an upside-down "T". (d) The Burgers vector shows the dislocation nucleated from side surface is a 1/2⟨111⟩-type mixed dislocation. (e-f) Sequential images showing the nucleation and dynamics of a dislocation dipole under [112] compression. (g) The statistical dislocation density evolution with the compressive strain.

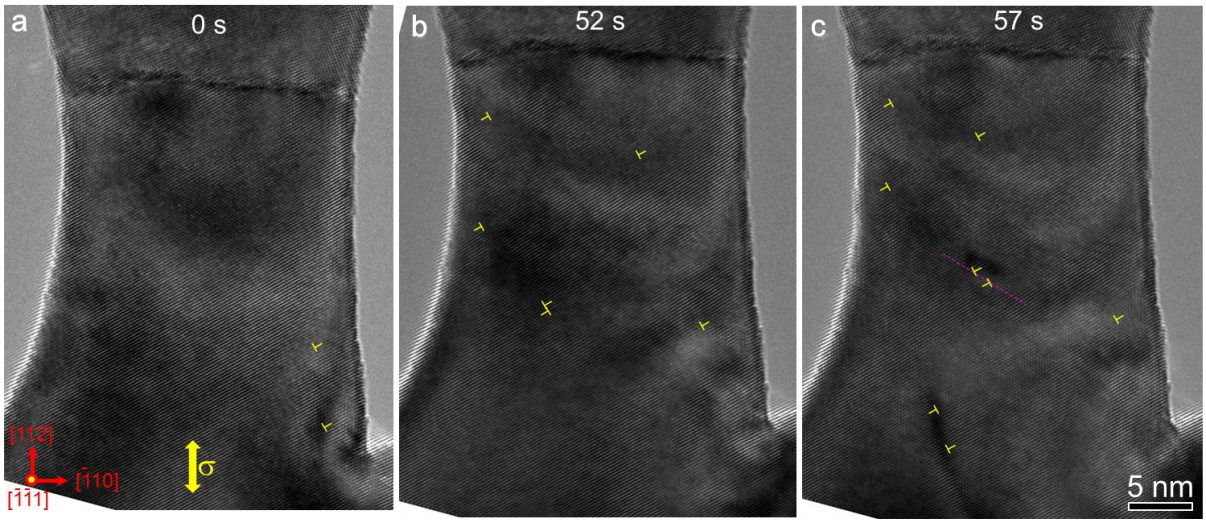

Figure 6.7 Dislocation dominated plastic deformation in a W nanocrystal under [112] tension. (a) Some dislocations exist in the pristine W nanocrystal. (b-c) Under tension loading, more dislocations are observed to nucleate simultaneously from multiple-sources.

simultaneously from multiple sources with the estimated nucleation stress of ~ 7.2 GPa on the (101) slip planes (Figure 6.6a-b). Most of the dislocations appear to nucleate as dipoles (Figure 6.6), which are likely the surface-nucleated half loops on {110} planes. It is worth noting that in most of these dipoles the two dislocations lie on the same slip plane, though some occur on adjacent slip planes (Figure 6.6 and 6.7). Dislocations in the dipoles are mobile, resulting in the expansion of those dipoles on the (101) slip planes after nucleation (Figure 6.6e-f). Further deformation results in the formation and thickening of a shear band along the (101) plane within which the dislocation density is as high as ~2×10^{16} m^{-2}, thus generating large local plastic strain (Figure 6.6c,g). Here it is noted that it has been notoriously difficult to determine the operative dislocation slip plane in BCC metals and the commonly used visual inspection of surface slip traces often caused confusions as to the {110} versus {112} slip[218,227]. In contrast, in situ HRTEM experiments conducted in current research enable a direct unambiguous determination

of the active slip plane in BCC W nanocrystals, i.e., a specific {110} plane depending on the loading orientation.

6.4 DISCUSSION

To understand the competition between deformation twinning and dislocation slip, atomistic studies are performed for W single crystals under ⟨112⟩ loading. In the direct MD simulations, either tension or compression, it is found that the plastic deformation is dominated by dislocation activities, including dislocation nucleation from the surface, glide inside the nanocrystal and entanglement with each other; some dislocations eventually escape from other parts of the surface under continual loading. The active dislocation behaviors in these MD simulations are consistent with the experimental observations. However, one might still be puzzled as to why dislocation slip is the active mode of plastic deformation under ⟨112⟩ loading, while twinning prevails for other loading orientations tested, including ⟨110⟩, ⟨100⟩, and ⟨111⟩.

To further study the twin and dislocation competition, it is noted that in FCC nanocrystals, the intrinsic lattice resistance is so low that the surface nucleated defects such as dislocations or twins can easily penetrate into the nanocrystal. As a result, plasticity in FCC nanocrystals is usually controlled by surface nucleation[20,43,184]. In contrast, in BCC nanocrystals, a surface nucleated defect experiences the intrinsically large lattice resistance as it grows into the nanocrystal. As a result, plasticity in BCC nanocrystals can be controlled by defect growth or migration rather than surface nucleation. In other words, even if a surface defect such as a twin embryo has been initiated at some favorable surface sites, its growth, including both the lateral and

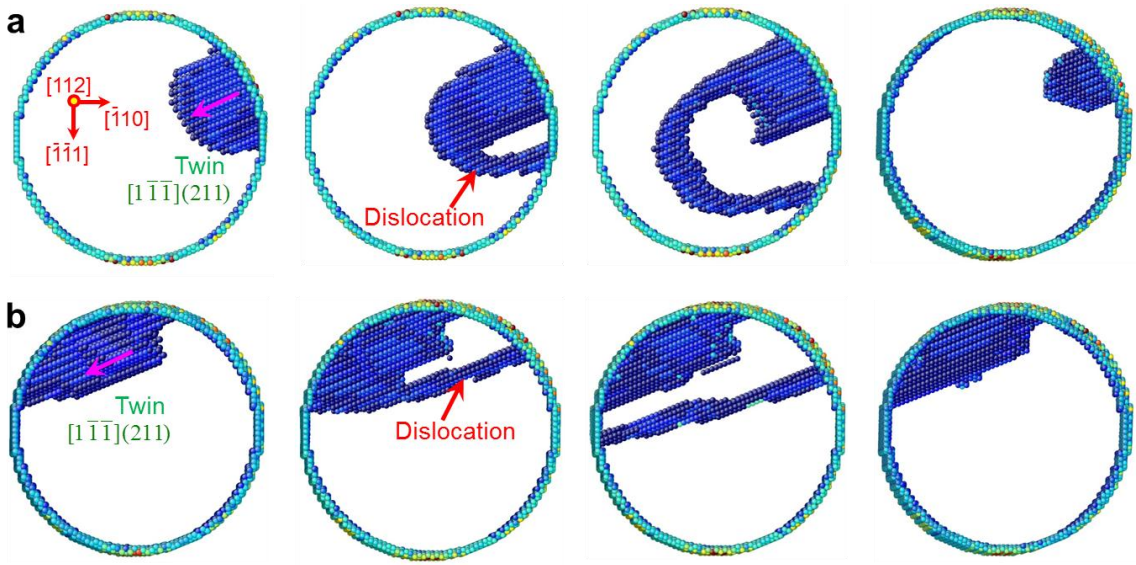

Figure 6.8 Atomistic simulations of competition between twinning and dislocation slip in W under [112] loading. (a) Nucleation and expansion of a dislocation loop from the edge of a pre-embedded twin embryo, whose edge is predominantly perpendicular to the twinning direction (pink arrow). (b) Similar to (a), except that the dominant edge of the twin embryo is parallel to the twinning direction. In both cases, the growth of the twin embryo is suppressed due to the competing nucleation of a dislocation that accommodates the load and results in shrinkage of the twin embryo.

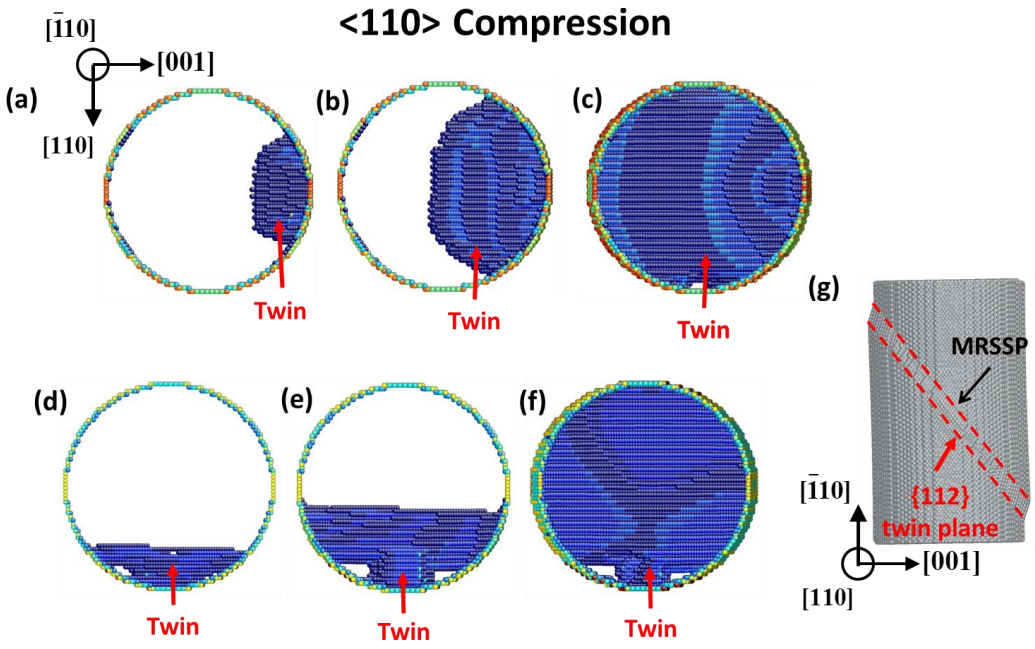

Figure 6.9 Atomistic simulations on the growth of twin embryo in W under [$\bar{1}$10] loading. (a-c) The growth of a twin embryo with an edge-dominant front. (d-f) The growth of a twin embryo with a screw-dominant front. In both cases, twin embryo grows to form a twin plate across the pillar, as shown in (g).

Table 6.1 Largest Schmid factors on the dislocation slip and deformation twinning systems for the four loading orientations tested in BCC W

Loading orientation	Dislocation		Twinning		Dominant mechanism in experiment
	Slip system	Schmi factor	Twin system	Schmid factor	
$[\bar{1}10]$	$[\bar{1}\bar{1}1](\bar{1}01)$	0.4082	$[\bar{1}\bar{1}1](\bar{1}12)$	0.4714	Twinning
[112]	$[\bar{1}\bar{1}1](101)$	0.4082	$[\bar{1}\bar{1}1](211)$	0.3928	Dislocation slip
[100]	$[\bar{1}\bar{1}1](\bar{1}\bar{1}0)$	0.4082	$[\bar{1}\bar{1}1](2\bar{1}\bar{1})$	0.4714	Twinning
$[\bar{1}11]$	$[\bar{1}\bar{1}1](\bar{1}01)$	0.2722	$[\bar{1}\bar{1}1](\bar{1}12)$	0.3143	Twinning

vertical mode as schematically shown in Figure 6.1h, still has to compete with and even be overridden by other modes of defect nucleation and growth. To explore the defect growth limited plastic deformation, a twin embryo is created near the surface of a [112]-loaded W nanocrystal (Figure 6.8a). This embryo belongs to the twinning system of $[\bar{1}\bar{1}1](211)$, which is subjected to the largest resolved shear stress among all possible twinning systems under [112] compression (Figure 6.4c). During MD simulations under various applied stresses, the nucleation of individual dislocation loops near the twin embryo is always observed, rather than the growth of the twin itself. Similar dislocation-dominated responses are observed when a twin embryo is created at other surface locations (e.g., Figure 6.8b). These results demonstrate that the expansion of the twin embryo can be limited by its lateral growth under [112] compression. In contrast, for other loading orientations studied, the twin embryo created at the surface always grows to form a complete twin band and then thickens through layer-by-layer migration of twin boundary, as seen during $[\bar{1}10]$ compression (Figure 6.9). These atomistic studies clearly demonstrate that the surface nucleated twin embryos cannot continue to grow during <112>

compression, thereby highlighting the growth controlled defect process in BCC nanocrystals owing to the intrinsically high lattice resistances. These MD results also reinforce the notion of twinning-dominated plasticity in BCC W nanocrystals, except for ⟨112⟩ loading.

Further insights into the competition between deformation twinning and dislocation slip are gained by analysis of the resolved shear stress on the respective twin and slip systems. Currently, there is a lack of established criteria for selecting the active mode of deformation twinning or dislocation slip in BCC metals. However, one expects that the resolved shear stress should play an important role. Table 6.1 lists the largest Schmid factors of twinning and dislocation slip for each of the four loading orientations tested. Under ⟨110⟩, ⟨100⟩ and ⟨111⟩ axial loadings, the corresponding Schmid factors of twinning are larger by a finite margin than those of dislocation slip. This is consistent with the observed twinning dominated plasticity in experiments. However, for ⟨112⟩ axial loading, the Schmid factors of twinning and dislocation slip are very close, which implies the similar resolved shear stresses to drive twin growth and dislocation glide. In this case, the above atomistic simulations shown in Figure 6.8 suggest that the active mode of dislocation shear is favored possibly due to the difficulty of lateral growth of the twin embryo. Nevertheless, a mechanistically-based, quantitative criterion for selecting the deformation twinning versus dislocation slip warrants further research in future.

Finally, we note that in addition to gaining new insight into deformation mechanisms, the in situ welding technique developed in this work provides a relatively simple means of sample preparation to facilitate the in situ atomic-scale mechanical testing of nanostructures without surface damage. Our study also demonstrates the advantage of in situ HRTEM deformation experiments that allows the unambiguous determination of active systems of dislocation slip and twinning, which has been a challenge for BCC crystals.

6.5 CONCLUSIONS

In conclusion, the combined in situ TEM experiments and atomistic simulations have revealed that deformation twinning is the dominant deformation mode in BCC W nanocrystals at room temperature and low strain rates, when loaded along ⟨100⟩, ⟨110⟩ and ⟨111⟩ directions. Under cyclic loads, deformation twinning is pseudoelastic and such a unique nanoscale deformation behavior could enable large actuation, energy storage and mechanical damping in micro/nano-devices. However, in situ TEM experiments also reveal the prevalent dislocation activities for ⟨112⟩ loading. The loading orientation effect is attributed to the defect growth controlled plasticity in small-scale BCC nanocrystals with high lattice resistances, which contrasts with the nucleation controlled plasticity in FCC counterparts. Broadly, our work demonstrates that the combined in situ HRTEM nanomechanical testing and atomistic modeling enable a deeper understanding of the fundamental deformation mechanisms in nanomaterials, and such integrated research may ultimately enable the design of nanostructured materials to realize their latent mechanical strength to the full.

7.0 CRYSTAL STRUCTURES ON THE DEFORMATION OF SMALL VOLUME FCC AND BCC METALS

In Chapters 4-6, the deformation mechanisms of FCC and BCC metals have been discussed. In this chapter, the commonalities and differences between FCC and BCC metals deforming at small length scale will be further explored, in both dislocation nucleation and deformation twinning. For both BCC and FCC nanocrystals, the deformation twinning can serve as the dominated plastic deformation mode under room temperature and low strain rates; while differences between BCC and FCC nanocrystals are observed in the twinning growth and dislocation nucleation modes, due to their distinct dislocation-core structures and intrinsic lattice resistances. The discussions presented in this chapter are helpful for understanding the differing size dependent strengthening in FCC and BCC nanopillars.

7.1 INTRODUCTION

It is well known that the deformation behavior of FCC and BCC metals can differ substantially[20,85]. In FCC metals, the dislocations have planar cores and thus have high mobility. The plasticity of bulk FCC metals with moderate to high stacking fault energies[214] is governed by dislocations-obstacle interactions. In FCC metals with ultra-low stacking fault energies, twinning can serve as the dominant deformation mechanism at room temperature (RT)[110]. In

BCC metals, however, screw dislocations have a non-planar core structure and experience a high lattice resistance[20,132]. Consequently, the plasticity of bulk BCC metals is strongly temperature and strain rate dependent[85]. At RT and moderate strain rates, plasticity of bulk BCC metals is controlled by the motion of screw dislocations[85,118,134,135,228]. At high strain rates or liquid nitrogen temperatures[110,113,119,136], the stress required to move screw dislocation increases significantly, allowing twinning to become a competing deformation mechanism[113]. Given these differences at macroscopic scales, it is interesting to consider what might happen as the sample dimensions are decreased down to the nanoscale.

Based on the results presented in this dissertation and reported in literature, the differences between FCC and BCC metals deforming at small length-scale will be explored and discussed in this chapter.

7.2 DISCUSSION

It is worthwhile to note several important commonalities and differences in the plastic deformation in FCC and BCC nanocrystals. First, the competition between deformation twinning and dislocation slip occurs in both FCC and BCC nanocrystals, and mechanical twinning can become the dominant plastic deformation mode at room temperature and low strain rates in both of them. As reviewed in Chapter 2, the deformation twinning in FCC nanocrystals has been well documented in literature[107,112,130,197]. However, it is largely unexplored in BCC metals due to the difficulties in the synthesis of BCC nanosized sample. The results shown in this dissertation provide the first direct experimental evidence of the twinning dominated plasticity in BCC W nanocrystals at room temperature and low strain rates. The physical origin of twinning

dominance in nanoscale FCC and BCC metals can be attributed to the prevalent high stresses required for the plastic deformation at small length scale, i.e. “smaller is stronger”. Such high stresses favor the twinning shear over the dislocation slip.

However, the twin growth in BCC metallic nanocrystals is different from that in the nanosized FCC metals. The deformation twinning in FCC metallic nanowires, such as Au, are strongly affected by the loading orientation, i.e. the Schmid factor. For a given loading direction, deformation twinning can be formed by the successive nucleation of leading partial dislocation on the adjacent slip planes, if the Schmid factor of trailing partial is lower than the leading ones[20]; otherwise, the trailing partial will nucleate on the same slip plane and remove the slip trace of leading partial to form a full-slip. Thus, the minimum stable deformation twinning in FCC metals has two-layers in thickness[137]. Whereas, the Schmid law on deformation twinning breaks down in BCC metals due to the non-planar dislocation core[229] and no stacking fault in BCC metals. Although the nucleation of deformation twinning in BCC metals also conducts in the manner of layer-by-layer growth on the adjacent twinning plane, a critical thickness is required for a stable twin embryo. For example, in bcc Mo and W[137,145], the twin embryo with two-layers is metastable, while the twin embryos with three- and four-layers are unstable. Steady growth of twin occurs only when the twin embryo achieves five-layers. As a result, the initial growth of deformation twin in BCC metals needs to overcome a relatively large lattice resistance, unlike the FCC metals. The atomistic simulations presented in Chapter 6 also demonstrate that the growth and propagation of twin embryos in BCC metals are strongly limited by their lateral growth, while the vertical growth of twin is relatively easy, because the latter growth mode involves the glide of twin interface dislocations with low energy barriers[137]. As a result, dislocation slip can dominate over twinning for certain loading conditions, such as ⟨112⟩ tension

and compression in W nanocrystals. However, such orientation-dependent deformation mode in BCC metals remains unclear. A mechanistically-based, quantitative criterion for selecting the twinning versus dislocation slip warrants further research in the future.

Second, the dislocation starvation is typical in FCC nanocrystals (such as Cu)[68], but not observed in the BCC W nanocrystals, even the smaller crystal size studied here. In the deformation of FCC nanocrystals, dislocation will be exhausted during deformation, leading to the dislocation starvation, and as a result, the nucleation of new dislocations is required for the further deformation, which will be controlled by the dislocation sources[45,69]. On the contrary, in BCC nanocrystals under ⟨112⟩ loading, numerous nucleation events can occur nearly simultaneously, and a gradual increase in dislocation density occurs during continual loading, in different from the single nucleation process observed in FCC metals (See Chapter 4). Such difference can be attributed to the intrinsically high versus low lattice resistances of dislocations in BCC versus FCC metals. Moreover, in nanosized BCC metals, the self-multiplication can conduct during the propagation of those surface nucleated dislocations[40]. As a result, the dislocation density in small-volume BCC metals will continually increase under the combined effect of multiple-sources nucleation and self-multiplication, which avoids the dislocation starvation. Those differences may play a role in the observed different strengthening trends in small scale FCC and BCC single crystals when dislocations serves as the dominant mechanisms of plastic deformation[40,71]. Also, the surface structure may affect the different dislocation nucleation behaviors, and the future studies are needed in understanding the surface structure.

Third, deformation twinning can be pesudoelastic in elemental BCC nanocrystals during loading and unloading, as shown in the results in Chapter 6. In contrast, while the deformation-induced twinning has been experimentally observed in FCC nanowires[107], the detwinning and

resultant pesudoelasticity has not been reported to date. It is of interest to note that the pesudoelastic deformation has been recently measured for the nanoscale shape memory alloys[216] and ceramics[217]. Pseudoelasticity could allow for reversible inelastic deformation, superelasticity, large actuation, energy storage and mechanical damping in micro/nano-devices[145,216,217].

7.3 CONCLUSIONS

In conclusion, the commonalities and differences in FCC and BCC nanocrystals deforming at nanoscale are discussed in this chapter, in both dislocation and deformation twinning. Deformation twinning can serve as the main plastic deformation mode at room temperature and low strain rates in both nanosized BCC and FCC metals. But, the dislocation nucleation modes and twinning growth mechanisms in BCC and FCC nanocrystals are distinct, contributing to the observed differing size-dependent strengthening in small-volume FCC and BCC single crystals.

8.0 SUMMARY AND CONCLUSIONS

The main objective of this dissertation is to understanding the relationships between structure-mechanical properties-deformation mechanisms in small volume crystals. FCC and BCC metallic nanowires were used as the model materials for this project, and in situ nanomechanical testing under HRTEM was employed to reveal the atomic-scale dynamic processes during the deformation of those FCC and BCC metallic nanowires.

It was discovered that the surface-nucleated dislocations can strongly interact inside the confined volume of Au nanowires. Those dislocation interactions can lead to a new type of dislocation-originated SFT via an intersection and cross-slip process, in distinct to the widely believed vacancy-originated SFT. Such formation mechanism of SFT is applicable to a broad class of FCC metals and alloys. Moreover, the dynamic processes of this deformation-induced dislocation-originated SFT can conduct in a manner that is not expected in the bulk samples, which serves as an important deformation mode in controlling the plasticity and strain hardening at nanoscale. This result advances the knowledge about the 3D volume defects in FCC metals and alloys.

Microstructure strongly affects the mechanical properties, deformation mechanisms and plasticity of materials. By introducing the coherent twin boundaries into Au nanowires, the strength of those Au nanowires can be improved significantly. Quantitative measurements show that Au nanowires containing angstrom-scaled twins (0.7 nm in thickness) exhibit tensile

strengths up to 3.12 GPa, close to the ideal strength limit of perfect Au crystals. However, approaching such nanotwin size limit gives rise to a remarkable ductile-to-brittle transition that is governed by the heterogeneous-to-homogeneous dislocation nucleation transition in Au nanowires, profoundly contrasting with the behavior of metallic nanowires with lower-density twins reported so far. Such twin-size dependent deformation is a new type of size effect in different from the crystal size effect described previously. This result is of fundamental and technological importance for future design and fabrication of ultra-strength materials.

Twinning is a fundamental deformation mode that competes against dislocation slip in crystals. In bulk BCC metals, the deformation twinning only occurs under high strain rate and/or low temperature, under which higher stress are required for the plastic deformation. However, as the crystal size decreased down to the nanoscale, deformation twinning can serve as the dominant deformation mode in BCC-tungsten nanocrystals at room temperature and low strain rate. The deformation twinning in BCC metals shows a pseudoelastic behavior under cyclic loading, which enables mechanical damping in nanodevices. A competition between twinning and dislocation slip is observed in W nanocrystals when the loading orientations are changed, which is controlled by the defect growth controlled plasticity in BCC materials deformed at small length scale.

Based on the results presented in this dissertation, the effects of crystal structure on the deformation of small volume materials were further explored. Several important commonalities and differences in FCC and BCC nanocrystals deforming at nanoscale were further proposed, in both dislocation and deformation twinning. As the crystal size decreases, deformation twinning can become the main plastic deformation mode in both BCC and FCC nanocrystals at room temperature and low strain rates, due to the higher stress required for the dislocation activities at

nanosclae. While BCC and FCC nanocrystals are different in both the twinning growth and dislocation nucleation modes, due to their distinct dislocation-core structure and intrinsic lattice resistance. Those differences may contribute to the observed differing strengthening trends in small scale FCC and BCC single crystals.

The results from this dissertation advance our fundamental understanding of plastic deformation in a broad class of metals and alloys, and are of technological importance for degradation control and future design of ultra-strength nanomaterials.

9.0 OUTLOOK

The results presented this dissertation were mainly focused on the real-time structure evolutions and deformation mechanisms in small-volume metals under mechanical loading. However, the recent development of micron/nano electro-mechanical systems (MEMS/NEMS) and portable electronics requires to reveal the materials' responses under the coupling effect of mechanical and electronic damage, which is critically important for the development of high performance materials in real applications. Here, some examples will be used to show the current research and future directions in the related fields.

Lithium-ion batteries are one of the most important parts that could revolutionize portable electronics and will be key to electrifying transport vehicles and delivering renewable electricity. However, the large volume changes upon lithium insertion and extraction will lead to the capacity fading and cycability loss. Understanding the atomic-scale structural evolution during the electrochemical reactions in solid-state electrodes is critically important to the development of high-performance Li-ion batteries. In the past few years, we have successfully developed several experimental setups for the in situ studies on the structure changes during the electrochemical processes in lithium and sodium ions batteries[17,30,31,230-235]. In a typical experiment, a nano-battery was constructed in the half-cell configuration, as shown in Figure 9.1. The working electrode was a uniform a-Si layer (yellow) coated on an individual carbon nanofiber (black). A Li metal on a W probe was the counter electrode, and the native Li_2O layer

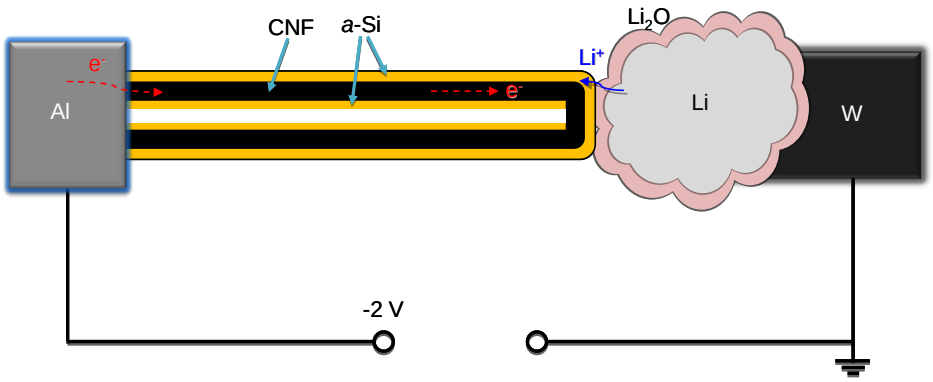

Figure 9.1 Schematic illustration of *in situ* electrochemical lithiation inside a TEM.[30]

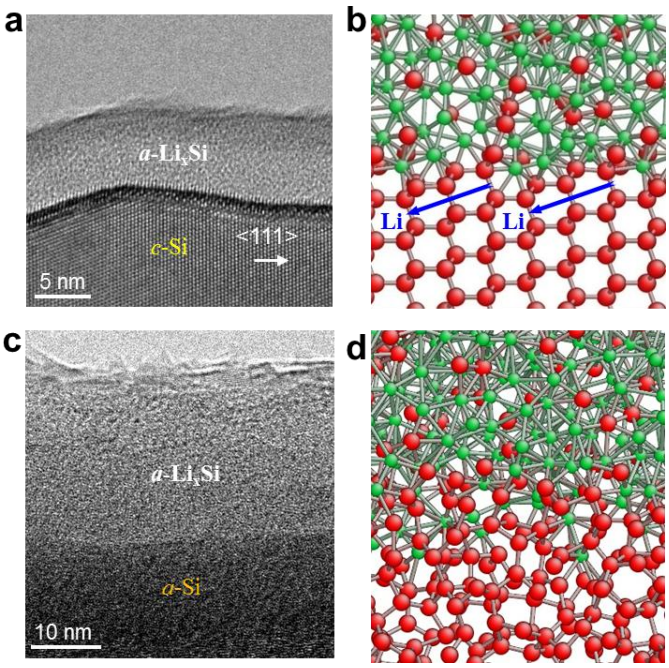

Figure 9.2 Comparison of the two-phase lithiation mechanism in *c*-Si and *a*-Si. (a) A high resolution TEM image showing a sharp phase boundary between the reactant of *c*-Si and the product of *a*-Li_xSi. (b) A snapshot from MD simulation showing the atomic structures near the amorphous-crystal phase boundary. The Li concentration is locally high near the surface of *c*-Si and a group of Li atoms collectively weaken the strong Si-Si covalent bonding, thereby facilitating the dissolution of Si atom from *c*-Si surface. (c) A HR TEM image showing a sharp phase boundary between *a*-Si and *a*-Li_xSi (x ~ 2.5). (e) A snapshot from MD simulation showing the atomic structures near the amorphous-amorphous interface. The *a*-Si consists of a continuous random network of Si atoms. Similar to (b), the Li concentration is locally high near the surface of *a*-Si.[30]

on Li metal served as a solid-state electrolyte for Li transport. By applying a negative potential on the lithium side, the electrochemical lithiation can be started. This experimental setup allows the atomic-scale observations on the structure change during the lithiation. By using this experiment setup, it was discovered that the lithiation of crystal silicon (c-Si) is controlled by the atomic-scale ledge mechanism, which gives rise to the crystallographic orientation dependence of lithiation-induced swelling (Figure 9.2a-b); while the lithiation of amorphous Si (a-Si) is mediated by an unexpected two-phase lithiation mechanism, which is opposite to the widely believed single-phase lithiation in a-Si (Figure 9.2c-d). These discoveries elucidate the atomistic origin of morphological change and mechanical degradation in lithiated electrodes, and have important application in the design of novel Si-based anodes that can alleviate the lithiation-induced failure and fracture.

Although the modified experimental setup can be used to study the lithiation/sodiation behaviors of different anode materials, including nanowires, nanoparticles and thin films, they does not work very well in the application of studying the cathode materials, such as $LiFePO_4$. The difficulties of the experiments might be due to the different kinetics, which is considerably affected by the factors such as experimental configuration. However, the differences are not understood very well at present. Future efforts are needed to reveal the structure evolution of cathode materials during electrochemical cycling, considering their limitations on battery performances. Another direction is the in situ liquid cell. Although the all-solid cell setup provides the advantage for the atomic-scale observation on the lithiation mechanisms, in situ study on the lithiation behaviors of electrodes in liquid electrolyte is necessary to simulate the real working conditions in batteries, which may leads to the different reaction kinetics. Some

progresses have been made in this direction; however, most of the results might be caused by the artifacts due to the exposure to electron beam.

On the other hand, electronic pulse is frequently used in MEMS/NEMS, nanodevice, transistor and memristor. However, the materials responses under electronic pulse conditions are largely unexplored, due to the technological difficulties in combining TEM with pulse generator. By changing the power source of the electrochemical experimental setup into a pulse generator, we have developed a method to couple the in situ observation and pulse source together. By using this method, ultrafast cooling (higher than 10^{14} K s^{-1}) can be achieved inside TEM, which could keep the liquid structure of pure BCC metals (such as Mo and V) down to the room temperature[236]. As a result, those pure metals were converted into their amorphous phase, i.e. monatomic metallic glasses, which solved a long-standing question in material science. By well-controlling the applied pulse, other interesting phenomenon are also discovered, such as the interface migration. However, the potential mechanisms of the material response and damage under pulse conditions are largely unknown due to the ultrafast structure change. Experimental studies combined with atomic-scale simulations are needed to reveal those fundamental physical processes. This method also has potential application in the study of the phase change mechanism in memristor.

In summary, current progresses in several related fields are briefly discussed and the problems existed are proposed. Great efforts need to be made before we can achieve an in-depth understanding on the material responses under the coupled effects of mechanical and electronic loading.

APPENDIX A

YOUNG'S MODULUS OF W SINGLE CRYSTAL

To estimate the yield stress and defects nucleation stress in W single crystals under mechanical loading, the young's modulus of W single crystals along different crystallographic direction need to be known. In theory, the Young's modulus of W single crystal along ⟨110⟩ and ⟨112⟩ directions can be calculated by using[60]:

$$E_{ijk} = \{S_{11} - 2(S_{11} - S_{12} - S_{44}/2)(l_{i1}^2 l_{j2}^2 + l_{j2}^2 l_{k3}^2 + l_{i1}^2 l_{k3}^2)\}^{-1}$$

where E_{ijk} is the Young's modulus along the [*ijk*] directions, respectively; S_{11}, S_{12}, S_{44} are the elastic compliances of W; l_{i1}, l_{j2}, l_{k3} are the direction cosines of the [*ijk*] direction. The elastic compliances for W single crystal at room temperature is S_{11}= 0.257×10^{-2} GPa^{-1}, S_{12}= -0.073×10^{-2} GPa^{-1}, S_{44}= 0.66×10^{-2} GPa^{-1}, respectively[60]. The directions cosines for ⟨110⟩ and ⟨112⟩ orientations are listed in Table A.1. Thus, the Young's modulus of W single crystal along ⟨110⟩ and ⟨112⟩ directions are calculated to be $E_{110} = E_{112} = 389$ GPa. The yielding stress of different W nanocrystals are calculated by using $\sigma = E\varepsilon$, where ε is the maximum elastic strain the material experienced just before yielding. While, the resolved shear stress on the shear plane can be obtained by using $\tau = m\sigma$, where *m* is the Schmid factor on the corresponding slip systems. For

the W nanocrystal loaded along $[\bar{1}10]$ in Figure 6.1, the Schmid factor for $[\bar{1}\bar{1}1](\bar{1}\bar{1}2)$ twinning system is 0.47. For the W nanocrystal loaded along $\langle 112 \rangle$ in Figure 6.6 and 6.7, the Schmid factor for $[1\bar{1}\bar{1}](101)$ dislocation slip system is 0.41.

Table A.1 Directions cosines for $\langle 110 \rangle$ and $\langle 112 \rangle$ orientations in BCC W

Direction cosines	l_{i1}	l_{j2}	l_{k3}
$\langle 110 \rangle$	$\sqrt{2}/2$	$\sqrt{2}/2$	0
$\langle 112 \rangle$	$1/\sqrt{6}$	$1/\sqrt{6}$	$2/\sqrt{6}$

BIBLIOGRAPHY

1 Atwood, G. Phase-change materials for electronic memories. *Science* **321**, 210 (2008).

2 Loke, D., Lee, T. H., Wang, W. J., Shi, L. P., Zhao, R., Yeo, Y. C., Chong, T. C. & Elliott, S. R. Breaking the Speed Limits of Phase-Change Memory. *Science* **336**, 1566-1569 (2012).

3 Lita, A. E., Rosenberg, D., Nam, S., Miller, A. J., Balzar, D., Kaatz, L. M. & Schwall, R. E. Tuning of tungsten thin film superconducting transition temperature for fabrication of photon number resolving detectors. *IEEE Trans. Appl. Supercond.* **15**, 3528-3531 (2005).

4 Huang, Y., Duan, X., Cui, Y. & Lieber, C. M. Gallium nitride nanowire nanodevices. *Nano Lett.* **2**, 101-104 (2002).

5 Zhan, Y., Nakajima, M. & Fukuda, T. in *Micro-NanoMechatronics and Human Science, 2009. MHS 2009. International Symposium on.* 237-242.

6 Lee, S. W., Park, S. J., Campbell, E. E. & Park, Y. W. A fast and low-power microelectromechanical system-based non-volatile memory device. *Nat. Commun.* **2**, 220 (2011).

7 Burghard, M., Klauk, H. & Kern, K. Carbon-Based Field-Effect Transistors for Nanoelectronics. *Adv. Mater.* **21**, 2586-2600 (2009).

8 Gudiksen, M. S., Lauhon, L. J., Wang, J., Smith, D. C. & Lieber, C. M. Growth of nanowire superlattice structures for nanoscale photonics and electronics. *Nature* **415**, 617-620 (2002).

9 Wang, C., Hu, Y., Lieber, C. M. & Sun, S. Ultrathin Au Nanowires and Their Transport Properties. *J. Am. Chem. Soc.* **130**, 8902-8903 (2008).

10 Wang, J., Sansoz, F., Huang, J., Liu, Y., Sun, S., Zhang, Z. & Mao, S. X. Near-ideal theoretical strength in gold nanowires containing angstrom scale twins. *Nat. Commun.* **4**, 1742 (2013).

11 Jennings, A. T. & Greer, J. R. Tensile deformation of electroplated copper nanopillars. *Philos. Mag.* **91**, 1108-1120 (2011).

12 Jang, D., Li, X., Gao, H. & Greer, J. R. Deformation mechanisms in nanotwinned metal nanopillars. *Nat. Nanotechnol.* **7**, 594-601 (2012).

13 Bao, J., Bell, D. C., Capasso, F., Wagner, J. B., Mårtensson, T., Trägårdh, J. & Samuelson, L. Optical Properties of Rotationally Twinned InP Nanowire Heterostructures. *Nano Lett.* **8**, 836-841 (2008).

14 Protasenko, V. V., Hull, K. L. & Kuno, M. Disorder-Induced Optical Heterogeneity in Single CdSe Nanowires. *Adv. Mater.* **17**, 2942-2949 (2005).

15 Novo, C., Funston, A. M. & Mulvaney, P. Direct observation of chemical reactions on single gold nanocrystals using surface plasmon spectroscopy. *Nat. Nanotechnol.* **3**, 598-602 (2008).

16 Cui, L. F., Ruffo, R., Chan, C. K., Peng, H. L. & Cui, Y. Crystalline-Amorphous Core-Shell Silicon Nanowires for High Capacity and High Current Battery Electrodes. *Nano Letters* **9**, 491-495 (2009).

17 Liu, X. H., Wang, J. W., Huang, S., Fan, F., Huang, X., Liu, Y., Krylyuk, S., Yoo, J., Dayeh, S. A. & Davydov, A. V. In situ atomic-scale imaging of electrochemical lithiation in silicon. *Nat. Nanotechnol.* **7**, 749-756 (2012).

18 Chan, C. K., Peng, H. L., Liu, G., McIlwrath, K., Zhang, X. F., Huggins, R. A. & Cui, Y. High-performance lithium battery anodes using silicon nanowires. *Nature Nanotechnology* **3**, 31-35 (2008).

19 Zhu, T. & Li, J. Ultra-strength materials. *Prog. Mater. Sci.* **55**, 710-757 (2010).

20 Weinberger, C. R. & Cai, W. Plasticity of metal nanowires. *J. Mater. Chem.* **22**, 3277-3292 (2012).

21 Ma, F., Xu, K.-W. & Chu, P. K. Surface-induced structural transformation in nanowires. *Mater. Sci. Eng., R* **74**, 173-209 (2013).

22 Leach, A. M., McDowell, M. & Gall, K. Deformation of Top-Down and Bottom-Up Silver Nanowires. *Adv. Funct. Mater.* **17**, 43-53 (2007).

23 Schoen, D. T., Xie, C. & Cui, Y. Electrical Switching and Phase Transformation in Silver Selenide Nanowires. *J. Am. Chem. Soc.* **129**, 4116-4117 (2007).

24 Dick, K. A., Thelander, C., Samuelson, L. & Caroff, P. Crystal Phase Engineering in Single InAs Nanowires. *Nano Lett.* **10**, 3494-3499 (2010).

25 Liu, X. Q., Li, X. B., Zhang, L., Cheng, Y. Q., Yan, Z. G., Xu, M., Han, X. D., Zhang, S. B., Zhang, Z. & Ma, E. New Structural Picture of the Ge_{2}Sb_{2}Te_{5} Phase-Change Alloy. *Phys. Rev. Lett.* **106** (2011).

26 Bei, H., Shim, S., Pharr, G. M. & George, E. P. Effects of pre-strain on the compressive stress–strain response of Mo-alloy single-crystal micropillars. *Acta Mater.* **56**, 4762-4770 (2008).

27 Feng, X. L., Matheny, M. H., Zorman, C. A., Mehregany, M. & Roukes, M. L. Low Voltage Nanoelectromechanical Switches Based on Silicon Carbide Nanowires. *Nano Lett.* **10**, 2891-2896 (2010).

28 Moradpour, A., Schneegans, O., Franger, S., Revcolevschi, A., Salot, R., Auban-Senzier, P., Pasquier, C., Svoukis, E., Giapintzakis, J., Dragos, O., Ciomaga, V.-C. & Chrétien, P. Resistive Switching Phenomena in LixCoO2 Thin Films. *Adv. Mater.* **23**, 4141-4145 (2011).

29 Sun, C.-F., Karki, K., Jia, Z., Liao, H., Zhang, Y., Li, T., Qi, Y., Cumings, J., Rubloff, G. W. & Wang, Y. A Beaded-String Silicon Anode. *ACS Nano* **7**, 2717-2724 (2013).

30 Wang, J. W., He, Y., Fan, F., Liu, X. H., Xia, S., Liu, Y., Harris, C. T., Li, H., Huang, J. Y., Mao, S. X. & Zhu, T. Two-Phase Electrochemical Lithiation in Amorphous Silicon. *Nano Lett.* **13**, 709-715 (2013).

31 Wang, J. W., Liu, X. H., Zhao, K., Palmer, A., Patten, E., Burton, D., Mao, S. X., Suo, Z. & Huang, J. Y. Sandwich-Lithiation and Longitudinal Crack in Amorphous Silicon Coated on Carbon Nanofibers. *Acs Nano*, DOI:10.1021/nn3034343 (2012).

32 Hao, S., Cui, L., Jiang, D., Han, X., Ren, Y., Jiang, J., Liu, Y., Liu, Z., Mao, S., Wang, Y., Li, Y., Ren, X., Ding, X., Wang, S., Yu, C., Shi, X., Du, M., Yang, F., Zheng, Y., Zhang, Z., Li, X., Brown, D. E. & Li, J. A Transforming Metal Nanocomposite with Large Elastic Strain, Low Modulus, and High Strength. *Science* **339**, 1191-1194 (2013).

33 Loh, O. Y. & Espinosa, H. D. Nanoelectromechanical contact switches. *Nat. Nanotechnol.* **7**, 283-295 (2012).

34 Liu, X. H., Zheng, H., Zhong, L., Huang, S., Karki, K., Zhang, L. Q., Liu, Y., Kushima, A., Liang, W. T., Wang, J. W., Cho, J.-H., Epstein, E., Dayeh, S. A., Picraux, S. T., Zhu, T., Li, J., Sullivan, J. P., Cumings, J., Wang, C., Mao, S. X., Ye, Z. Z., Zhang, S. & Huang, J. Y. Anisotropic Swelling and Fracture of Silicon Nanowires during Lithiation. *Nano Letters* **11**, 3312-3318 (2011).

35 Ho, P. S. & Kwok, T. Electromigration in metals. *Reports on Progress in Physics* **52**, 301 (1989).

36 Pierce, D. & Brusius, P. Electromigration: A review. *Microelectronics Reliability* **37**, 1053-1072 (1997).

37 Uchic, M. D., Dimiduk, D. M., Florando, J. N. & Nix, W. D. Sample Dimensions Influence Strength and Crystal Plasticity. *Science* **305**, 986-989 (2004).

38 Zhu, Y. An electromechanical material testing system for in situ electron microscopy and applications. *Proc. Natl. Acad. Sci. U.S.A.* **102**, 14503-14508 (2005).

39 Li, J., Van Vliet, K. J., Zhu, T., Yip, S. & Suresh, S. Atomistic mechanisms governing elastic limit and incipient plasticity in crystals. *Nature* **418**, 307-310 (2002).

40 Weinberger, C. R. & Cai, W. Surface-controlled dislocation multiplication in metal micropillars. *Proc. Natl. Acad. Sci. U.S.A.* **105**, 14304-14307 (2008).

41 Li, X., Wei, Y., Lu, L., Lu, K. & Gao, H. Dislocation nucleation governed softening and maximum strength in nano-twinned metals. *Nature* **464**, 877-880 (2010).

42 Greer, J., Oliver, W. & Nix, W. Size dependence of mechanical properties of gold at the micron scale in the absence of strain gradients. *Acta Mater.* **53**, 1821-1830 (2005).

43 Zhu, T., Li, J., Samanta, A., Leach, A. & Gall, K. Temperature and Strain-Rate Dependence of Surface Dislocation Nucleation. *Phys. Rev. Lett.* **100**, 025502 (2008).

44 Shan, Z. W., Mishra, R. K., Syed Asif, S. A., Warren, O. L. & Minor, A. M. Mechanical annealing and source-limited deformation in submicrometre-diameter Ni crystals. *Nat. Mater.* **7**, 115-119 (2007).

45 Oh, S. H., Legros, M., Kiener, D. & Dehm, G. In situ observation of dislocation nucleation and escape in a submicrometre aluminium single crystal. *Nat. Mater.* **8**, 95-100 (2009).

46 Diao, J., Gall, K. & Dunn, M. L. Surface-stress-induced phase transformation in metal nanowires. *Nat. Mater.* **2**, 656-660 (2003).

47 Park, H. & Zimmerman, J. Modeling inelasticity and failure in gold nanowires. *Phys. Rev. B* **72** (2005).

48 Cao, A., Wei, Y. & Mao, S. X. Alternating starvation of dislocations during plastic yielding in metallic nanowires. *Scr. Mater.* **59**, 219-222 (2008).

49 Wang, Y., Teitel, S. & Dellago, C. Surface-Driven Bulk Reorganization of Gold Nanorods. *Nano Lett.* **5**, 2174-2178 (2005).

50 Park, H., Gall, K. & Zimmerman, J. Deformation of FCC nanowires by twinning and slip. *J. Mech. Phys. Solids* **54**, 1862-1881 (2006).

51 Liang, W., Zhou, M. & Ke, F. Shape Memory Effect in Cu Nanowires. *Nano Lett.* **5**, 2039-2043 (2005).

52 Liang, W. & Zhou, M. Atomistic simulations reveal shape memory of fcc metal nanowires. *Phys. Rev. B* **73** (2006).

53 Zheng, H., Cao, A. J., Weinberger, C. R., Huang, J. Y., Du, K., Wang, J. B., Ma, Y. Y., Xia, Y. N. & Mao, S. X. Discrete plasticity in sub-10-nm-sized gold crystals. *Nat. Commun.* **1**, 144 (2010).

54 Zhu, Y., Wang, J. W., Liu, Y., Liu, X., Kushima, A., Liu, Y., Xu, Y., Mao, S. X., Li, J., Wang, C. & Huang, J. Y. In Situ Atomic-Scale Imaging of Phase Boundary Migration in

FePO4 Microparticles During Electrochemical Lithiation. *Adv. Mater.* **25**, 5461-5466 (2013).

55 Huang, J. Y., Qi, L. & Li, J. In situ imaging of layer-by-layer sublimation of suspended graphene. *Nano Res.* **3**, 43-50 (2010).

56 Lu, Y., Song, J., Huang, J. Y. & Lou, J. Fracture of Sub-20nm Ultrathin Gold Nanowires. *Adv. Funct. Mater.* **21**, 3982-3989 (2011).

57 Huang, J. Y., Zheng, H., Mao, S. X., Li, Q. & Wang, G. T. In Situ Nanomechanics of GaN Nanowires. *Nano Lett.* **11**, 1618-1622 (2011).

58 Greer, J. R. Nanotwinned metals: It's all about imperfections. *Nat. Mater.* **12**, 689-690 (2013).

59 Hirth, J. P. & Lothe, J. *Theory of Dislocations*. (Wiley, 1982).

60 Meyers, M. A. & Chawla, K. K. *Mechanical Behavior of Materials*. 2nd edn, (Cambridge University Press, 2009).

61 Yamakov, V., Wolf, D., Phillpot, S. R., Mukherjee, A. K. & Gleiter, H. Dislocation processes in the deformation of nanocrystalline aluminium by molecular-dynamics simulation. *Nat. Mater.* **1**, 45-49 (2002).

62 Gleiter, H. *Nanocrystalline materials*. (Springer, 1991).

63 Meyers, M. A., Mishra, A. & Benson, D. J. Mechanical properties of nanocrystalline materials. *Prog. Mater. Sci.* **51**, 427-556 (2006).

64 Shan, Z. Grain Boundary-Mediated Plasticity in Nanocrystalline Nickel. *Science* **305**, 654-657 (2004).

65 Lu, L. Superplastic Extensibility of Nanocrystalline Copper at Room Temperature. *Science* **287**, 1463-1466 (2000).

66 Schiøtz, J. & Jacobsen, K. W. A Maximum in the Strength of Nanocrystalline Copper. *Science* **301**, 1357-1359 (2003).

67 Schiøtz, J., Di Tolla, F. D. & Jacobsen, K. W. Softening of nanocrystalline metals at very small grain sizes. *Nature* **391**, 561-563 (1998).

68 Greer, J. & Nix, W. Nanoscale gold pillars strengthened through dislocation starvation. *Phys. Rev. B* **73**, 245410 (2006).

69 Kiener, D. & Minor, A. M. Source Truncation and Exhaustion: Insights from Quantitative in situ TEM Tensile Testing. *Nano Lett.* **11**, 3816-3820 (2011).

70 Chisholm, C., Bei, H., Lowry, M. B., Oh, J., Syed Asif, S. A., Warren, O. L., Shan, Z. W., George, E. P. & Minor, A. M. Dislocation starvation and exhaustion hardening in Mo alloy nanofibers. *Acta Mater.* **60**, 2258-2264 (2012).

71 Greer, J. R., Weinberger, C. R. & Cai, W. Comparing the strength of f.c.c. and b.c.c. sub-micrometer pillars: Compression experiments and dislocation dynamics simulations. *Mater. Sci. Eng., A* **493**, 21-25 (2008).

72 Brinckmann, S., Kim, J.-Y. & Greer, J. Fundamental Differences in Mechanical Behavior between Two Types of Crystals at the Nanoscale. *Phys. Rev. Lett.* **100** (2008).

73 Kim, J.-Y. & Greer, J. R. Tensile and compressive behavior of gold and molybdenum single crystals at the nano-scale. *Acta Mater.* **57**, 5245-5253 (2009).

74 Dmitriev, S. V., Kitamura, T., Li, J., Umeno, Y., Yashiro, K. & Yoshikawa, N. Near-surface lattice instability in 2D fiber and half-space. *Acta Mater.* **53**, 1215-1224 (2005).

75 Sansoz, F. Surface Faceting Dependence of Thermal Transport in Silicon Nanowires. *Nano Lett.* **11**, 5378-5382 (2011).

76 Deng, C. & Sansoz, F. Near-Ideal Strength in Gold Nanowires Achieved through Microstructural Design. *ACS Nano* **3**, 3001-3008 (2009).

77 Fujita, T., Guan, P., McKenna, K., Lang, X., Hirata, A., Zhang, L., Tokunaga, T., Arai, S., Yamamoto, Y., Tanaka, N., Ishikawa, Y., Asao, N., Yamamoto, Y., Erlebacher, J. & Chen, M. Atomic origins of the high catalytic activity of nanoporous gold. *Nat. Mater.* **11**, 775-780 (2012).

78 Weinberger, C. R., Jennings, A. T., Kang, K. & Greer, J. R. Atomistic simulations and continuum modeling of dislocation nucleation and strength in gold nanowires. *J. Mech. Phys. Solids* **60**, 84-103 (2012).

79 Algra, R. E., Verheijen, M. A., Borgström, M. T., Feiner, L.-F., Immink, G., van Enckevort, W. J., Vlieg, E. & Bakkers, E. P. Twinning superlattices in indium phosphide nanowires. *Nature* **456**, 369-372 (2008).

80 Clatterbuck, D. M., Krenn, C. R., Cohen, M. L. & Morris, J. W., Jr. Phonon Instabilities and the Ideal Strength of Aluminum. *Physical Review Letters* **91**, 135501 (2003).

81 Bernardi, M., Raja, S. N. & Lim, S. K. Nanotwinned gold nanowires obtained by chemical synthesis. *Nanotechnology* **21**, 285607 (2010).

82 Hong, X., Wang, D. & Li, Y. Kinked gold nanowires and their SPR/SERS properties. *Chem. Commun.* **47**, 9909-9911 (2011).

83 Zhong, S., Koch, T., Wang, M., Scherer, T., Walheim, S., Hahn, H. & Schimmel, T. Nanoscale Twinned Copper Nanowire Formation by Direct Electrodeposition. *Small* **5**, 2265-2270 (2009).

84 Wood, E. L. & Sansoz, F. Growth and properties of coherent twinning superlattice nanowires. *Nanoscale* **4**, 5268-5276 (2012).

85 Christian, J. Some surprising features of the plastic deformation of body-centered cubic metals and alloys. *Metall. Mater. Trans. A* **14**, 1237-1256 (1983).

86 Lu, K., Lu, L. & Suresh, S. Strengthening Materials by Engineering Coherent Internal Boundaries at the Nanoscale. *Science* **324**, 349-352 (2009).

87 Lu, L., Shen, Y. F., Chen, X. H., Qian, L. H. & Lu, K. Ultrahigh strength and high electrical conductivity in copper. *Science* **304**, 422-426 (2004).

88 Lu, L., Chen, X., Huang, X. & Lu, K. Revealing the Maximum Strength in Nanotwinned Copper. *Science* **323**, 607-610 (2009).

89 Zhang, Z. J., Zhang, P., Li, L. L. & Zhang, Z. F. Fatigue cracking at twin boundaries: Effects of crystallographic orientation and stacking fault energy. *Acta Mater.* **60**, 3113-3127 (2012).

90 Qu, S., Zhang, P., Wu, S. D., Zang, Q. S. & Zhang, Z. F. Twin boundaries: Strong or weak? *Scr. Mater.* **59**, 1131-1134 (2008).

91 Bufford, D., Wang, H. & Zhang, X. High strength, epitaxial nanotwinned Ag films. *Acta Mater.* **59**, 93-101 (2011).

92 Zhu, T. & Gao, H. Plastic deformation mechanism in nanotwinned metals: An insight from molecular dynamics and mechanistic modeling. *Scr. Mater.* **66**, 843-848 (2012).

93 Ma, E., Wang, Y. M., Lu, Q. H., Sui, M. L., Lu, L. & Lu, K. Strain hardening and large tensile elongation in ultrahigh-strength nano-twinned copper. *Appl. Phys. Lett.* **85**, 4932 (2004).

94 Wang, Y. B. & Sui, M. L. Atomic-scale in situ observation of lattice dislocations passing through twin boundaries. *Appl. Phys. Lett.* **94**, 021909 (2009).

95 Zhang, X., Misra, A., Wang, H., Nastasi, M., Embury, J. D., Mitchell, T. E., Hoagland, R. G. & Hirth, J. P. Nanoscale-twinning-induced strengthening in austenitic stainless steel thin films. *Appl. Phys. Lett.* **84**, 1096 (2004).

96 Lu, Y., Song, J., Huang, J. & Lou, J. Surface dislocation nucleation mediated deformation and ultrahigh strength in sub-10-nm gold nanowires. *Nano Res.* **4**, 1-7 (2011).

97 Hao, Y., Meng, G., Wang, Z. L., Ye, C. & Zhang, L. Periodically Twinned Nanowires and Polytypic Nanobelts of ZnS: The Role of Mass Diffusion in Vapor−Liquid−Solid Growth. *Nano Lett.* **6**, 1650-1655 (2006).

98 Lopez, F. J., Hemesath, E. R. & Lauhon, L. J. Ordered stacking fault arrays in silicon nanowires. *Nano Lett.* **9**, 2774-2779 (2009).

99 Shin, N., Chi, M., Howe, J. Y. & Filler, M. A. Rational Defect Introduction in Silicon Nanowires. *Nano Lett.* **13**, 1928–1933 (2013).

100 Woo, R. L., Xiao, R., Kobayashi, Y., Gao, L., Goel, N., Hudait, M. K., Mallouk, T. E. & Hicks, R. Effect of twinning on the photoluminescence and photoelectrochemical properties of indium phosphide nanowires grown on silicon (111). *Nano Lett.* **8**, 4664-4669 (2008).

101 Deng, C. & Sansoz, F. Fundamental differences in the plasticity of periodically twinned nanowires in Au, Ag, Al, Cu, Pb and Ni. *Acta Mater.* **57**, 6090-6101 (2009).

102 Deng, C. & Sansoz, F. Enabling Ultrahigh Plastic Flow and Work Hardening in Twinned Gold Nanowires. *Nano Lett.* **9**, 1517-1522 (2009).

103 Deng, C. & Sansoz, F. Size-dependent yield stress in twinned gold nanowires mediated by site-specific surface dislocation emission. *Appl. Phys. Lett.* **95**, 091914 (2009).

104 Deng, C. & Sansoz, F. Repulsive force of twin boundary on curved dislocations and its role on the yielding of twinned nanowires. *Scr. Mater.* **63**, 50-53 (2010).

105 Afanasyev, K. A. & Sansoz, F. Strengthening in Gold Nanopillars with Nanoscale Twins. *Nano Lett.* **7**, 2056-2062 (2007).

106 Chen, Z., Jin, Z. & Gao, H. Repulsive force between screw dislocation and coherent twin boundary in aluminum and copper. *Physical Review B* **75**, 212104 (2007).

107 Seo, J.-H., Yoo, Y., Park, N.-Y., Yoon, S.-W., Lee, H., Han, S., Lee, S.-W., Seong, T.-Y., Lee, S.-C., Lee, K.-B., Cha, P.-R., Park, H. S., Kim, B. & Ahn, J.-P. Superplastic Deformation of Defect-Free Au Nanowires via Coherent Twin Propagation. *Nano Lett.* **11**, 3499-3502 (2011).

108 Wu, B., Heidelberg, A. & Boland, J. J. Mechanical properties of ultrahigh-strength gold nanowires. *Nat. Mater.* **4**, 525-529 (2005).

109 Peng, C., Zhong, Y., Lu, Y., Narayanan, S., Zhu, T. & Lou, J. Strain rate dependent mechanical properties in single crystal nickel nanowires. *Appl. Phys. Lett.* **102**, 083102 (2013).

110 Christian, J. W. & Mahajan, S. Deformation twinning. *Prog. Mater. Sci.* **39**, 1-157 (1995).

111 Lagerlöf, K. P. D. On deformation twinning in b.c.c. metals. *Acta Metall. Mater.* **41**, 2143-2151 (1993).

112 Zhu, Y. T., Liao, X. Z. & Wu, X. L. Deformation twinning in nanocrystalline materials. *Prog. Mater. Sci.* **57**, 1-62 (2012).

113 Meyers, M. A., Vöhringer, O. & Lubarda, V. A. The onset of twinning in metals: a constitutive description. *Acta Mater.* **49**, 4025-4039 (2001).

114 El-Danaf, E., Kalidindi, S. & Doherty, R. Influence of grain size and stacking-fault energy on deformation twinning in fcc metals. *Metall. Mater. Trans. A* **30**, 1223-1233 (1999).

115 Rohatgi, A., Vecchio, K. & Gray, G. The influence of stacking fault energy on the mechanical behavior of Cu and Cu-Al alloys: Deformation twinning, work hardening, and dynamic recovery. *Metall. Mater. Trans. A* **32**, 135-145 (2001).

116 Qu, S., An, X. H., Yang, H. J., Huang, C. X., Yang, G., Zang, Q. S., Wang, Z. G., Wu, S. D. & Zhang, Z. F. Microstructural evolution and mechanical properties of Cu–Al alloys subjected to equal channel angular pressing. *Acta Mater.* **57**, 1586-1601 (2009).

117 Zhao, Y. H., Zhu, Y. T., Liao, X. Z., Horita, Z. & Langdon, T. G. Tailoring stacking fault energy for high ductility and high strength in ultrafine grained Cu and its alloy. *Appl. Phys. Lett.* **89**, 121906 (2006).

118 Argon, A. S. & Maloof, S. R. Plastic deformation of tungsten single crystals at low temperatures. *Acta Metall.* **14**, 1449-1462 (1966).

119 Argon, A. S. & Maloof, S. R. Fracture of tungsten single crystals at low temperatures. *Acta Metall.* **14**, 1463-1468 (1966).

120 Murr, L. E., Meyers, M. A., Niou, C. S., Chen, Y. J., Pappu, S. & Kennedy, C. Shock-induced deformation twinning in tantalum. *Acta Mater.* **45**, 157-175 (1997).

121 Hsiung, L. M. & Lassila, D. H. Shock-induced deformation twinning and omega transformation in tantalum and tantalum–tungsten alloys. *Acta Mater.* **48**, 4851-4865 (2000).

122 Rösner, H., Markmann, J. & Weissmüller, J. Deformation twinning in nanocrystalline Pd. *Philos. Mag. Lett.* **84**, 321-334 (2004).

123 Wu, X.-L. & Ma, E. Deformation twinning mechanisms in nanocrystalline Ni. *Appl. Phys. Lett.* **88**, 061905 (2006).

124 Liao, X. Z., Zhao, Y. H., Srinivasan, S. G., Zhu, Y. T., Valiev, R. Z. & Gunderov, D. V. Deformation twinning in nanocrystalline copper at room temperature and low strain rate. *Appl. Phys. Lett.* **84**, 592 (2004).

125 Huang, C. X., Wang, K., Wu, S. D., Zhang, Z. F., Li, G. Y. & Li, S. X. Deformation twinning in polycrystalline copper at room temperature and low strain rate. *Acta Mater.* **54**, 655-665 (2006).

126 Liao, X. Z., Zhou, F., Lavernia, E. J., He, D. W. & Zhu, Y. T. Deformation twins in nanocrystalline Al. *Appl. Phys. Lett.* **83**, 5062 (2003).

127 Chen, M., Ma, E., Hemker, K. J., Sheng, H., Wang, Y. & Cheng, X. Deformation twinning in nanocrystalline aluminum. *Science* **300**, 1275-1277 (2003).

128 Han, W., Wu, S., Huang, C., Li, S. & Zhang, Z. Orientation Design for Enhancing Deformation Twinning in Cu Single Crystal Subjected to Equal Channel Angular Pressing. *Adv. Eng. Mater.* **10**, 1110-1113 (2008).

129 Rodrigues, V., Sato, F., Galvão, D. & Ugarte, D. Size Limit of Defect Formation in Pyramidal Pt Nanocontacts. *Phys. Rev. Lett.* **99** (2007).

130 Yue, Y., Liu, P., Deng, Q., Ma, E., Zhang, Z. & Han, X. Quantitative Evidence of Crossover toward Partial Dislocation Mediated Plasticity in Copper Single Crystalline Nanowires. *Nano Lett.* **12**, 4045-4049 (2012).

131 Park, H. & Ji, C. On the thermomechanical deformation of silver shape memory nanowires. *Acta Mater.* **54**, 2645-2654 (2006).

132 Duesbery, M. S. & Vitek, V. Plastic anisotropy in b.c.c. transition metals. *Acta Mater.* **46**, 1481-1492 (1998).

133 Vitek, V. Structure of dislocation cores in metallic materials and its impact on their plastic behaviour. *Prog. Mater. Sci.* **36**, 1-27 (1992).

134 Huang, L., Li, Q.-J., Shan, Z.-W., Li, J., Sun, J. & Ma, E. A new regime for mechanical annealing and strong sample-size strengthening in body centred cubic molybdenum. *Nat. Commun.* **2**, 547 (2011).

135 Caillard, D. Kinetics of dislocations in pure Fe. Part I. In situ straining experiments at room temperature. *Acta Mater.* **58**, 3493-3503 (2010).

136 Marian, J., Cai, W. & Bulatov, V. V. Dynamic transitions from smooth to rough to twinning in dislocation motion. *Nat. Mater.* **3**, 158-163 (2004).

137 Ogata, S., Li, J. & Yip, S. Energy landscape of deformation twinning in bcc and fcc metals. *Phys. Rev. B* **71**, 224102 (2005).

138 Siegel, D. J. Generalized stacking fault energies, ductilities, and twinnabilities of Ni and selected Ni alloys. *Appl. Phys. Lett.* **87**, 121901-121903 (2005).

139 Li, S., Ding, X., Deng, J., Lookman, T., Li, J., Ren, X., Sun, J. & Saxena, A. Superelasticity in bcc nanowires by a reversible twinning mechanism. *Phys. Rev. B* **82**, 205435 (2010).

140 Frederiksen, S. L., Jacobsen, K. W. & Schiøtz, J. Simulations of intergranular fracture in nanocrystalline molybdenum. *Acta Mater.* **52**, 5019-5029 (2004).

141 Zhang, Y., Millett, P. C., Tonks, M. & Biner, B. Deformation-twin-induced grain boundary failure. *Scr. Mater.* **66**, 117-120 (2012).

142 Zhang, Y., Millett, P. C., Tonks, M. & Biner, S. B. Deformation twins in nanocrystalline body-centered cubic Mo as predicted by molecular dynamics simulations. *Acta Mater.* **60**, 6421-6428 (2012).

143 Pan, Z., Li, Y. & Wei, Q. Tensile properties of nanocrystalline tantalum from molecular dynamics simulations. *Acta Mater.* **56**, 3470-3480 (2008).

144 Wang, Y. M., Hodge, A. M., Biener, J., Hamza, A. V., Barnes, D. E., Liu, K. & Nieh, T. G. Deformation twinning during nanoindentation of nanocrystalline Ta. *Appl. Phys. Lett.* **86**, 101915-101913 (2005).

145 Li, S., Ding, X., Li, J., Ren, X., Sun, J. & Ma, E. High-Efficiency Mechanical Energy Storage and Retrieval Using Interfaces in Nanowires. *Nano Lett.* **10**, 1774-1779 (2010).

146 Cao, A. Shape memory effects and pseudoelasticity in bcc metallic nanowires. *J. Appl. Phys.* **108**, 113531 (2010).

147 Wang, P., Chou, W., Nie, A., Huang, Y., Yao, H. & Wang, H. Molecular dynamics simulation on deformation mechanisms in body-centered-cubic molybdenum nanowires. *J. Appl. Phys.* **110**, 093521-093528 (2011).

148 Yu, Q., Qi, L., Mishra, R. K., Li, J. & Minor, A. M. Reducing deformation anisotropy to achieve ultrahigh strength and ductility in Mg at the nanoscale. *Proc. Natl. Acad. Sci. U.S.A.* **110**, 13289-13293 (2013).

149 Yu, Q., Qi, L., Chen, K., Mishra, R. K., Li, J. & Minor, A. M. The Nanostructured Origin of Deformation Twinning. *Nano Lett.* **12**, 887-892 (2012).

150 Yu, Q., Shan, Z.-W., Li, J., Huang, X., Xiao, L., Sun, J. & Ma, E. Strong crystal size effect on deformation twinning. *Nature* **463**, 335-338 (2010).

151 Lu, Y., Huang, J. Y., Wang, C., Sun, S. & Lou, J. Cold welding of ultrathin gold nanowires. *Nat. Nanotechnol.* **5**, 218-224 (2010).

152 Wang, L., Zhang, Z. & Han, X. In situ experimental mechanics of nanomaterials at the atomic scale. *NPG Asia Materials* **5**, e40 (2013).

153 Yang, L. & et al. Quantitative in situ TEM tensile testing of an individual nickel nanowire. *Nanotechnology* **22**, 355702 (2011).

154 Plimpton, S. Fast Parallel Algorithms for Short-Range Molecular Dynamics. *J. Comput. Phys.* **117**, 1-19 (1995).

155 Grochola, G., Russo, S. P. & Snook, I. K. On fitting a gold embedded atom method potential using the force matching method. *J. Chem. Phys.* **123**, 204719 (2005).

156 Li, J. AtomEye: an efficient atomistic configuration viewer. *Modell. Simul. Mater. Sci. Eng.* **11**, 173-177 (2003).

157 Mishin, Y., Mehl, M. J., Papaconstantopoulos, D. A., Voter, A. F. & Kress, J. D. Structural stability and lattice defects in copper: Ab initio, tight-binding, and embedded-atom calculations. *Phys. Rev. B* **63**, 224106 (2001).

158 Stukowski, A. Visualization and analysis of atomistic simulation data with OVITO–the Open Visualization Tool. *Modelling and Simulation in Materials Science and Engineering* **18**, 015012 (2010).

159 Ogata, S., Li, J., Hirosaki, N., Shibutani, Y. & Yip, S. Ideal shear strain of metals and ceramics. *Phys. Rev. B* **70**, 104104 (2004).

160 Kiritani, M. Story of stacking fault tetrahedra. *Mater. Chem. Phys.* **50**, 133-138 (1997).

161 Silcox, J. & Hirsch, P. B. Direct observations of defects in quenched gold. *Philos. Mag.* **4**, 72-89 (1959).

162 Clarebrough, L. M. Stacking-fault tetrahedra in annealed f.c.c. metals and alloys. *Philos. Mag.* **30**, 1295-1312 (1974).

163 Coene, W., Bender, H. & Amelinckx, S. High resolution structure imaging and image simulation of stacking fault tetrahedra in ion-implanted silicon. *Philos. Mag. A* **52**, 369-381 (1985).

164 Loretto, M. H., Clarebrough, L. M. & Segall, R. L. Stacking-fault tetrahedra in deformed face-centred cubic metals. *Philos. Mag.* **11**, 459-465 (1965).

165 Loretto, M. H. & Pavey, A. The formation of intrinsic stacking-fault tetrahedra in deformed F.C.C. alloys. *Philos. Mag.* **17**, 553-559 (1968).

166 Kojima, S., Satoh, Y., Taoka, H., Ishida, I., Yoshiie, T. & Kiritani, M. Confirmation of vacancy-type stacking fault tetrahedra in quenched, deformed and irradiated face-centred cubic metals. *Philos. Mag. A* **59**, 519-532 (1989).

167 Kiritani, M., Yasunaga, K., Matsukawa, Y. & Komatsu, M. Plastic Deformation of Metal Thin Films without Involving Dislocations and Anomalous Production of Point Defects. *Radiat. Eff. Defects Solids* **157**, 3-24 (2002).

168 Kiritani, M. Dislocation-free plastic deformation under high stress. *Mater. Sci. Eng., A* **350**, 1-7 (2003).

169 Wirth, B. D., Bulatov, V. & Diaz de la Rubia, T. Atomistic simulation of stacking fault tetrahedra formation in Cu. *J. Nucl. Mater.* **283-287, Part 2**, 773-777 (2000).

170 Matsukawa, Y., Osetsky, Y. N., Stoller, R. E. & Zinkle, S. J. Destruction processes of large stacking fault tetrahedra induced by direct interaction with gliding dislocations. *J. Nucl. Mater.* **351**, 285-294 (2006).

171 Martinez, E., Marian, J., Arsenlis, A., Victoria, M. & Perlado, J. M. A dislocation dynamics study of the strength of stacking fault tetrahedra. Part I: interactions with screw dislocations. *Philos. Mag.* **88**, 809-840 (2008).

172 Lee, H. J. & Wirth, B. D. Molecular dynamics simulation of the interaction between a mixed dislocation and a stacking fault tetrahedron. *Philos. Mag.* **89**, 821-841 (2009).

173 Matsukawa, Y., Osetsky, Y. N., Stoller, R. E. & Zinkle, S. J. Mechanisms of stacking fault tetrahedra destruction by gliding dislocations in quenched gold. *Philos. Mag.* **88**, 581-597 (2008).

174 Niewczas, M. & Hoagland, R. G. Molecular dynamics studies of the interaction of a/6 ⟨112⟩ Shockley dislocations with stacking fault tetrahedra in copper. Part I: Intersection of SFT by an isolated Shockley. *Philos. Mag.* **89**, 623-640 (2009).

175 Szelestey, P., Patriarca, M. & Kaski, K. Computational study of a screw dislocation interacting with a stacking-fault tetrahedron. *Modell. Simul. Mater. Sci. Eng.* **13**, 541-551 (2005).

176 Robach, J. S., Robertson, I. M., Lee, H. J. & Wirth, B. D. Dynamic observations and atomistic simulations of dislocation–defect interactions in rapidly quenched copper and gold. *Acta Mater.* **54**, 1679-1690 (2006).

177 Matsukawa, Y., Osetsky, Y. N., Stoller, R. E. & Zinkle, S. J. The collapse of stacking-fault tetrahedra by interaction with gliding dislocations. *Mater. Sci. Eng., A* **400-401**, 366-369 (2005).

178 Osetsky, Y. N., Rodney, D. & Bacon, D. J. Atomic-scale study of dislocation–stacking fault tetrahedron interactions. Part I: mechanisms. *Philos. Mag.* **86**, 2295-2313 (2006).

179 Uberuaga, B. P., Hoagland, R. G., Voter, A. F. & Valone, S. M. Direct Transformation of Vacancy Voids to Stacking Fault Tetrahedra. *Phys. Rev. Lett.* **99**, 135501 (2007).

180 Wang, H., Xu, D. S., Yang, R. & Veyssière, P. The formation of stacking fault tetrahedra in Al and Cu: I. Dipole annihilation and the nucleation stage. *Acta Mater.* **59**, 1-9 (2011).

181 Wang, H., Xu, D. S., Yang, R. & Veyssière, P. The formation of stacking fault tetrahedra in Al and Cu: III. Growth by expanding ledges. *Acta Mater.* **59**, 19-29 (2011).

182 Nix, W. D. & Lee, S.-W. Micro-pillar plasticity controlled by dislocation nucleation at surfaces. *Philos. Mag.* **91**, 1084-1096 (2011).

183 Chrobak, D., Tymiak, N., Beaber, A., Ugurlu, O., Gerberich, W. W. & Nowak, R. Deconfinement leads to changes in the nanoscale plasticity of silicon. *Nat. Nanotechnol.* **6**, 480-484 (2011).

184 Wang, J. W., Narayanan, S., Yu Huang, J., Zhang, Z., Zhu, T. & Mao, S. X. Atomic-scale dynamic process of deformation-induced stacking fault tetrahedra in gold nanocrystals. *Nat. Commun.* **4**, 2340 (2013).

185 Matsukawa, Y. & Zinkle, S. J. One-Dimensional Fast Migration of Vacancy Clusters in Metals. *Science* **318**, 959-962 (2007).

186 Arakawa, K., Ono, K., Isshiki, M., Mimura, K., Uchikoshi, M. & Mori, H. Observation of the One-Dimensional Diffusion of Nanometer-Sized Dislocation Loops. *Science* **318**, 956-959 (2007).

187 Wirth, B. D. How Does Radiation Damage Materials? *Science* **318**, 923-924 (2007).

188 Kuhlmann-Wilsdorf, D. The growth and annealing of stacking fault tetrahedra. *Acta Metall.* **13**, 257-270 (1965).

189 Mordehai, D., Rabkin, E. & Srolovitz, D. J. Pseudoelastic Deformation during Nanoscale Adhesive Contact Formation. *Phys. Rev. Lett.* **107**, 096101 (2011).

190 Egerton, R. F., Li, P. & Malac, M. Radiation damage in the TEM and SEM. *Micron* **35**, 399-409 (2004).

191 Jose-Yacaman, M., Gutierrez-Wing, C., Miki, M., Yang, D.-Q., Piyakis, K. & Sacher, E. Surface diffusion and coalescence of mobile metal nanoparticles. *J. Phys. Chem. B* **109**, 9703-9711 (2005).

192 Lagos, M., Sato, F., Galvão, D. & Ugarte, D. Mechanical Deformation of Nanoscale Metal Rods: When Size and Shape Matter. *Physical Review Letters* **106**, 055501 (2011).

193 Zheng, H., Wang, J., Huang, J. Y., Wang, J. & Mao, S. X. Void-assisted plasticity in Ag nanowires with a single twin structure. *Nanoscale* **6**, 9574-9578 (2014).

194 Lu, Y., Song, J., Huang, J. & Lou, J. Surface dislocation nucleation mediated deformation and ultrahigh strength in sub-10-nm gold nanowires. *Nano Research*, 1-7 (2011).

195 Espinosa, H. D., Prorok, B. C. & Peng, B. Plasticity size effects in free-standing submicron polycrystalline FCC films subjected to pure tension. *J. Mech. Phys. Solids* **52**, 667-689 (2004).

196 Budiman, A. S., Han, S. M., Greer, J. R., Tamura, N., Patel, J. R. & Nix, W. D. A search for evidence of strain gradient hardening in Au submicron pillars under uniaxial compression using synchrotron X-ray microdiffraction. *Acta Materialia* **56**, 602-608 (2008).

197 Sedlmayr, A., Bitzek, E., Gianola, D. S., Richter, G., Mönig, R. & Kraft, O. Existence of two twinning-mediated plastic deformation modes in Au nanowhiskers. *Acta Mater.* **60**, 3985-3993 (2012).

198 Lee, S.-W., Han, S. M. & Nix, W. D. Uniaxial compression of fcc Au nanopillars on an MgO substrate: The effects of prestraining and annealing. *Acta Mater.* **57**, 4404-4415 (2009).

199 Volkert, C. A. & Lilleodden, E. T. Size effects in the deformation of sub-micron Au columns. *Philos. Mag.* **86**, 5567-5579 (2006).

200 Gutkin, M. Y. & Ovid'ko, I. A. Homogeneous nucleation of dislocation loops in nanocrystalline metals and ceramics. *Acta Mater.* **56**, 1642-1649 (2008).

201 Norman, G. E. & Yanilkin, A. V. Homogeneous nucleation of dislocations. *Phys. Solid State* **53**, 1614-1619 (2011).

202 Gutkin, M. Y., Ishizaki, T., Kuramoto, S. & Ovid'ko, I. A. Nanodisturbances in deformed Gum Metal. *Acta Mater.* **54**, 2489-2499 (2006).

203 Gilman, J. J. Influence of dislocation dipoles on physical properties. *Discussions of the Faraday Society* **38**, 123-137 (1964).

204 Gouldstone, A., Van Vliet, K. J. & Suresh, S. Nanoindentation: Simulation of defect nucleation in a crystal. *Nature* **411**, 656-656 (2001).

205 Ma, E., Shen, T. D. & Wu, X. L. Nanostructured metals: Less is more. *Nat. Mater.* **5**, 515-516 (2006).

206 Yue, Y., Liu, P., Zhang, Z., Han, X. & Ma, E. Approaching the Theoretical Elastic Strain Limit in Copper Nanowires. *Nano Lett.* **11**, 3151-3155 (2011).

207 Budiman, A., Han, S., Greer, J., Tamura, N., Patel, J. & Nix, W. A search for evidence of strain gradient hardening in Au submicron pillars under uniaxial compression using synchrotron x-ray microdiffraction. *Acta Mater.* **56**, 602-608 (2008).

208 Jang, D., Li, X., Gao, H. & Greer, J. R. Deformation mechanisms in nanotwinned metal nanopillars. *Nature Nanotechnology* **7**, 594–601 (2012).

209 Van Swygenhoven, H., Derlet, P. M. & Froseth, A. G. Stacking fault energies and slip in nanocrystalline metals. *Nature Materials* **3**, 399-403 (2004).

210 Zhang, Y. & Huang, H. Do Twin Boundaries Always Strengthen Metal Nanowires? *Nanoscale Res. Lett.* **4**, 34-38 (2008).

211 Yu, Q., Shan, Z. W., Li, J., Huang, X. X., Xiao, L., Sun, J. & Ma, E. Strong crystal size effect on deformation twinning. *Nature* **463**, 335-338 (2010).

212 Greer, J. R. & De Hosson, J. T. M. Plasticity in small-sized metallic systems: Intrinsic versus extrinsic size effect. *Prog. Mater. Sci.* **56**, 654-724 (2011).

213 Weinberger, C. R. & Cai, W. Plasticity of metal nanowires. *Journal of Materials Chemistry* **22**, 3277-3292 (2012).

214 Swygenhoven, H. V., Derlet, P. M. & Frøseth, A. G. Stacking fault energies and slip in nanocrystalline metals. *Nat. Mater.* **3**, 399-403 (2004).

215 Warner, D. H., Curtin, W. A. & Qu, S. Rate dependence of crack-tip processes predicts twinning trends in f.c.c. metals. *Nat. Mater.* **6**, 876-881 (2007).

216 San Juan, J., No, M. L. & Schuh, C. A. Nanoscale shape-memory alloys for ultrahigh mechanical damping. *Nature Nanotechnology* **4**, 415-419 (2009).

217 Lai, A., Du, Z. H., Gan, C. L. & Schuh, C. A. Shape Memory and Superelastic Ceramics at Small Scales. *Science* **341**, 1505-1508 (2013).

218 Marichal, C., Van Swygenhoven, H., Van Petegem, S. & Borca, C. {110} Slip with {112} slip traces in bcc Tungsten. *Sci. Rep.* **3**, 2547 (2013).

219 Yamakov, V. I. & Glaessgen, E. H. Nanoscale fracture: To twin or not to twin. *Nat. Mater.* **6**, 795-796 (2007).

220 Kim, J.-Y., Jang, D. & Greer, J. R. Tensile and compressive behavior of tungsten, molybdenum, tantalum and niobium at the nanoscale. *Acta Mater.* **58**, 2355-2363 (2010).

221 Han, M. S., Feng, G., Jung, J. Y., Jung, H. J., Groves, J. R., Nix, W. D. & Yi, C. Critical-temperature/Peierls-stress dependent size effects in body centered cubic nanopillars. *Appl. Phys. Lett.* **102**, 041910 (2013).

222 Xie, K. Y., Shrestha, S., Cao, Y., Felfer, P. J., Wang, Y., Liao, X., Cairney, J. M. & Ringer, S. P. The effect of pre-existing defects on the strength and deformation behavior of α-Fe nanopillars. *Acta Mater.* **61**, 439-452 (2013).

223 Schneider, A., Kaufmann, D., Clark, B., Frick, C., Gruber, P., Mönig, R., Kraft, O. & Arzt, E. Correlation between Critical Temperature and Strength of Small-Scale bcc Pillars. *Phys. Rev. Lett.* **103** (2009).

224 Kang, K., Bulatov, V. V. & Cai, W. Singular orientations and faceted motion of dislocations in body-centered cubic crystals. *Proc. Natl. Acad. Sci. U.S.A.* **109**, 15174-15178 (2012).

225 Narayanan, S., McDowell, D. L. & Zhu, T. Crystal plasticity model for BCC iron atomistically informed by kinetics of correlated kinkpair nucleation on screw dislocation. *J. Mech. Phys. Solids* **65**, 54-68 (2014).

226 Lagerlof, K. P. D. On deformation twinning in BCC metals. *Acta Metallurgica et Materialia* **41**, 2143-2151 (1993).

227 Weinberger, C. R., Boyce, B. L. & Battaile, C. C. Slip planes in bcc transition metals. *Int. Mater. Rev.* **58**, 296-314 (2013).

228 Kaun, L., Luft, A., Richter, J. & Schulze, D. Slip Line Pattern and Active Slip Systems of Tungsten and Molybdenum Single Crystals Weakly Deformed in Tension at Room Temperature. *Phys. Status Solidi B* **26**, 485-499 (1968).

229 Ito, K. & Vitek, V. Atomistic study of non-Schmid effects in the plastic yielding of bcc metals. *Philos. Mag. A* **81**, 1387-1407 (2001).

230 Wang, J., Fan, F., Liu, Y., Jungjohann, K. L., Lee, S. W., Mao, S. X., Liu, X. & Zhu, T. Structural Evolution and Pulverization of Tin Nanoparticles during Lithiation-Delithiation Cycling. *J. Electrochem. Soc.* **161**, F3019-F3024 (2014).

231 Wang, J. W., Liu, X. H., Mao, S. X. & Huang, J. Y. Microstructural evolution of tin nanoparticles during in situ sodium insertion and extraction. *Nano Lett.* **12**, 5897-5902 (2012).

232 Zhu, Y., Wang, J. W., Liu, Y., Liu, X., Kushima, A., Liu, Y., Xu, Y., Mao, S. X., Li, J. & Wang, C. In Situ Atomic-Scale Imaging of Phase Boundary Migration in FePO4 Microparticles During Electrochemical Lithiation. *Adv. Mater.* **25**, 5461-5466 (2013).

233 Liu, Y., Fan, F., Wang, J., Liu, Y., Chen, H., Jungjohann, K., Xu, Y., Zhu, Y., Bigio, D. & Zhu, T. In Situ TEM Study of Electrochemical Sodiation and Potassiation of Carbon Nanofibers. *Nano Lett.* (2014).

234 Liu, X. H., Wang, J. W., Liu, Y., Zheng, H., Kushima, A., Huang, S., Zhu, T., Mao, S. X., Li, J. & Zhang, S. In situ transmission electron microscopy of electrochemical

lithiation, delithiation and deformation of individual graphene nanoribbons. *Carbon* **50**, 3836-3844 (2012).

235 Liu, Y., Zheng, H., Liu, X. H., Huang, S., Zhu, T., Wang, J., Kushima, A., Hudak, N. S., Huang, X. & Zhang, S. Lithiation-induced embrittlement of multiwalled carbon nanotubes. *ACS Nano* **5**, 7245-7253 (2011).

236 Zhong, L., Wang, J., Sheng, H., Zhang, Z. & Mao, S. X. Formation of monatomic metallic glasses through ultrafast liquid quenching. *Nature* **512**, 177-180 (2014).